

Pressure-Operated Soft Robotic Snake Modeling, Control, and Motion Planning

By

Ming Luo

A dissertation submitted to The Worcester Polytechnic Institute in conformity with
the requirements for the degree of Doctor of Philosophy

in

Robotics Engineering

Worcester, Massachusetts

August, 2017

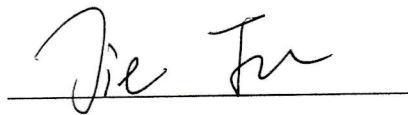
© Ming Luo 2017
All rights reserved

Approved by:



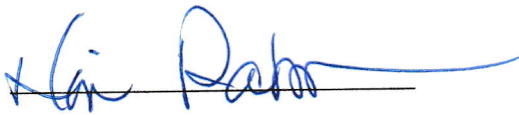
Prof. Cagdas D. Onal, Advisor

Worcester Polytechnic Institute



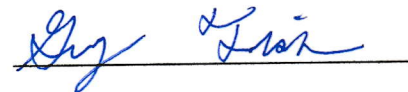
Prof. Jie Fu, Committee Member

Worcester Polytechnic Institute



Prof. Nima Rahbar, Committee Member

Worcester Polytechnic Institute



Prof. Gregory S. Fischer, Graduate Committee Representative

Worcester Polytechnic Institute

Abstract

Search and rescue mobile robots have shown great promise and have been under development by the robotics researchers for many years. They are many locomotion methods for different robotic platforms, including legged, wheeled, flying and hybrid. In general, the environment that these robots would operate in is very hazardous and complicated, where wheeled robots will have difficulty physically traversing and where legged robots would need to spend too much time planning their foot placement. Drawing inspiration from biology, we have noticed that the snake is an animal well-suited to complicated, rubble filled environments. A snake's body has a very simple structure that nevertheless allows the snake to traverse very complex environments smoothly and flexibly using different locomotion modes. Many researchers have developed different kinds of snake robots, but there is still a big discrepancy between the capabilities of current snake robots and natural snakes. Two aspects of this discrepancy are the rigidity of current snake robots, which limit their physical flexibility, and the current techniques

for control and motion planning, which are too complicated to apply to these snake robots without a tremendous amount of computation time and expensive hardware.

In order to bridge the gap in flexibility, pneumatic soft robotics is a potential good solution. A soft body can absorb the impact forces during the collisions with obstacles, making soft snake robots suitable for unpredictable environments. However, the incorporation of autonomous control in soft mobile robotics has not been achieved yet. One reason for this is the lack of the embeddable flexible soft body sensor technology and portable power sources that would allow soft robotic systems to meet the essential hardware prerequisites of autonomous systems. The infinite degree of freedom and fluid-dynamic effects inherent of soft pneumatics make these systems difficult in terms of modeling, control, and motion planning: techniques generally required for autonomous systems.

This dissertation addresses fundamental challenges of soft robotics modeling, control, and motion planning, as well as the challenge of making an effective soft pneumatic snake platform. In my 5 years of PhD work, I have developed four generations of pressure operated WPI soft robotics snakes (SRS), the fastest of which can travel about 220 mm/s, which is around one body per second. In order to make these soft robots autonomous, I first proposed a mathematical dynamical model for the WPI SRS and verified its accuracy through experimentation. Then I designed and fabricated a curvature sensor to be embedded inside each soft actuator to measure their bending angles. The latest WPI SRS is a modularized system which can be scaled up or down depending on the

requirements of the task. I also developed and implemented an algorithm which allows this version of the WPI SRS to correct its own locomotion using iterative learning control. Finally, I developed and tested a motion planning and trajectory following algorithm, which allowed the latest WPI SRS to traverse an obstacle filled environment. Future research will focus on motion planning and control of the WPI SRS in outdoor environments utilizing the camera instead of the tracking system. In addition, it is important to investigate optimal control and motion planning strategies for mobile manipulation tasks where the SRS needs to move and manipulate its environment.. Finally, the future work will include the design, control, and motion planning for a soft snake robot where each segment has two degrees-of-freedom, allowing it to lift itself off the ground and traverse complex-real-world environments.

Acknowledgments

I would first like to express my gratitude to my advisor Prof. Cagdas D. Onal for his mentoring, guidance and support throughout the years of my PhD study. Prof. Onal has been an incredible supervisor and is knowledgeable in all aspects of soft robotics. His academic enthusiasm and technical expertise has enriched my insights to the research of soft robotics and sets solid foundation of that. Prof. Onal has provided me so much intellectual support, academic guidance and professional assistance, which have been invaluable treasure for my doctoral research. I want to acknowledge our collaborators who provide valuable engineering contributions for this dissertation: Prof. Jie Fu, Prof. Nima Rahbar, Dr. Sina Youssefian and Dr. Mahdi Agheli from Worcester Polytechnic Institute.

I would also like to thank my lab mates from Soft Robotics Lab (SRL) for collaborative work and friendship: Fuchen Chen, Weijia Tao, Erik H Skorina, Shadi Tasdighi

Kalat, Siamak Ghorbani-Faal, Selim Ozel, Yinan Sun, Yinan Sun, Yixiao Pan, Junius Santoso, Ugur Celik , Anany Dwivedi, Wut Yee Oo, Yun Qin, Ruibo Yan and Zhengyu Wang. I have very much enjoyed our days and nights working in the lab.

I want to thank mechanical and robotics engineering staff: Barbara Furhman, Randy Robinson, Erica Stults, Deborah Baron, Katherine Crighton for their generous and patient help.

Finally, I am deeply thankful to my family, for their love, understanding, encouragement and support. I could never have come this far without them.

This work would not have been possible without the help and support of my family, advisor, colleagues and friends. I would like to expressly thank everyone who has helped me over the past five years of my PhD life.

Dedication

This dissertation is dedicated to my parents Guoquan Luo and Xiaomin Liang.

Contents

Abstract	i
Acknowledgments	iv
List of Tables	ix
List of Figures	x
Acronyms	xiii
1. Introduction	1
1.1 Background and Motivation	2
1.1.1 Background and Motivation of the Soft Robotics	2
1.1.2 Background and Motivation of the Snake Robotics	3
1.1.3 Motivation and Challenge of the Pneumatically Operated Soft Snake Robot	4
1.2 Literature Review	7
1.2.1 Snake robot	7
1.2.2 Soft robot	9
1.3 Dissertation Contributions	13
1.4 Dissertation Overview	15
2. Design and Fabrication	18
2.1 Soft Bending Actuation Modules	20
2.1.1 First Generation Soft Bending Actuator	20
2.1.2 Second and Third Generation Soft Bending Actuator	21
2.1.3 Fourth Generation Soft Bending Actuator	23
2.2 Proprioceptive Curvature Sensing	27
2.2.1 The First Generation Custom Magnetic Curvature Sensor	28
2.2.2 The Second Generation Custom Magnetic Curvature Sensor	29
2.3 WPI SRS System Architecture	35
2.3.1 The First and Second Generation SRS	35

2.3.2 The Third Generation SRS	36
2.3.3 The Fourth Generation SRS	38
2.4 Discussion and Conclusion	39
3. Modeling and Locomotion Control	40
3.1 SRS DYNAMIC MODEL	41
3.2 SRS Locomotion Control	48
3.3 SRS Actuator Dynamic Model System Identification	49
3.4 Model Experimental Verification	51
3.4.1 The First Generation SRS	52
3.4.2 The Second Generation SRS	63
3.4.3 The Third Generation SRS	66
3.5 Discussion and Conclusion	73
4. Control of Soft Bidirectional Bending Modules	74
4.1 Iterative and Direct SMC (Sliding Mode Control) Algorithm	76
4.2 Experimental Result	81
4.3 Discussion and Conclusion	89
5. Iterative Learning Control and Object avoidance Motion Planning	91
5.1 Iterative Learning Control	93
5.2 Motion planning and Trajectory following	98
5.2.1 Motion Planning	98
5.2.2 Trajectory Following	104
5.2.3 Motion Planning and Trajectory Following Control Simulation	107
5.3 Experimental Verification	108
5.4 Conclusion	115
6. Conclusion	116
6.1 Summary of Work and contributions	117
6.2 Future Work	120
Reference	123

List of Tables

Table 1 Parameters of the SRS dynamic model	43
Table 2 First Generation WPI SRS Experimental Parameters.....	53
Table 3 Algorithm 1	54
Table 4 Algorithm 2	55
Table 5 Experimental Parameters of the Second Generation SRS.....	63
Table 6 Experimental Parameters of the Third Generation SRS.....	67
Table 7 Parameters of the motion planning algorithm	100
Table 8 Parameters Value of the experimental calibration	109
Table 9 Parameters Value of the motion planning algorithm.....	109
Table 10 Performance comparison of the four WPI SRS generations.....	119

List of Figures

Figure 1 Snake Locomotion © 2012 Encyclopedia Britannica, Inc.....	4
Figure 2 First experimental prototype of the soft robotics snake developed by Onal, Rus's group from MIT.....	5
Figure 3 Snake robot systems.....	8
Figure 4 Soft robot systems.....	11
Figure 5 Four generations of WPI SRS.....	15
Figure 6 CAD model (Left) and experimental prototype (right) of the first Generation Soft Bending Actuator.....	21
Figure 7 Fabrication Process of the First Generation Soft Bending Actuator.....	21
Figure 8 CAD model (Left) and experimental prototype (right) of the second and third generation soft bending actuator.....	22
Figure 9 Fabrication process of the second (Left) and third (Right) generation soft bending actuator	23
Figure 10 CAD model (Left) and experimental prototype (right) of the fourth generation soft bending actuator with integrated curvature sensing.....	24
Figure 11 Fabrication process of the fourth generation soft bending actuator.....	26
Figure 12 The structure and fabrication of the first version curvature sensor	29
Figure 13 Finite Element Analysis of the flexible curvature sensor.....	32
Figure 14 The relationship between the cross section shape of the actuator and the sensor performance.	34
Figure 15 The Experimental System of the Tether Robot (The First and Second Generation)	36
Figure 16 The System Architecture of the untethered third generation WPI SRS.....	37
Figure 17 The System Architecture of the modularized fourth generation WPI SRS.....	38
Figure 18 Dynamic force balance between two segments of the SRS.	43
Figure 19 The moment arm of each segment of the SRS varies as a function of bending curvature	45

Figure 20 The dynamic response of the fourth generation soft actuator under 8 psi 50

Figure 21 Position and velocity of the simulated soft snake robot center of mass (CoM) over time for the numerical simulation results..... 52

Figure 22 Experimental information is processed for comparison with simulated results. (a) Curvature information is extracted from the positions and orientations of both ends of each segment. (b) The recovered segment shape when $r_i > 0$ 54

Figure 23 The overlaid curve on the soft snake robot indicates the recovered shape and position of the snake from visual feedback..... 56

Figure 24 The curvature plot of each soft segment in the experiment. The solid line, circle, dashed line, and triangle represent the 1st, 2nd, 3rd, and 4th soft segments, respectively. 56

Figure 25 The curvature plot of each soft segment in the simulation. The solid line, circle, dashed line, and triangle represent the 1st, 2nd, 3rd, and 4th soft segments, respectively. 57

Figure 26 Curvature waveforms of each segment in the experiment (solid line) and the simulation (dashed line). 58

Figure 27 Comparison of the snake robot shapes between the simulation and the experiment at 3, 8, 13, and 16 s. The dashed line shows the simulation and the solid line shows the experimental results..... 59

Figure 28 The root-mean-square (RMS) error of the shape difference between the experiment and the simulation. 60

Figure 29 The root-mean-square (RMS) error of the shape difference between the experiment and the simulation. 60

Figure 30 The root-mean-square (RMS) error of the shape difference between the experiment and the simulation..... 60

Figure 31 Comparison of model predictions and experimental results for different operational parameters of the soft robotic snake in terms of resulting CoM velocities..... 61

Figure 32 Comparison of model predictions and experimental results for different operational parameters of the soft robotic snake in terms of the soft robotic snake in term of resulting CoM velocities and trajectory radii with the offset term $\emptyset = 0$ 63

Figure 33 Comparison of model predictions and experimental results for different operational parameters of the soft robotic snake in terms of the soft robotic snake in term of resulting CoM velocities and trajectory radii with the offset term $\emptyset = 0.4$ 64

Figure 34 A plot of the experimental trajectory (red dots) and fit line (blue line) compared to the complex and simple model trajectories (black and green lines) with frequency 2 Hz and input pressure 54 kPa..... 65

Figure 35 A diagram of each segment. The actuator with an interior pressure chamber is blue area, while the red areas are the gaps. Only blue area is pressurized and capable of active motion..... 66

Figure 36 A series of still images, each 6 s apart, taken to show the snake in operation. The frequency is 1 Hz, and the offset is 0.2..... 68

Figure 37 SRS shape and trajectory when the frequency is 0.9 Hz and the offset is 0.2 (blue), 0.1 (black), 0 (green), -0.1 (pink), and -0.2 (red) in the simulation (a) and experiment (b) in 10s..... 68

Figure 38 The center of mass (CoM) linear velocity and its standard deviation with respect to undulation frequency from 0.75–1 Hz for offset values of 0 (a), 0.1 (b) -0, 1 (c), 0.2 (d), and -0.2 (e)..... 69

Figure 39 The CoM angular velocity and its standard deviation with respect to undulation frequency from 0.75–1Hz for offset values of 0.1 (a) and 0.2 (b).....	69
Figure 40 Performance verification of the four embedded curvature sensors using external motion-capture data as ground truth, for $\omega = 2 \text{ Hz}$ and $\phi = 0$. (a)–(d) represent each segment from head to tail.....	71
Figure 41 Static response of the fourth generation version bending soft robotic module in a range of 150° at $\pm 11 \text{ psi}$	82
Figure 42 Step response of the two controllers.	83
Figure 43 Dynamic response of both controllers following sinusoidal trajectories with frequencies of 0.25 Hz (a), 1 Hz (b), 4 Hz (c), and 6 Hz (d), with the same bending angle amplitude of 34.3°	85
Figure 44 Closed loop frequency response of both controllers tracking sinusoidal signals over a range of frequencies.....	86
Figure 45 (a) Iterative and direct SMC system trajectories for 6 Hz sine wave following.	88
Figure 46 (a) Iterative and direct SMC system trajectories for 2 Hz square wave following..	88
Figure 47 The sensor verification of four generation WPI SRS.....	94
Figure 48 Each module bending angle of the WPI SRS go straight line test control by ILC.	95
Figure 49 Center of Mass (CoM) of the WPI SRS during the ILC at straight line task.....	96
Figure 50 Each module bending angle of the WPI SRS go curve test control by ILC.....	97
Figure 51 Center of Mass (CoM) of the WPI SRS during the ILC at curve task.	97
Figure 52 Bounding box definition.....	99
Figure 53 Motion planning algorithm example	102
Figure 54 Motion planning algorithm simulation	105
Figure 55 The performance of the motion planning algorithm.....	106
Figure 56 Trajectory following of the WPI SRS in simulation	106
Figure 57 Motion planning and trajectory following simulation of WPI SRS.	107
Figure 58 Bounding box from the experiment.....	109
Figure 59 The first scenario experimental results (Target angle is 60°).....	112
Figure 60 The second scenario experimental results (Target angle is 0°).	113
Figure 61 The third scenario experimental results (Target angle is 0°)..	114

Acronyms

SRS soft robotic snake

SMC sliding model control

Chapter 1

1. Introduction

Soft robotics is a technique that involves constructing robots out of flexible materials and using compliant actuation methods. The advantages of soft robotic systems over traditional robots include adaptation to unstructured or unknown environments, organic bio-inspired mobility and manipulation, and increased safety for the robot and for its environment. However, current soft robot platforms suffer from a lack of accurate theoretical dynamic models, proprioceptive measurements, and efficient control and motion planning algorithms, which impede advancements toward full autonomy. This thesis introduces the pressure-operated soft robotic snake platform “WPI SRS” which promises inherent flexibility and versatility to operate in complex and unpredictable environments. In addition, this thesis addresses the fundamental robotics challenges of the soft robot: modeling, sensing, control and motion planning. In doing so, it provides the groundwork for future autonomous soft robots.

1.1 Background and Motivation

1.1.1 Background and Motivation of the Soft Robotics

The robots of today are heavily utilized in factory automation. Conventional robotic structures are made with high stiffness materials. These parts can be manufactured by mechanical machining tools including milling and lathing, and are mechanically assembled. These machines provide powerful solutions in terms of speed, precision and controllability in simple environments at a safe distance from human beings, but are less capable and unsafe for operation in natural environments, like those of humans. In these natural environments, traditional rigid robotic architecture causes significant performance problems that cannot be easily compensated for by the software. Part of this problem is the lack of flexibility in conventional actuation mechanisms [1].

Soft robotics provides an alternative. Given their small minimum stiffness, soft mechanisms are inherently safe and adaptive. A soft body can deform and absorb energy in the event of a crash, and conform to unknown objects and conditions. These inherent advantages mean that soft robots operate similarly closer to biological capabilities observed in nature. A soft robot can adapt and deform to keep contact with uneven ground for operation in unstructured environments. Similarly, it can interact with human and environment more safely than conventional rigid robot system by reducing the risk of injury to itself and surroundings from collision. In addition, soft robots also adapt more readily to various objects, simplifying tasks such as grasping, and can also exhibit improved mobility over soft substrates [2].

1.1.2 Background and Motivation of the Snake Robotics

Robots offer great promise in assisting search-and-rescue operations in extremely hostile and cluttered environments after a variety of accidents. These applications require special robotic capabilities that may not be fulfilled by traditional mobile robots such as operating through narrow openings or complex passages. Though wheeled and walking machines have undergone decades, even centuries, of development, they are still limited in the types of terrain they can traverse. A robotic snake is a salient solution for such conditions since it can navigate on unstructured terrain without limbs while being able to pass through narrow openings or complex passages, similar to its biological counterpart [3,4].

Snakes use four unique modes of terrestrial locomotion, shown on Figure 1: Serpentine, Sidewinding, Concertina, and Rectilinear. Which mode they use depends on the several factors, such as the properties of the surface and the desired speed.

In this research, we focus on the serpentine locomotion, also called lateral undulation, which is the most common locomotion type for snakes. Simple undulation is characterized by waves of lateral bending being propagated along the body from head to tail. The bends push laterally against surface objects, but do not deform locally around them, and usually slip out of contact quickly [5]. This locomotion method makes use of the anisotropic properties of snake skin, which has around ten times the friction in the normal direction than in the tangential direction.

Snake locomotion

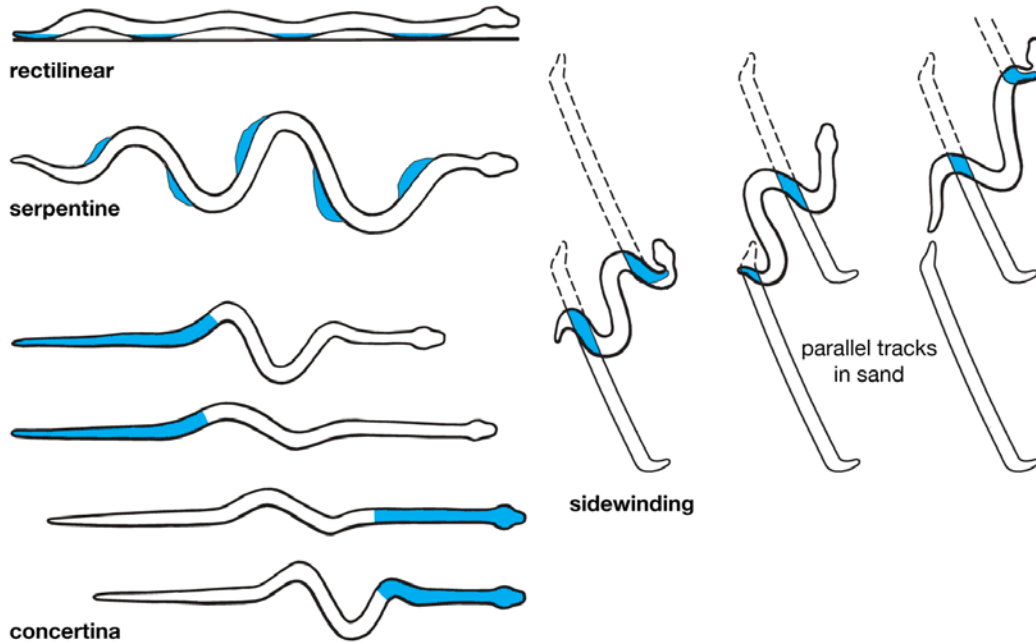


Figure 1 Snake Locomotion © 2012 Encyclopedia Britannica, Inc.

1.1.3 Motivation and Challenge of the Pneumatically Operated Soft Snake Robot

Although many snake robots have been developed, current approaches do not utilize body flexibility [7-31]. Since traditional robot fabrication is based on rigid links, robotic snakes may not be as safe and adaptive as their natural counterparts. To address this issue, D. Rus's group developed and tested a pneumatically-operated soft robotic snake, shown in Figure 2, to explore the full range of possibilities snake-like undulatory locomotion types. The body of this soft robotic snake prototype consists of four bidirectional fluidic elastomer actuators (FEAs) mounted in series, with each actuator-segment pressurized by controlling the state of a solenoid valve array connecting it to a

common pressure source. Passive wheels were mounted between segments generate the necessary frictional anisotropy for forward locomotion [6]. However, there are several unsolved problems in the development of an autonomous soft snake robot capable of operating in a realistic and unknown environment, which represent common challenges for the soft robotics community:

- How to increase the speed of the system;
- Theoretical modeling of the dynamics;
- Proprioceptive feedback sensors;
- Precise dynamic motion planning and control of a continuously deformable body;

The first version of the soft robotic snake can attain an average locomotion speed of 19 mm s^{-1} , which is only one tenth its body length per second. It is still much slower than a real snake. Therefore, this version is impractical for outside applications. In addition, an accurate dynamic model is a fundamental for a mobile robot undergoing serpentine



Figure 2 First experimental prototype of the soft robotics snake developed by Onal, Rus's group from MIT [6]

locomotion as it allows for optimization, control, navigation, and learning algorithms. However, mathematical modeling of soft robots for locomotion optimization and motion

planning and control algorithms has been limited since the deformable nature of these systems creates many challenges, such as the infinite passive degrees-of-freedom and non-linear material behavior. In addition, the development of proprioceptive feedback sensors which can capture the dynamic features of a soft actuator is challenging, since these sensors would need to be both flexible and capable of being miniaturized in order to maintain the advantages of a soft body.

From the soft robotic systems viewpoint, precise motion planning and control of a continuously deformable body with dynamic effect has not been solved like conventional rigid robot dynamics has. This is because soft systems have the infinite control outputs represented by their infinite passive degrees freedom. The problem that this thesis addresses is choosing the optimal control input parameters for the motion planning and control algorithm which can describe the full kinematic and dynamic features of the soft robotics while maintaining the dynamic benefits of the soft robotics.

1.2 Literature Review

1.2.1 Snake robot

Many researchers have studied the principles of snake locomotion and developed robotic equivalents that can replicate snake motion showed on Figure 3. The first snake robot was developed by Shigeo Hirose in 1971 [7-9]. During the subsequent 40 years of research, many snake robots have been developed. Most are modular in design and comprise a number of connected segments which confer flexibility. Although majority are aimed at terrestrial applications, some aquatic devices have been developed. Power sources include electric motors, pneumatics, hydraulics and mechanical methods [10,11].

From the Hirose-Fukushima Robotics Lab, the ACM series robots demonstrate the evolution of the snake robot from the only 2D motion capability robot “ACM III” to the 3D motion, waterproof and other advance robot “ACM-R5” [12-14]. The SINTEF lab developed the “Anna Konda”, a large firefighting snake. This modular jointed robot has a length of 3 m, weighs 75 kg, and has 20 degrees of freedom (DoF), each actuated by a water-powered hydraulic cylinders. It can move using the the sidewinding gait. Two nozzles are attached to the “head” module, which enable the snake to spray water to put out fires [15]. Similarly, the “Aiko” is a portable DC motor-operated system for experimenting with snake robot locomotion [16,17]. The “PIKo” is a snake-like robot for internal inspection of complex pipe structures. It has eight DoF and can go through both horizontal and vertical pipe structures [18].

The researchers from the CMU Biorobotics Lab have developed a modular snake robot which can operate inside steam pipes, vessels and other confined spaces [19-21]. In the Biologically Inspired Robotics Group at Ecole Polytechnique Fédérale Lausanne, the AmphiBot I and II snake robots were developed, which were inspired by snakes and elongated fish such as lampreys to produce a novel type of robot with dexterous locomotion abilities. These were used to investigate hypotheses of how central nervous systems implement these abilities in animals [22-24]. In University of Michigan mobile robotics lab, the propulsion of the OmniTread snake robots achieved by the tank treads on the four sides of every link, which can help the robot walk on the complex terrains [25,26].

The theoretical modeling of the rigid snake robot has been researched over the decades. Sato, Fjerdingen and Shugen studied the modeling of a rigid snake robot in 2D

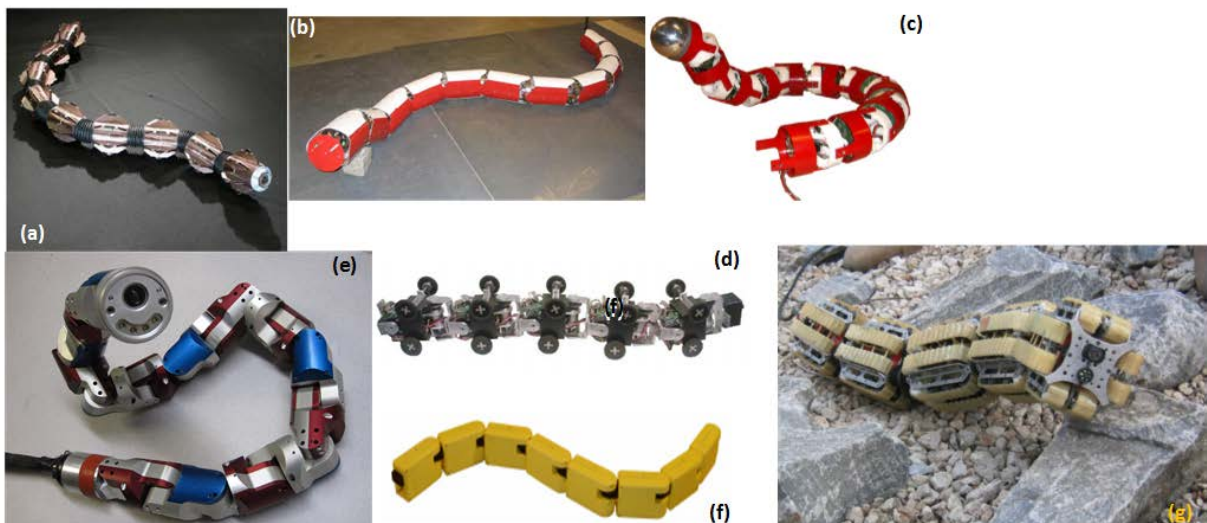


Figure 3 Snake robot systems. (a) ACM-R5 [9-11] (b) Anna Konda [12] (c) Aiko [13-14] (d) PIKo [15] (e) CMU modular snake robot [16-18] (f) AmphiBot II [19-20] (g) OmniTread OT-8 [21,22]

[27-29]. Pettersen added expressions for the linear velocity of individual links based on previous work and divided the general model into an actuated and an un-actuated part. Subsequently, partial feedback linearization of the model was presented [30]. In addition, Patterson proposed a simplified model after linearization and gave proofs of stability and controllability to a rigid snake robot based on the proposed model. Matsuno, Tanaka and Transteth studied segmented rigid snake robot modeling in 3D by taking vertical motions into account [31]. However, the rigid bodies and non-continuous curves of current snake robots limits their physical flexibility and ability to adapt to complex environments.

1.2.2 Soft robot

Generally, there are two actuation methods for soft robots showed on Figure. 4 [32-41]. The first uses mechanical tendons, such as the variable length tendon cable or shape memory alloy (SMA). The other one is through pneumatic or hydraulically actuation. This thesis will focus on pneumatic actuation. The first version of the soft pneumatic actuator is the McKibben actuators, which is compliant linear soft actuators composed of elastomer tubes wrapped in fiber sleeves [42-44]. When pressurized, the McKibben actuator contracts, causing the motive force. In recent years, a new type of actuator has been developed, the Fluidic elastomer actuator (FEA). It is extensible and adaptable, low-power soft actuator. G. M. Whiteside's group developed a multi-gait soft pneumatic quadruped that is capable to traversing difficult obstacles [45-48]. In addition, there is a 3D printed soft jumping robot power by the Combustible fuels [49,50]. The Octobot is the

first robot to be made entirely from soft materials. Powered by a chemical reaction and controlled by a fluidic logic circuit, it heralds a generation of soft robots that might surpass conventional machines [51,52]. In B. Trimmer's group, a soft-bodied robot called GoQBot closely mimics caterpillar rolling [53-55]. In D. Rus's group, an autonomous soft-bodied robotic fish that is hydraulically actuated and capable of sustained swimming in three dimensions [56-58]. A soft robotic manipulation system is capable of autonomous, dynamic, and safe interactions with humans and its environment [59-61]. Walsh's group created a benchtop cardiac simulator and a direct cardiac compression device employing soft actuators in an elastomeric matrix to reduce the risk of the heart failure treatment [62,63]. A soft robotic glove with embedded soft actuators is design for restoring basic hand use for individuals who have peripheral nervous system conditions, including hereditary muscle disorders (e.g. muscular dystrophy), nerve diseases, and Amyotrophic Lateral Sclerosis (ALS, Lou Gehrig's disease) [64-66]. In C. Laschi's group, a soft arm is capable of pushing-based locomotion and object grasping, mimicking the movements that octopuses adopt when crawling [67-70].

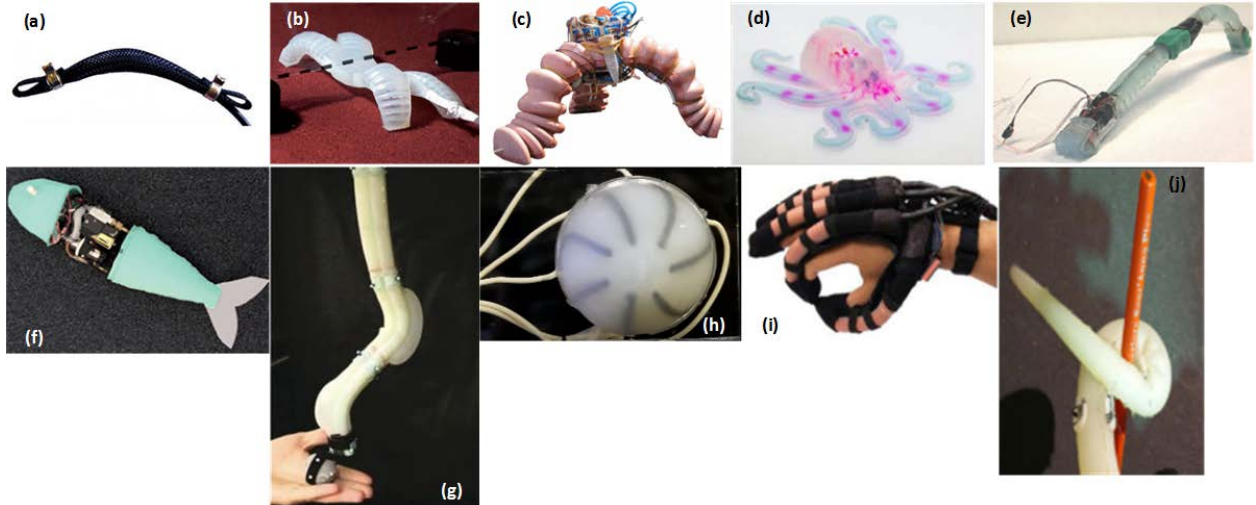


Figure 4 Soft robot systems (a) McKibben muscle [42-44] (b) A multi-gait quadruped [45-48] (c) Jumping powered by internal combustion [49,50] (d) Octobot power by chemical reaction [51,52] (e) Caterpillar-inspired locomotion [53-55] (f) An autonomous fish [56-58] (g) soft robotic manipulation [59-61] (h) soft heart [62,63] (i) soft glove for rehabilitation [64-66] (j) octopus-inspired manipulation [67-70]

However, mathematical modeling and control of soft robots has been limited since the deformable nature of such systems creates many challenges, including having infinite passive degrees of freedom, a particular problem of entirely soft robotics system. Usually, finite element analysis (FEA) is a common tool to model the static model of the soft robot [71-73]. However, FEA is often limited by its computational complexity, and is unsuitable for use in mobile robots. Some researchers have made contribution to the analytical modeling of soft robots [74-78]. Both methods need special mathematical models of the soft material and also utilize different material geometric relationship [79-81]. However, the work done with these methods can only describe and control the static model of the simple actuator system, which could not be implemented in the real time dynamic modeling and control of the complex and multi-segment soft robotic system.

In the soft robotics field, sensor technology which can be used to determine the kinematic and dynamic state of the robotics body is challenging. The many degrees of

freedom of the soft body, the stability of the dynamic response, the portability of the soft robotics body and the scalability are the crucial factors for this technology. There are three different methods achieving this. The first involves utilizing the changing properties of a material as it changes its shape. Examples of this include the commercial resistive flex sensor and the embedded liquid metals stretch sensor, which offer a simple and compact solution for embedded sensing in soft robotics [82-85]. Nevertheless, we concluded in a preliminary study that these methods suffer from dynamic artifacts, such as delayed response and drift [86]. The second method involves using Optical fiber Bragg grating. This method can achieve accurate curvature measurements using a thin and flexible optical fiber. However, the accompanying hardware system that is required to parse the raw data is large, and would occupy the large portion of the soft robotics body, especially for small, tether-less mobile robots with many degrees of freedom [87-88]. The last method involves the combination of a magnet and Hall Effect sensor. The sensor measures the changes in magnetic field as body deformations cause the magnet to change position. This method can capture the high-frequency behavior of the soft actuator perfectly as accurately as the optical method, while being significantly more compact over all. However, the space taken up by the magnet and sensor, both of which need to be inside the body being sensed, limits the miniaturization of this method.

1.3 Dissertation Contributions

This dissertation addresses several research topics related to the development of autonomous mobile soft robotics system, seeking to improve soft robotics technologies in the areas of cost, easy reliable fabrication, and simple control motion planning algorithms. The major contributions of this dissertation are summarized as follows:

The fast controllable mobile soft robot

Our second generation WPI SRS can travel at one body length per second, around 220mm/s, by serpentine locomotion under 10 psi. Its smooth, continuously deforming shape looks like the realistic snake [89].

The first autonomous controllable mobile soft robot with embedded feedback sensor

Our third generation WPI SRS is a self-contained autonomous mobile soft robotics system, with power source, electrical hardware, and pneumatic pump all mounted on board. In addition, each segment has an embedded hall effect curvature sensor which can measure the robot's kinematic state locally, allowing the robot can do feedback control based on this information [91].

The first controllable modularized mobile soft robot with embedded feedback sensor

Our fourth generation WPI SRS is a modularized autonomous mobile soft robotic system. Each module has the independent curvature sensor and control system. This generation WPI SRS is able to self-correct its motion using the local curvature sensor and

iterative learning control algorithm without the external tracking information. In addition, this robot is more robust and flexible than the other soft robotics systems because of its modularity [98].

The accurate analytical dynamic modeling of the soft mobile robotics system

We propose a general solution to the problem of soft robotic system modeling using traditional mechanical prospect. Based on the WPI SRS, this model encapsulates the kinematics and dynamics of the WPI SRS while avoided complex material or dynamic fluid models. Our physical experiments verify the accuracy of the model [93].

The motion planning and trajectory following control algorithm of the soft mobile robotics system

We propose a simple but practical solution for the soft robotic system motion planning and trajectory following. This solution could reduce the infinite DoF of the WPI SRS to a limited number, allowing us to implement established robotic motion planning strategies onto the soft robotic system [98].

1.4 Dissertation Overview

This dissertation discusses the main aspects of four generation WPI SRS, from 2012 to 2017, including the Mechanical design, Fabrication, system architecture, mathematical modeling, motion planning, and control. Images of these four generations of WPI SRS are shown in Figure 5. This introductory chapter introduces the background and motivation for WPI SRS, and discusses related work on soft robots and snake robots.

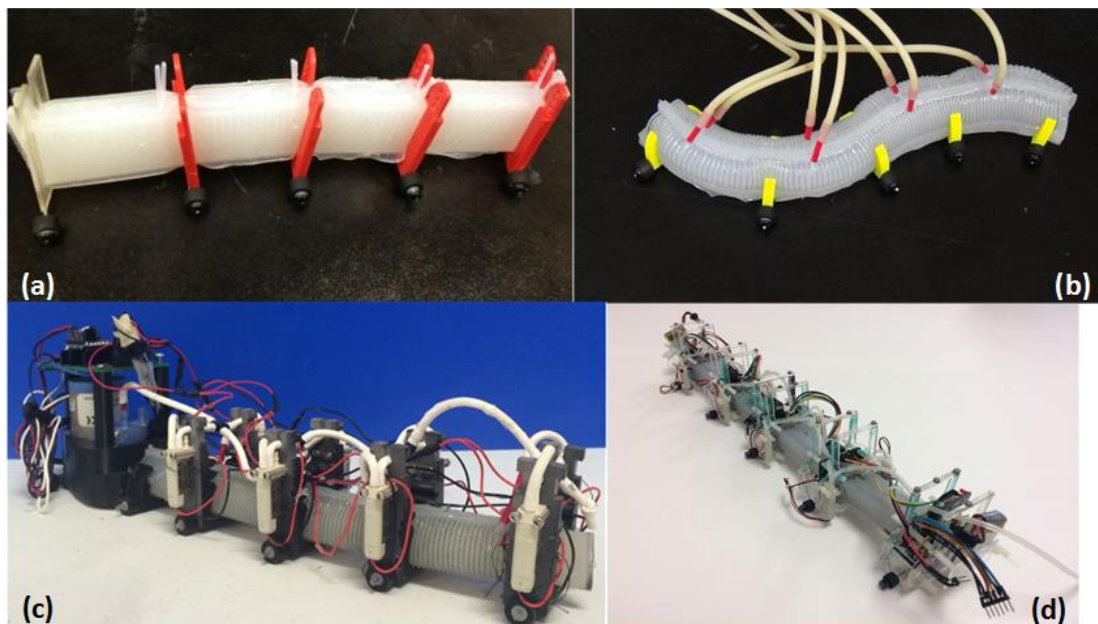


Figure 5 Four generations of WPI SRS. (a) The first (2013) (b) The second (2014) (c) The third (2015) (d) The fourth generation.

Chapter 2 introduces the mechanical design and the fabrication of the four generations WPI SRS. First, in order to increase the WPI SRS's speed and reliability, we optimize the design of the soft modules, making them stronger and has faster. Then we elaborate on the fabrication of the curvature sensors which combine the single-axis Hall

Effect sensor with the magnet. We also optimized the sensor design based on the requirement of WPI SRS to maximize the linearity and working range of the sensor. Last, we describe the system architecture of WPI SRS.

Chapter 3 introduces the dynamic model of WPI SRS. In order to simplify the model under realistic condition, we make several assumptions about the environment and WPI SRS kinematic information. The model seeks to combine tradition rigid snake robot models, the WPI SRS kinematic model, and the soft module dynamic model. The experimental result verify our model's accuracy. In addition, we also describe the basic locomotion method used by the WPI SRS in greater detail, which will be the fundamental control object on Chapter 5.

Chapter 4 introduces the precise feedback control of our single soft bending module under limited system bandwidth. The soft bending module, consisting of a single module from the fourth generation WPI SRS, is the independent system which includes the flexible curvature sensor and the local controller. Therefore, the fourth generation WPI SRS is much more flexible than other generation robots. In this section, we focus on local control of the single soft bending actuator before proceeding to the more challenging system task in the future. We propose two different control configuration of the controller and show the maximum control performance we can achieve under the limited system capability.

Chapter 5 introduces several system tasks for the fourth generation WPI SRS. First, the WPI SRS can correct its motion based on the local curvature sensor and iterative

learning control, compensating for inconsistencies between segments and allowing the soft robot could achieve some tasks locally. We also shows the motion planning algorithm and trajectory following algorithm, allowing the robot to navigate in an obstacle-filled environment. The algorithms shown in this section utilize the minimum observation required to describe the global kinematic and dynamic state of the robot, allowing for far the less computation time in motion planning. We find the minimum control inputs which allow the WPI SRS to keep its dynamic benefits without loss of accuracy.

This dissertation is concluded and future work is discussed in Chapter 6.

Chapter 2

2. Design and Fabrication

The first soft robotic snake made of silicone rubber was developed in 2013 [5]. This snake robot promised significant advantages in achieving traveling curvature waves with a reduced number of pneumatic bending actuation segments as well as safe and adaptive interaction with the environment. However, this soft snake robot is able to move at approximately 20 mm/s under 5 psi pressure input with external fluid tubing, electrical system and power source which is only one tenth its whole body length.

The second generation soft robotic snake utilizing optimized bending actuators, which can locomote using lateral undulation 10 times faster than the original prototype when pressurized air is supplied using external tubing [89].

Towards the ultimate goal of full autonomy, the third generation soft snake robot is a fully self-contained soft robotic snake (WPI SRS) as a mobility platform, which incorporates on-board electrical and fluidic power, embedded control, and distributed solenoid valves for tetherless operation. Custom magnetic curvature sensors are incorporated within each soft bending actuation segment for real-time proprioceptive measurements.

The fourth generation soft snake robot is a modularized soft mobile robotic system with flexible curvature sensors. Compared with the third generation, this robot is able to achieve more complex tasks than the third generation. The soft bending modules from this generation have stronger durability than the previous version actuators because of an updated fabrication.

The outcome of this chapter was published at [90],[92],[93],[98].

2.1 Soft Bending Actuation Modules

2.1.1 First Generation Soft Bending Actuator

The design of the first generation fluidic elastomer actuator is shown in Figure 6, with a CAD drawing and experimental prototype. This actuator is able to reach 90° degree around 4.5 psi and 15 ml of air volume. The experimental prototype is built through molding silicone rubber (Smooth-on Ecoflex 0030) following a fabrication process comprising three steps as shown in Figure 7 and described below:

Step 1: Three premolds of the soft snake body are 3D printed. Two actuation premolds carry the negative of parallel rectangular fluidic channels connected on both ends in a serpentine arrangement. The third one is the constraint premold that has a thin rectangular opening with the same length and width as the channel layer.

Step 2: An inextensible flexible sheet is embedded into the constraint premold in order to add a constraint for the soft body to undergo bending deformation upon pressurization. Then, silicone rubber is poured into both premolds.

Step 3: When cured, all three molds are removed and two actuation molds are glued on both sides of the constraint mold using thin layers of uncured silicone rubber as glue.

The segments are tall and narrow, causing potential balance issues. The fluidic channels embedded in the elastomer for actuation are small and intricate, leading to

possible blockage during fabrication. The actuators are likely to malfunction for pressure inputs higher than 5 psi. This is due to the radial expansion of the actuator, leading to

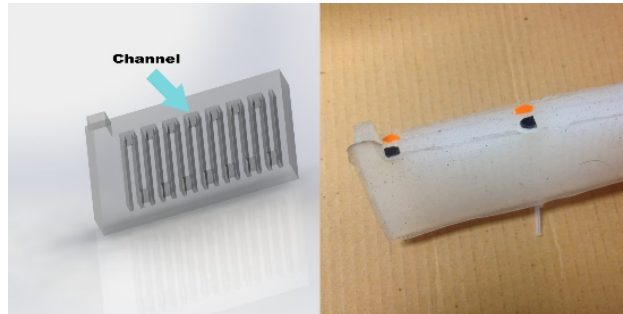


Figure 6 CAD model (Left) and experimental prototype (right) of the first Generation Soft Bending Actuator

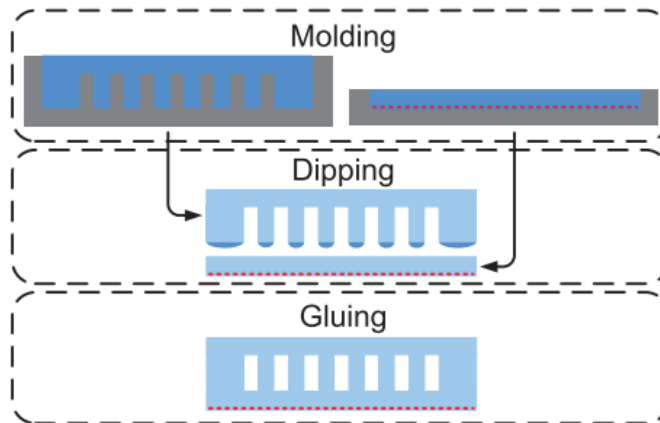


Figure 7 Fabrication Process of the First Generation Soft Bending Actuator

undesired stress and eventual damage with increased pressure. In addition, the segments exhibit slow dynamics with large time constants resulting in a limit on the frequency of the serpentine gait and consequently, locomotion speed.

2.1.2 Second and Third Generation Soft Bending Actuator

Compared with the first generation soft bending actuator [93], the second and third generation soft bending actuator showed on Figure 8 offers robust operation, safety

at larger input pressure values, faster response, lower center of gravity, and a flat bottom for better compatibility with snake-like lateral undulation [90]. This actuator is able to reach 90° degree around 7 psi and 45 ml of air volume. The entire fabrication

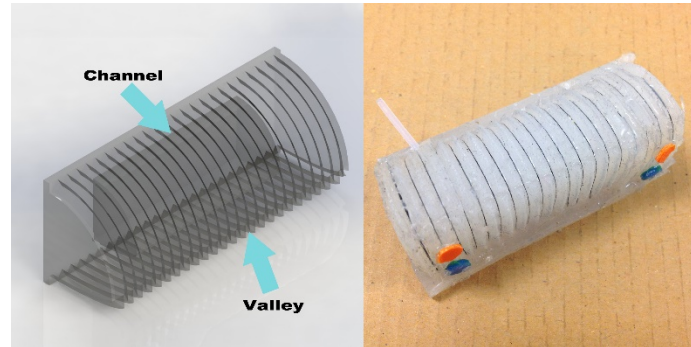


Figure 8 CAD model (Left) and experimental prototype (right) of the second and third generation soft bending actuator.

process of the SRS, which uses four bidirectional bending actuators as segments, consists of four steps as explained below and illustrated in Figure 9.

Step1 Body mold and constraint mold are 3D printed. The body mold has two parts, the holder which has the main shape of the actuator and the cover which helps form the shape of the channel. Constraint mold is a rectangular shell. An inextensible flexible sheet is inserted into the constraint mold. The soft curvature sensor is embedded inside the third generation soft bending actuator instead of the inextensible flexible sheet.

Step2 The silicone is poured into all molds. After the silicone fills the body mold, the cover is placed on top to create the fluidic channel. The silicone cures at room temperature in four hours. Two half bodies and the constraint layer are made at the same time.

Step3 Half bodies are demolded. Nylon thread is tied following circular grooves around the body. A small amount of uncured silicone is brushed to cover the thread to make sure it stays in place attached to the main body.

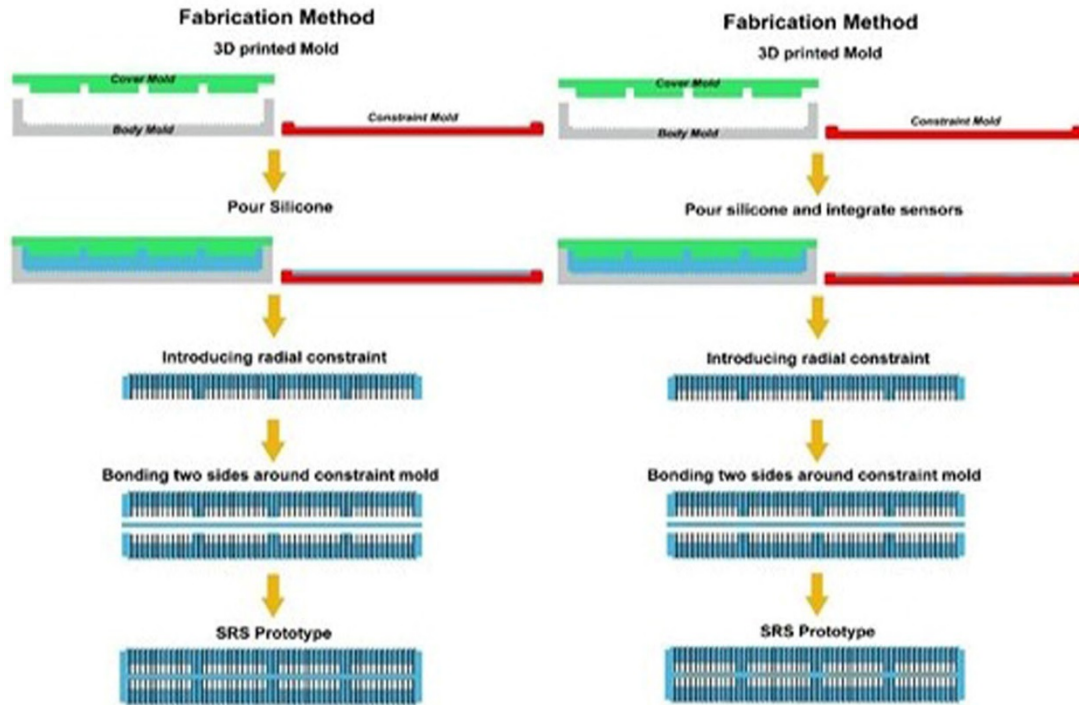


Figure 9 Fabrication process of the second (Left) and third (Right) generation soft bending actuator

Step4 Finally, two half bodies and constraint layer are bonded to each other using a very thin layer of uncured silicone.

2.1.3 Fourth Generation Soft Bending Actuator

Although the second and third generation’s actuators performed better than the old ones and represented a significant advance in multimaterial composite fabrication with the integration of the curvature sensors, they had major reliability problems. The

first cause of this is the connection between the external pressure lines and the soft actuators. This was done by piercing each of the chambers with a sharpened tube after

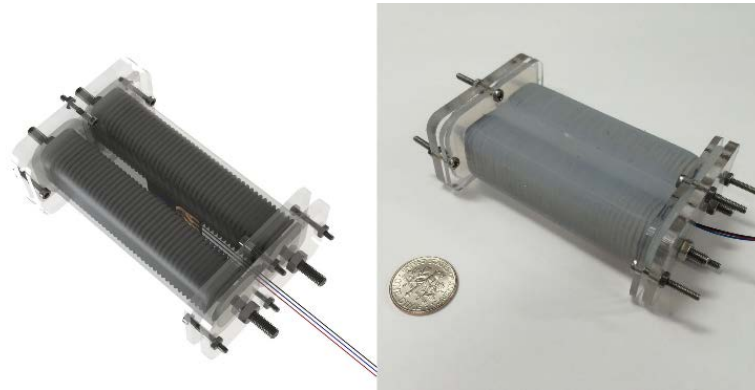


Figure 10 CAD model (Left) and experimental prototype (right) of the fourth generation soft bending actuator with integrated curvature sensing.

fabrication without any additional seal. The other point of failure is the interface between the constraint layer and the soft actuators on either side. The chambers were fabricated separately, and then glued to the constraint layer. The bonded surfaces of the two parts are often not perfectly flat, and imperfections in the adhesion process create weak points in the actuator chamber.

Our soft bending actuator comprises two soft linear muscles and an inextensible constraint layer in between showed Figure 10. The individual linear actuators are made of tubes of silicone rubber wrapped in inextensible thread, which causes them to extend with reduced radial deformation when pressurized. The constraint layer, with a custom integrated curvature sensor, inhibits this linear extension, resulting in the bending of the entire soft module. Caps are attached to both ends of the actuator to seal the chambers and allow for connection with other segments. The caps are made of two acrylic boards sandwiching the rim of the silicone rubber tube to prevent leaking. Thus, the silicone

rubber substrate itself is used as a gasket, eliminating the need for airtight bonds between separate pieces of silicone, a major failure point in the past. Screws are used at either end to allow for easy mounting, with one side using vent screws to allow pressure to be introduced into the chamber. The rectangular external cross section of the actuators reduces potential twisting that occurs at high bending angles and pressure inputs. This actuator is able to reach 90° degree around 9 psi and 70 ml of air volume. The steps of fabrication can be summarized as follows (see Figure 11):

Step 1: Two inner bodies (i.e. linear muscles) of the module are fabricated first using a 3-D printed mold and silicone rubber (Smooth-On Ecoflex 0030).

Step 2: Inextensible sewing thread is wrapped and bonded around each linear muscle.

Step 3: With the flexible curvature sensor in the middle, two pieces of self-adhesive laminate sheet are laser cut and attached together to form the constraint layer.

Step 4: The constraint layer and two inner bodies are placed in a second 3-D printed mold and filled with silicone rubber.

Step 5: Acrylic end-connector caps and vent screws are attached to both ends of the body.

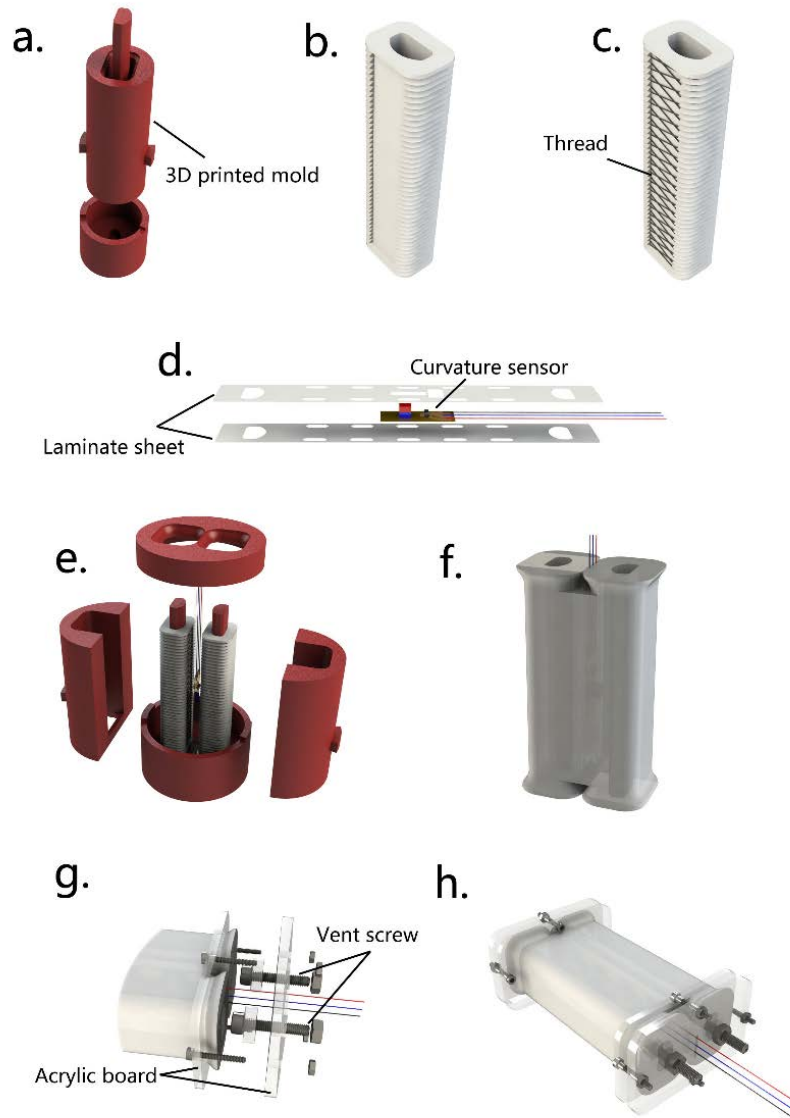


Figure 11 Fabrication process of the fourth generation soft bending actuator

2.2 Proprioceptive Curvature Sensing

In order to sense the kinematic state of our soft snake robot, we have developed a flexible curvature sensor. This consists of a magnet and a Hall Effect sensor mounted on the constraint layer of the snake robot. When the actuator bends, the change in the magnetic field density are sensed by the hall effect sensor can be converted into the curvature of the actuator. In addition, in the center of our robot is an inextensible layer that prevents the segments from extending, constraining the actuator deformation to pure bending. This inextensible layer becomes the neutral axis of bending, subject to no length change and minimal bending stresses. Therefore, this thin center constraint is the optimal location to embed flexible curvature sensors.

Compared to commercial resistive curvature sensors, this sensor offers a fast dynamic response, no nonlinear artifacts, and the ability to customize sensitivity and range in order to measure curvature values according to a variety of task specifications. Compared to optical fiber curvature sensors, our sensor is easier to fabricate and is more scalable. We introduced this unique approach to curvature sensing in. For integration into soft bending modules, our curvature sensors required a few modifications. First, the magnet used is a 0.125 inch cube which forces the entire actuator to be too thick to use as the snake's constraint layer, requiring a reduction in thickness and circuit board stiffness as well as an increase in reliability.

2.2.1 The First Generation Custom Magnetic Curvature Sensor

We proposed the first version of the flexible sensor for soft snake ^[62]. A smaller magnet cube (1/16 inch) was used to reduce the thickness. The sensitivity was also increased to be able to sense the full range of the actuator motion. In addition, the PCB was fabricated out of a Laminate sheet combined with copper foil which greatly reduces the stiffness of the sensor and also provides protection for the traces.

The entire fabrication process consists of five steps, as explained below and illustrated in Figure 12:

Step 1: Circuit traces are designed and printed on a copper film using a solid-ink printer.

Step 2: The patterned copper film is laminated with a thin polyester lamination film on the back side.

Step 3: The copper-polyester laminate is placed in a ferric chloride etching tank, to remove all exposed copper, leaving the electrical traces intact.

Step 4: Another layer of laminating sheet is laser machined to leave mounting and connection holes for discrete components and laminated to the top side of the flexible circuit.

Step 5: Discrete circuit components are soldered, and the miniature magnet is mounted on its precise position under a microscope.

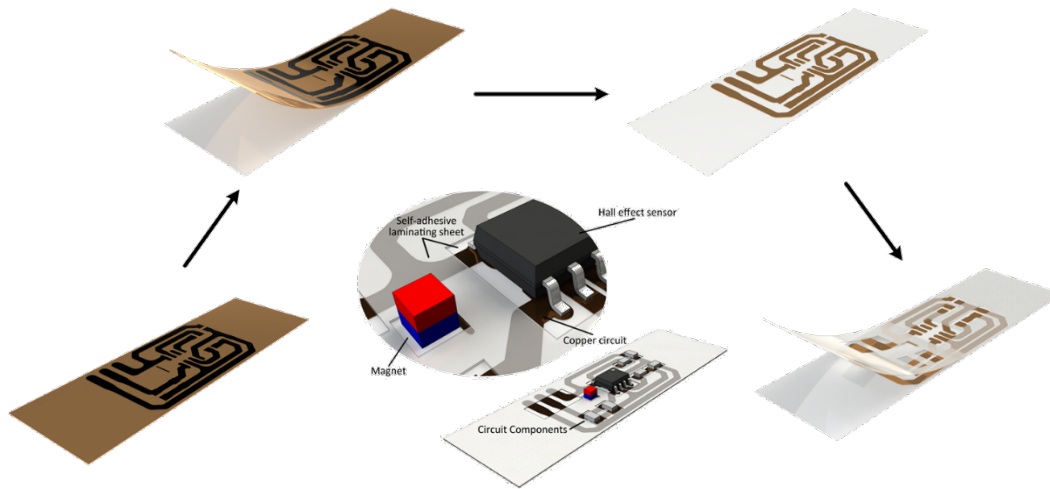


Figure 12 The structure and fabrication of the first version curvature sensor

2.2.2 The Second Generation Custom Magnetic Curvature Sensor

This first generation custom sensor was very fragile because the traces required for the amplification circuit were prone to breaking as the sensor flexed. The circuit contained three layers: two laminate polyester sheets and one copper layer. The melting point of the laminate sheet is very low, which causes difficulties in soldering.

To solve the above issues, we improve our design and produce the third version of the flexible sensor. To further reduce the thickness, we changed to a smaller Hall effect IC (the AH49E) and the cube magnet to a 1/32 inch high cylinder. The new hall effect sensor also allowed us to move the amplification circuit out of the soft actuator which greatly simplifies the design of the circuit and improves the reliability. The PCB material is now Pyralux (3M) which is softer and can tolerate higher temperatures. Figure shows

the circuit design of the new flexible curvature sensor. The entire fabrication process consists of three steps as below.

Step 1 : Circuit traces are designed and printed on a copper-clad flexible substrate (Pyralux, 3M) using a solid ink printer (Xerox Color 8570).

Step 2 : The patterned copper-clad substrate is placed in a ferric chloride etching tank that remove all exposed copper, leaving the electrical traces intact.

Step 3 : Discrete circuit components are soldered and the miniature magnet is mounted on its precise position using a microscope.

We employed finite element analysis (FEA) to improve the design of our curvature sensor. We considered two main parameters: the orientation of the magnet and the distance between the magnet and the Hall element. First, we generated magnetic field data using Comsol, an example of which can be seen in Figure 13(a). We used this to calculate the strength of the magnetic field at the Hall element with respect to the circuit design. Figure 13(b) shows the geometric relationship between the magnet and the Hall element on a bending segment. The origin is located at the base of the magnet, L is the arc-length along the flexible circuit between the origin and the center of the Hall element, h_m is the height of the center of the magnet (point M) and h_s is the height of the Hall Effect sensor element (point S). We assume that the flexible sensor is under constant curvature, allowing us to calculate the positions of these two points. We can then calculate the vector between M and S, magnetic field data B_x and B_y at S, and to determine the expected field registered by the Hall element (in its normal direction) using via the following rotation equation:

$$B_n = B_y \cos\theta - B_x \sin\theta \quad (1)$$

where B_n is the magnetic field density which the one dimensional Hall effect sensor could sense when the bending angle is θ . When analyzing the sensor simulation, we considered the working range of the bending actuator to be ± 90 degrees, representing the bounds of Figure 13(c) shows the model prediction of the magnetic field with respect to curvature at a distance of $L = 3.1$ mm, the results of which can be approximated using a linear fit. In order to determine the optimal distance and magnet orientation, we calculated the range of measured magnetic fields for L ranging between 3.1 to 4.6 mm with the magnetic north pointing upwards (along y-axis) and sideways (along x-axis), the results of which can be seen in Figure 13(d). This range was chosen to keep the sensor from coming into contact with the magnet at larger curvature values, as well as keep the magnetic field from becoming too weak to be measured effectively.

These sensor readings can each be approximated by a linear fit, as in Figure 13(e). We compared the residuals (R^2 values) for these fits for top- and side-facing magnets for the same range of L , representing the linearity of the resulting data. The results of this analysis can be seen in Figure. We conclude that the top-facing magnet orientation is superior, because the working range is larger and the data is more linear. In addition, it is found to be advantageous to minimize L to maximize the range of magnetic field readings.

In previous work, we found that the integrated curvature sensor response was non-monotonic at low actuation pressures, as seen in Figure 14(e). This behavior made parsing the sensor data difficult at low angles, and caused inconsistencies in segment

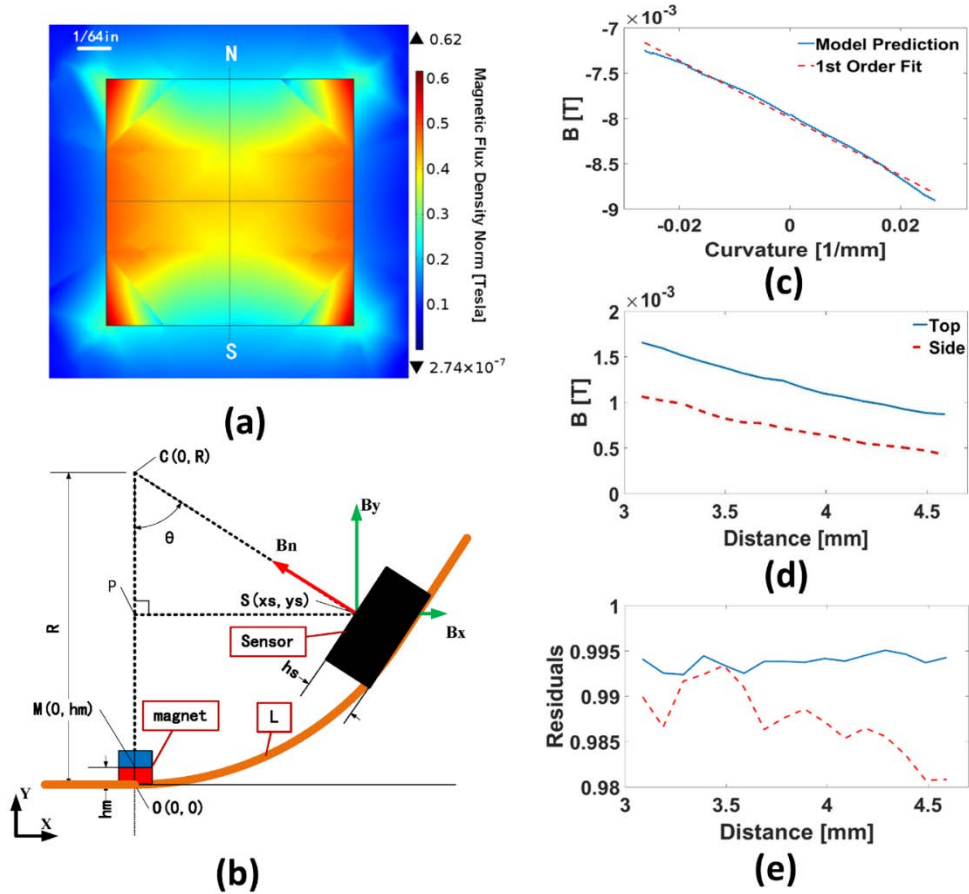


Figure 13 Finite Element Analysis of the flexible curvature sensor. (a) A 2D view of magnetic field vectors from our Comsol simulation. (b) The geometric relation between the magnet and the hall effect sensor. (c) The simulated magnetic field data at the the sensor (Blue solid line) and a corresponding 1st order fit (Red dashed line) as a function of curvature. The magnet is facing out of the sensor (the N direction is upwards) and the distance L is 3.1 mm, (d) The effect of changing L and magnet orientation on measured magnetic field at a 90-degree bending angle. The blue solid line shows the data where the magnet is facing upwards (y -axis) and the red dashed line shows the magnet facing sideways (x -axis, i.e. towards the Hall Effect sensor). (e) The residuals of linear fits on data from (d), representing the linearity of the data.

motion data. We postulate that silicone rubber on the inside edge of an actuator is deforming when pressurized and pressing against the sensor, causing anomalous readings, and that the cross-section of the pressure chamber has a direct effect on this behavior (as pressure is introduced, we expect the rectangular chamber to deform into a circular cross section). An illustration of this behavior for unpressurized and pressurized states of a rectangular cross-section actuator can be seen in Figures 14(a) and (c) respectively.

Thus, in order to prevent this effect, we modified the pressure chamber cross-section to semicircular, which can be seen in Figure 14(b) with its pressurized form Figure 14(d), where it doesn't deform the sensor. We used an external vision tracker to calculate ground truth segment curvatures corresponding to the recorded sensor voltages. Figure 14(e) shows these calibration curves for the two different chamber cross-sections. In addition, we also converted the numerical magnetic flux data to sensor voltage based on the sensitivity of the Hall Effect sensor and the amplification circuit parameters. Again, we observed that the rectangular chamber data is not monotonic at small curvatures, meaning that the sensor is incapable of detecting changing angles at low pressure inputs. The sensor readings with the semicircular cross-section remain injective and more linear. Additionally, the FEA model prediction fits this experimental data much better. This improvement makes the integrated curvature sensor more reliable, precise, and easier to use.

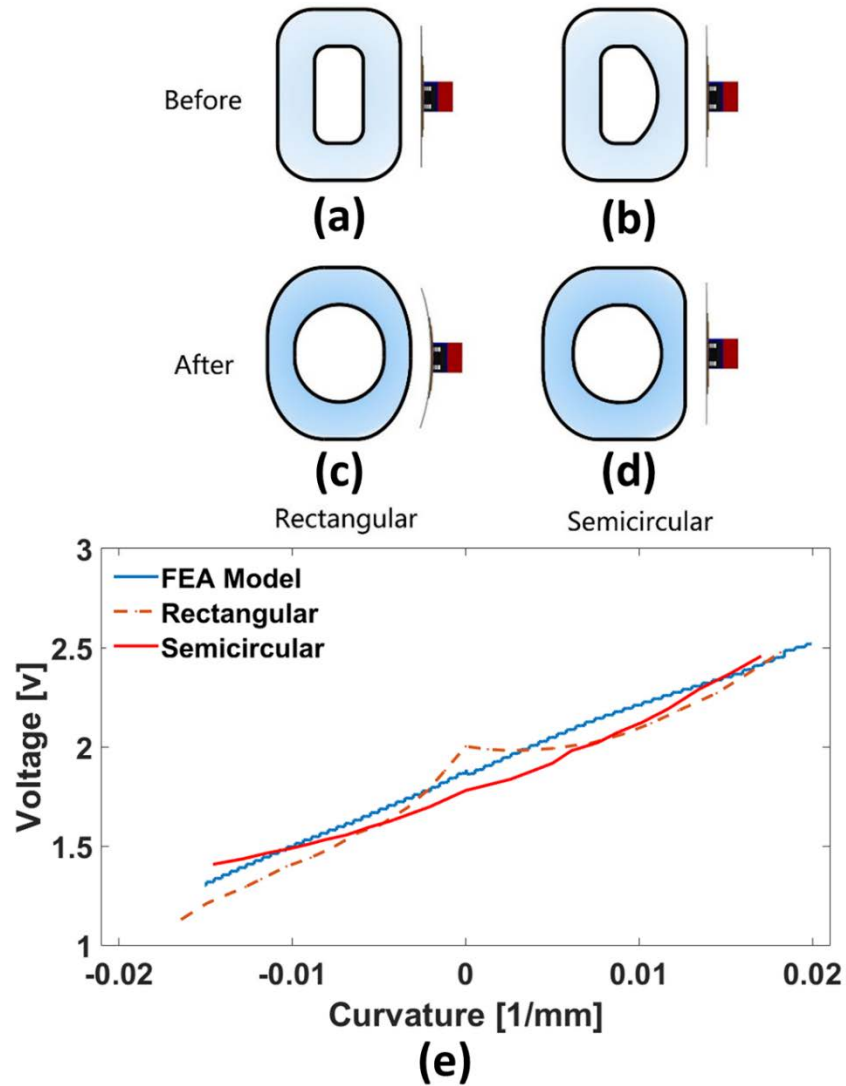


Figure 14 The relationship between the cross section shape of the actuator and the sensor performance. The rectangular (a) and semicircular (b) shapes of the actuator pressure chamber cross section deform into circular shapes upon pressurization in (c) and (d), respectively. Notice that the rectangular chamber in (c) deforms more against the sensor, causing it to bow. The sensor calibration data of the two chamber types in (e) indicate that the proposed semi-circular cross section yields injective response. The rectangular chamber data is not monotonically increasing with bending curvature, making it inappropriate for feedback around small curvature values. The blue solid line is the FEA model prediction.

2.3 WPI SRS System Architecture

2.3.1 The First and Second Generation SRS

The fluidic sub-system, the control sub-system, and the robot itself form the whole tether soft snake robot system as depicted in Figure 15. As a fluid source, we use a shop air nozzle that can provide a large pressure input, which passes through a regulator to obtain controlled pressure values more compatible with our actuators, typically below 10 psi. The regulated pressure input is connected to a valve array that drives the soft snake robot. Each segment of the robot requires two valves to achieve bidirectional bending. The aim of the control system is to move the snake robot in a way that follows the serpentine gait. A NI-DAQ PCI 6009 transfers commands from Matlab to drive each valve. Eight digital outputs of the NI-6009 are used to control eight miniature solenoid valves, turning them on or off.

Experimental data are extracted using an external vision system. Positions of custom color markers placed at both ends of each segment (a total of 10 markers) are measured over time using an overhead camera and an open source visual tracking software.

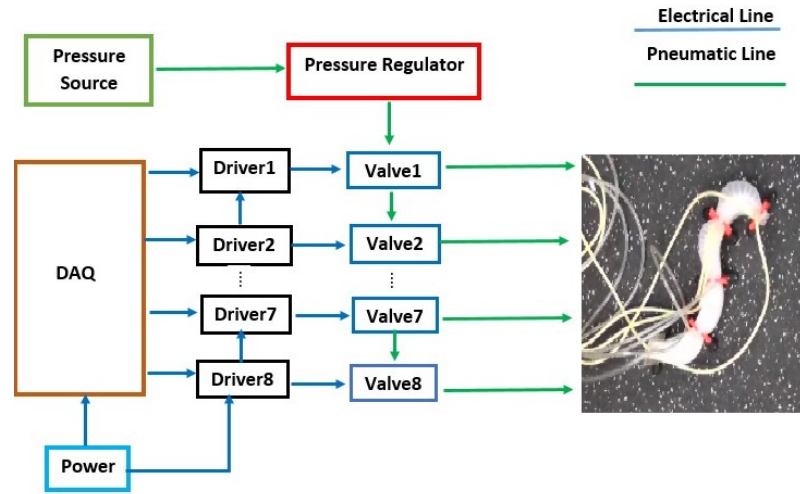


Figure 15 The Experimental System of the Tether Robot (The First and Second Generation)

2.3.2 The Third Generation SRS

Figure 16 shows the system architecture of the tetherless third generation SRS. 3D printed valve and passive wheel holders (links) are placed around the SRS body between each bending module. Passive wheels provide the requisite anisotropic friction between tangential and normal directions of the body. Each miniature solenoid valve, controlled by the Arduino Mini Pro Board, directs pressurized air into a single soft actuator. The pressure source is a Parker C134G-13 compressor embedded at a 3-D printed tail, which delivers up to 16 psi at 2 LPM. To keep the actuators operating within a safe range, the microcontroller sends a pulse width modulation (PWM) signal to the common collector of the compressor to adjust its output pressure. All experimental results that follow utilize a PWM duty cycle of 90%. Analog input pins of the microcontroller read the sensor data from the embedded curvature sensors. The SRS can communicate with a

nearby PC via Xbee wireless communication, which is used to record curvature data and reprogram the microcontroller. In order to verify the performance of the curvature sensor as well as the whole snake, a custom overhead motion capture system using an Optitrack V120-SLIM camera and a large-power infrared (IR) light-emitting diode array are used as a ground truth external measurement system that tracks passive 3 mm IR markers. Two markers are placed at each valve holder and the tail such that the position and angle of each link as well as the bending angle of each actuator can be measured.

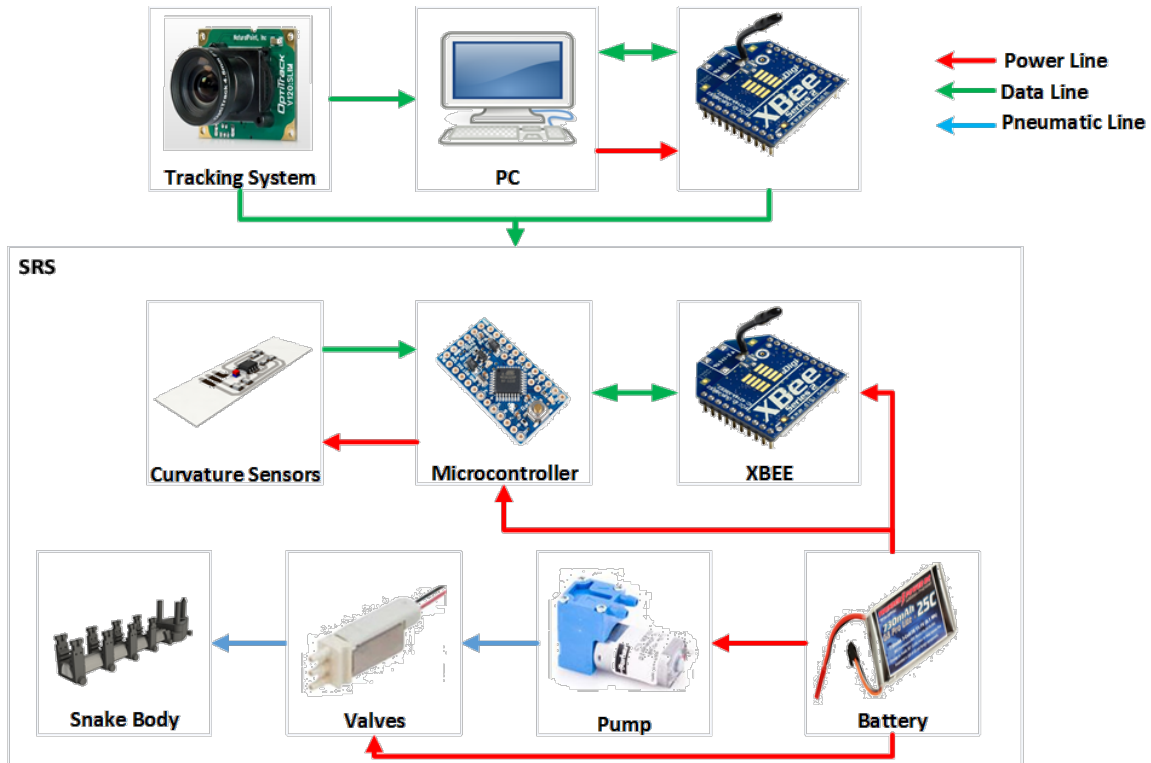


Figure 16 The System Architecture of the untethered third generation WPI SRS.

2.3.3 The Fourth Generation SRS

Figure 17 shows the fourth generation WPI SRS system architecture. Because this version of the WPI SRS is a modularized system, each bending module has an independent slave controller which can receive the curvature sensor data of the bending module and control the two digital solenoid valves which are used to alternately pressurize and vent each actuator chamber. The master controller, located at the tail of the snake, sends commands to the individual segments and receives bending angle data from the slave controllers using I2C serial communication. The pressure source is an external air compressor which we regulate down to 20 psi for the WPI SRS. We put inferred (IR) markers on each bending module, which allowed the external Optitrack tracking system to detect the global position and local state of the WPI SRS global and send it to the control computer. The PC can communicate wirelessly with the XBEE sending control commands and receiving on-board sensor readings.

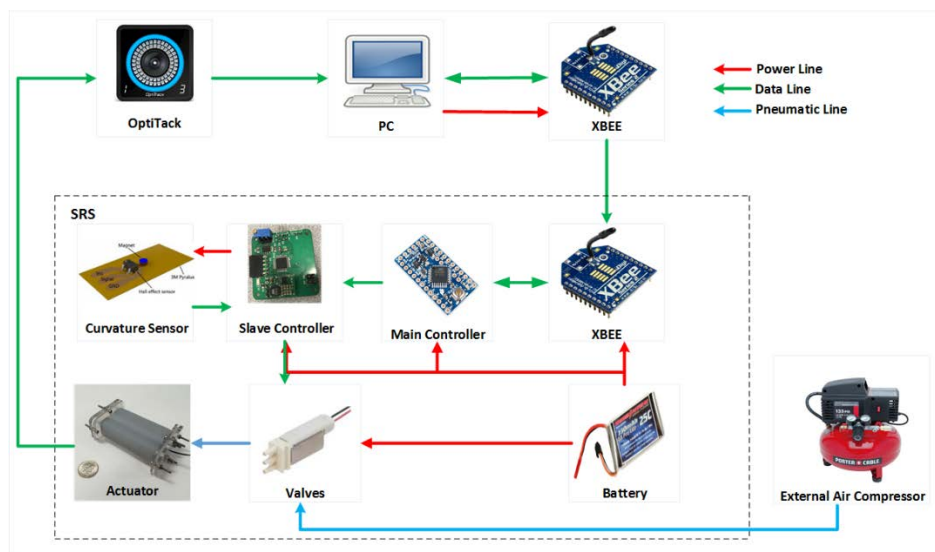


Figure 17 The System Architecture of the modularized fourth generation WPI SRS.

2.4 Discussion and Conclusion

In this section, we introduced the four generation WPI SRS fabrication included the soft bending actuator design and fabrication, the customized curvature sensor design and fabrication and WPI SRS system architecture. The second soft actuator has faster dynamic than the previous version because of the optimal mechanical design which make the second generation WPI SRS has tenth time faster locomotion than the old version. In addition, the latest soft actuator is more reliable and system independent than the previous soft actuator because of the refined fabrication process and its modularity. The curvature sensor which could reflect the actuator's bending angle is easy to be mounted inside the soft actuator as a constraint layer and the linearity of the sensor is very promising based on the optimal numerical analysis.

Chapter 3

3. Modeling and Locomotion Control

For a mobile robot undergoing serpentine locomotion, an accurate dynamic model is a fundamental requirement for optimization, control, navigation, and learning algorithms. Such algorithms can be readily implemented for traditional rigid robots, but remain a challenge for nonlinear and low-bandwidth soft robotic systems. This section addresses the theoretical modeling of the dynamics of a pressure-operated soft snake robot. A general framework is detailed to solve the 2D modeling problem of a soft snake robot, which is applicable to most pressure-operated soft robots developed by a modular kinematic arrangement of bending-type fluidic elastomer actuators. The model is simulated using measured physical parameters of a soft snake robot prototype. The theoretical results are verified through a detailed comparison to locomotion experiments on a flat surface with measured frictional properties. Experimental results confirm that the proposed model describes the motion of the robot accurately.

The outcome of this chapter was published at [89],[91],[92],[93].

3.1 SRS DYNAMIC MODEL

Our first work also presented a complex and simplified theoretical dynamic model of the soft snake robot and experimentally verified its accuracy over linear motion trajectories for the First Generation SRS. This approach treated each soft segment as an actuated bending joint with solid connectors between segments as links. This model combined a kinematic model, inspired by rigid snake modeling efforts with a dynamic model for pneumatic soft actuator. However, the previous model could not predict the rotational motion of the snake, because it didn't take into account the moments caused by frictional forces. Then, we propose a pair of refined snake dynamic models, which include the frictional torque effects. We compare these refined models with experimental results to evaluate their accuracy in predicting linear and rotational motions of the SRS and identify sources of error.

This section proposes a completed model of the soft snake robot. A general soft snake robot comprises N soft segments of length l . For simplicity and practical applications, here are some assumptions:

- The rigid link lengths can be ignored as compared to the length of the soft segments.
- All N connector points have the same moment of inertia J and mass m .

Table 1 lists all the mathematical parameters of the kinematics and dynamics model, which are graphically depicted in Figure. The soft snake robot works on a 2D surface. The following definitions are illustrated similar to a rigid snake robot:

Definition 1 (Link angle): The connector point $i \in (1, \dots, N) \in \mathbb{R}^N$ of the snake robot is noted by $\theta_i \in \mathbb{R}$ with respect to the global x -axis with counterclockwise positive direction.

Definition 2 (Curvature): The curvature of joint $i \in (1, \dots, N - 1) \in \mathbb{R}^{N-1}$ of the snake robot is noted by $\kappa_i \in \mathbb{R}$ is defined:

$$\kappa_i = \frac{\theta_i - \theta_{i-1}}{l}. \quad (2)$$

Given a bidirectional bending module i of length l , out of $N - 1$ modules in series, the normalized arc length $s \in [0,1]$ and a curvature value κ_i , the orientation of this module can be written as:

$$\theta_i = \kappa_i s + \theta_{i+1}. \quad (3)$$

Definition 3 (The global position): The position of the robot with respect to the global frame $\mathbf{p} \in \mathbb{R}^2$ is given by:

$$\mathbf{p} = \begin{pmatrix} p_x \\ p_y \end{pmatrix} = \begin{pmatrix} \frac{1}{Nm} \sum_{i=1}^N m x_i \\ \frac{1}{Nm} \sum_{i=1}^N m y_i \end{pmatrix} = \frac{1}{N} \begin{pmatrix} \mathbf{e}^T \mathbf{X} \\ \mathbf{e}^T \mathbf{Y} \end{pmatrix}, \quad (4)$$

where the vectors: $\mathbf{X} = (x_1, \dots, x_N)^T \in \mathbb{R}^N$, $\mathbf{Y} = (y_1, \dots, y_N)^T \in \mathbb{R}^N$, and $\mathbf{e} = (1, \dots, 1)^T \in \mathbb{R}^N$

Table 1 Parameters of the SRS dynamic model

Symbol	Description
N	Number of links
l	The channel length of the soft segment
m	Mass of each link
J	Moment of inertia of each link
μ_t	Tangential coefficient of friction of each link
μ_n	Normal coefficient of friction of each link
$\theta \in \mathbb{R}^N$	Angle between link i and the global x axis
$\kappa \in \mathbb{R}^{N-1}$	Segment curvature vector
$X, Y \in \mathbb{R}^N$	Link CoM global coordinates vectors
(p_x, p_y)	Global coordinates of the CM of the robot
$T \in \mathbb{R}^{N-1}$	Segment torque input vector
$f_{R,x}, f_{R,y} \in \mathbb{R}^N$	Ground friction force vectors
$h_x, h_y \in \mathbb{R}^{N-1}$	Joint constraint force vectors

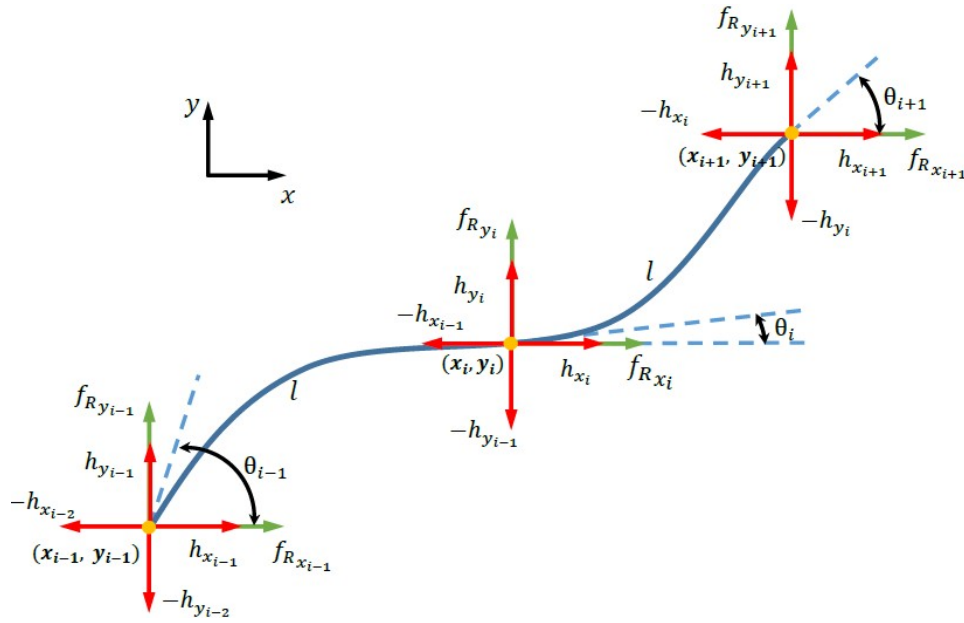


Figure 18 Dynamic force balance between two segments of the SRS.

The complete dynamic model is fundamentally based on the balance of forces and torques for each end of each segment (Figure 18). From this, the force balance equation can be written as:

$$\begin{aligned} m\ddot{\mathbf{X}} + \mathbf{f}_{R,x} &= \mathbf{D}^T \mathbf{h}_x \\ m\ddot{\mathbf{Y}} + \mathbf{f}_{R,y} &= \mathbf{D}^T \mathbf{h}_y \end{aligned} \quad (5)$$

Where

$$\mathbf{D} = \begin{pmatrix} 1 & -1 & & & \\ & \cdot & \cdot & & \\ & & \cdot & \cdot & \\ & & & \cdot & \cdot \\ & & & & 1 & -1 \end{pmatrix} \in \mathbb{R}^{(N-1) \times N}$$

Figure 19 displays the torque balance for each soft segment. F_{Li} and F_{Ri} represent the external forces perpendicular to the moment arm for points A and B on segment i , which include the joint constraint force and friction. Joint constraint forces ensure that two segments remain connected, and frictional forces are anisotropic between the tangential and normal directions. In order to calculate these moment-generating forces, the sum of the joint constraint force and friction in figure should be projected to the moment arm normal direction. The projection angles $\theta_{F_{Li}}, \theta_{F_{Ri}}$ respectively, for A and B can be calculated by:

$$\text{For point } A: \theta_{F_{Li}} = \frac{\pi}{2} + \frac{\theta_{i-1}}{2} + \frac{\theta_i}{2}$$

$$\text{For point } B: \theta_{F_{Ri}} = \frac{3\pi}{2} + \frac{\theta_i}{2} + \frac{\theta_{i+1}}{2}$$

Let $h_{x,i}^*, f_{Rx,i}^*$ be the constraint and friction forces in line with the moment generating force on segment i , written as:

$$h_{x,i}^* = h_{x,i} \cos(\theta_{Ri}) + h_{y,i} \sin(\theta_{Ri}) \quad (6)$$

$$f_{Rx,i}^* = f_{Rx,i} \cos(\theta_{Ri}) + f_{Ry,i} \sin(\theta_{Ri})$$

The length of the moment arm changes as the segment curvature changes.

According to the geometric relation shown in Figure 19, the length of the moment arm is given by:

$$l_i = 2 \left| \frac{l}{\Delta\theta} \sin \frac{\Delta\theta}{2} \right| \quad (7)$$

The approximated inertia of each soft actuator end point is given by:

$$j(i) = \begin{cases} ml_1^2 / 3 & \text{if } i = 1 \\ ml_{N-1}^2 / 3 & \text{if } i = N \\ ml_{i-1}^2 / 3 + ml_i^2 / 3 & \text{otherwise} \end{cases}$$

The moment of inertia matrix of the entire soft snake is, then:

$$J = \begin{pmatrix} j(1) & 0 & & \\ 0 & j(2) & & \\ & & \ddots & 0 \\ & & & 0 & j(N) \end{pmatrix} \in R^{N \times N}$$

Therefore, the torque balance equation for segment i is:

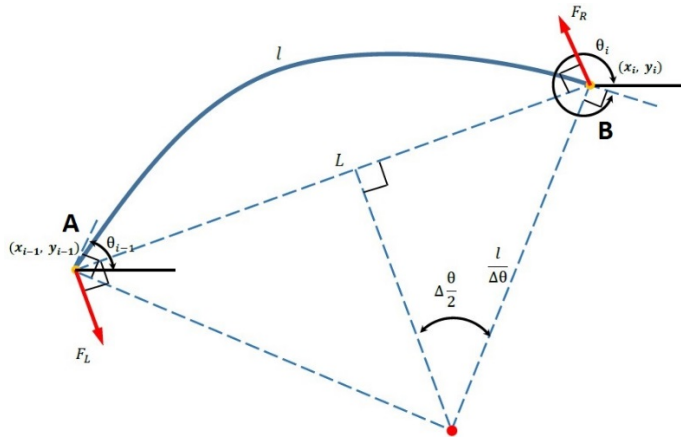


Figure 19 The moment arm of each segment of the SRS varies as a function of bending curvature

$$A_3 = \begin{pmatrix} 0 & 0 & & \\ C_{2,1} & 0 & & \\ & & \ddots & \ddots \\ & & 0 & 0 \\ & & C_{N,N-1} & 0 \end{pmatrix} A_4 = \begin{pmatrix} 0 & C_{1,1} & & \\ 0 & 0 & & \\ & & \ddots & \ddots \\ & & 0 & C_{N-1,N-1} \\ & & 0 & 0 \end{pmatrix} \in R^{N \times N}$$

$$C_1 = \begin{pmatrix} 0 & 0 & & \\ 1 & 0 & & \\ & & \ddots & \ddots \\ & & 1 & 0 \\ & & -1 & 1 \end{pmatrix} C_2 = \begin{pmatrix} -1 & 1 & & \\ 0 & -1 & & \\ & & \ddots & \ddots \\ & & 0 & 0 \\ & & -1 & 1 \end{pmatrix} \in R^{N \times N}$$

We can combine Equation and to yield:

$$\begin{aligned} \mathbf{M}_\theta \ddot{\theta} + \mathbf{W}_\theta \dot{\theta}^2 + \mathbf{G}_\theta \dot{\theta} + \mathbf{M}_\kappa \ddot{\kappa} + \mathbf{W}_\kappa \dot{\kappa}^2 + \mathbf{F}_1 f_{R,x} + \mathbf{F}_2 f_{R,y} &= \mathbf{D}^T \mathbf{T} \\ Nm[\mathbf{X}\mathbf{Y}]^T &= \mathbf{E}^T \mathbf{f}_R \end{aligned} \quad (11)$$

$$\begin{aligned} \mathbf{M}_\theta &= \mathbf{J}\mathbf{I}_N + ml\mathbf{H}_9(\mathbf{D}\mathbf{D}^T)^{-1}\mathbf{B}_1 + ml\mathbf{H}_9(\mathbf{D}\mathbf{D}^T)^{-1}\mathbf{B}_3 \\ \mathbf{W}_\theta &= ml\mathbf{H}_9(\mathbf{D}\mathbf{D}^T)^{-1}\mathbf{B}_3 - ml\mathbf{H}_{10}(\mathbf{D}\mathbf{D}^T)^{-1}\mathbf{B}_1 \\ \mathbf{G}_\theta &= ml\mathbf{H}_9(\mathbf{D}\mathbf{D}^T)^{-1}\mathbf{B}_4 + ml\mathbf{H}_{10}(\mathbf{D}\mathbf{D}^T)^{-1}\mathbf{B}_7 \\ \mathbf{M}_\kappa &= ml\mathbf{H}_9(\mathbf{D}\mathbf{D}^T)^{-1}\mathbf{B}_5 + ml\mathbf{H}_{10}(\mathbf{D}\mathbf{D}^T)^{-1}\mathbf{B}_8 \\ \mathbf{W}_\kappa &= ml\mathbf{H}_9(\mathbf{D}\mathbf{D}^T)^{-1}\mathbf{B}_6 - ml\mathbf{H}_{10}(\mathbf{D}\mathbf{D}^T)^{-1}\mathbf{B}_9 \\ \mathbf{F}_1 &= \mathbf{H}_{11}(\mathbf{D}\mathbf{D}^T)^{-1}\mathbf{D} - \mathbf{H}_{13} \\ \mathbf{F}_2 &= -\mathbf{H}_{12}(\mathbf{D}\mathbf{D}^T)^{-1}\mathbf{D} + \mathbf{H}_{14} \\ \mathbf{E} &= \begin{pmatrix} \mathbf{e} & \mathbf{0}_{N \times 1} \\ \mathbf{0}_{N \times 1} & \mathbf{e} \end{pmatrix} \in \mathbb{R}^{2N \times 2} \end{aligned} \quad (12)$$

$$\begin{aligned} \mathbf{H}_9 &= (\mathbf{H}_3\mathbf{C}_2 - \mathbf{H}_1\mathbf{C}_1), \mathbf{H}_{10} = (\mathbf{H}_4\mathbf{C}_2 - \mathbf{H}_2\mathbf{C}_1), \mathbf{H}_{11} = (\mathbf{H}_3 - \mathbf{H}_1), \\ \mathbf{H}_{12} &= (\mathbf{H}_4 - \mathbf{H}_2), \mathbf{H}_{13} = (\mathbf{H}_7 - \mathbf{H}_5), \mathbf{H}_{14} = (\mathbf{H}_8 - \mathbf{H}_6) \end{aligned}$$

This set of equations provides an accurate mathematical representation of the ideal dynamics of our soft snake robot.

3.2 SRS Locomotion Control

The WPI SRS uses a lateral undulation gait for locomotion. In the SRS, control inputs are the states of the solenoid valves. Each segment is controlled by two parallel solenoid valves operating antagonistically, each controlling a single bending direction. In order to generate a traveling curvature wave, the operation states of the solenoid valves are controlled by:

$$S_i = \text{sign}(\sin(\omega t + \beta_i) + \varphi) \quad (13)$$

Where ω , β_i and φ are the frequency, traveling wave delay, and offset of the i^{th} actuator, respectively. The solenoid valve is open when $S_i > 0$ and is closed otherwise.

3.3 SRS Actuator Dynamic Model System Identification

Based on experimental characterizations, the dynamic response of the actuator behaves as a second-order system:

$$\kappa = C_1 e^{(-t/\tau_1)} + C_2 e^{(-t/\tau_2)} + C_0 \quad (14)$$

where τ_1, τ_2 are time constants and C_0, C_1 and C_2 are constant parameters.

In order to figure out these parameters based on the actuator's dynamic curve. We rewrite the Eq (14) into a general solution of the second order system under constant (step) input:

$$\ddot{\kappa} + a\dot{\kappa} + b\kappa = c \quad (15)$$

With the boundary condition $\kappa(t = 0) = 0$ and $\dot{\kappa}(t = 0) = 0$ and where t is the time. The relationship between the coefficients in Eq (14) and (15) can be described as follows:

$$C_0 + C_1 + C_2 = 0 \quad (16)$$

$$\frac{C_1}{\tau_1} + \frac{C_2}{\tau_2} = 0$$

$$a = \frac{1}{\tau_1 \tau_2}$$

$$b = \frac{1}{\tau_1} + \frac{1}{\tau_2}$$

$$c = \frac{C_0}{\tau_1 \tau_2}$$

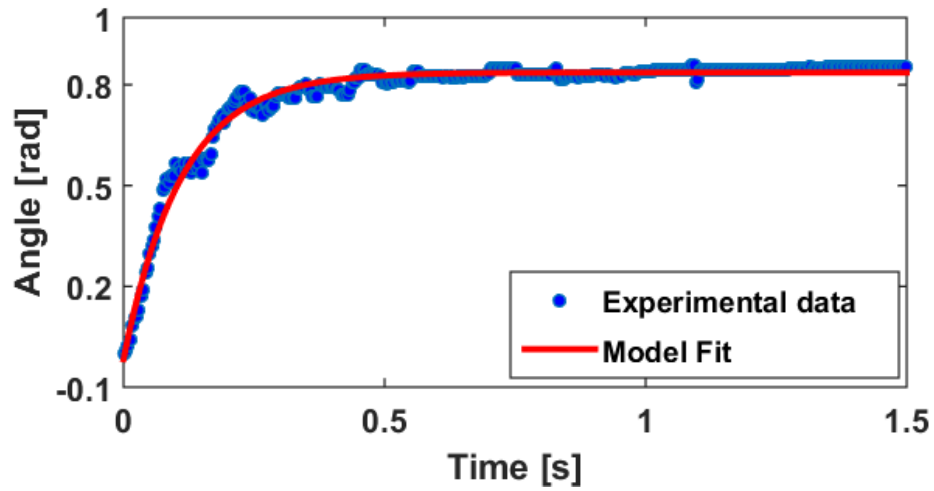


Figure 20 The dynamic response of the fourth generation soft actuator under 8 psi

The Figure 20 shows the fourth generation actuator dynamic behavior when actuated around 8 psi. The time constants: $\tau_1 = 0.1107$, $\tau_2 = 0.0021$. The offset constant: $C_0 = 0.8366$ $C_1 = 0.8531$ $C_2 = 0.0165$ Based on the Eq (16), $a = 4221.8$, $b = 476.4912$, $c = 3532.2$.

3.4 Model Experimental Verification

This section verifies the presented model through the comparison of numerical simulations with experimental results. The body of the soft robotic snake prototype comprises four bidirectional fluidic elastomer actuators as segments composed in series. To verify our modeling approach we performed simulations of the simplified soft snake robot dynamic model. The simulation Adopt the ODE toolbox in Matlab to solve the differential equations of the soft snake robot model. Since solenoid valves switch between on and off positions, the dynamic response of fluidic elastomer actuators used as segments in our robot is also taken into account for step pressure inputs. To compare our model with experimental results, physical parameters of the snake robot prototype and the workspace, we utilized a “spring car”, which included a spring of known stiffness, a linear potentiometer, and passive wheels. As the contact forces are gradually increased, the car starts moving. To simulate friction forces in both tangential and normal directions with respect to the snake body, we recorded the largest deformation of the spring ΔL_{max} , when wheels are freely rotating and when they are fixed. The friction coefficients were simply calculated as:

$$\mu = \frac{k\Delta L_{max}}{mg} \quad (17)$$

3.4.1 The First Generation SRS

Figure 21 displays simulation results including the initial and final positions of the snake body as well as the trajectory of the head. The following set of parameters were used in these simulations: $N = 5$, $l = 0.025m$, $m = 0.1kg$, $U_t = 0.1$, $U_n = 0.9$. In this demonstration of the model, the input pressure value, $P = 3.75 \text{ psi}$, $\omega = \frac{2\pi}{3}$, and $\beta_i = 2\pi \frac{i}{N} \text{ rad/s}$. Figure 21 displays the position and velocity of the CoM of the soft snake robot for the same simulation.

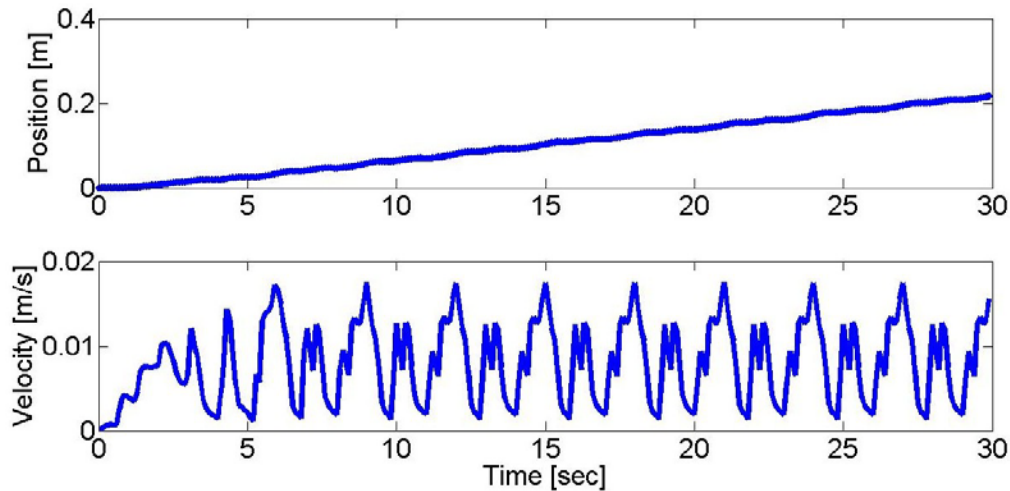


Figure 21 Position and velocity of the simulated soft snake robot center of mass (CoM) over time for the numerical simulation results.

Table 2 displays a list of measured parameters. We used a spring scale to measure the friction factors in two orthogonal directions (normal and tangential to the body axis) by recording the force from the spring scale as the robot began to move upon horizontal pulling. In addition, in order to measure the sliding friction in the normal direction, the passive wheels of the snake were fixed before the measurement. We repeated the

Table 2 First Generation WPI SRS Experimental Parameters

Symbol	Description	Value	Unit
N	The number of links	5	
G	The weight of each soft segment	0.25	kg
U_t	The friction factor in the tangential direction	0.0966	
U_n	The friction factor in the normal direction	0.68	
α	Amplitude	68	rad/mm
T	Undulation period	$\frac{2\pi}{3}$	rad/s

measurements 10 times for both the tangential rolling friction and normal sliding friction cases. The mean friction coefficient values in tangential and normal directions were 0.0966 and 0.68, respectively, with standard deviations of 0.0015 and 0.01.

Experimental data is extracted using an external vision system. Positions of custom color markers placed at both ends of each segment (a total of 10 markers) are measured over time using an overhead camera and an open source visual tracking software. Using two markers at each end of the segments, we can readily extract their average position and orientation, which were further processed in Matlab to calculate the curvature of each bending joint (segment) and the velocity of the center of mass of the whole robot.

After an initial calibration of the tracking software, the position of each marker can be extracted with respect to the global coordinate frame. Based on the position and orientation information at both ends of each segment, we can calculate the curvature value as shown in Table 3 and Figure 22 (a). For comparison with the simulated snake body, Table 4 and Figure 22 (b) describe the recovery of the soft segment shape based on the extracted positions and calculated curvature values.

Algorithm 1 Segment curvature extraction.

Require: Position of two points at each end of the segment:

$$A_1(x_1, y_1), A_2(x_2, y_2) \text{ and } B_1(x_3, y_3), B_2(x_4, y_4)$$

Require: Segment length: l .

1. The slope of point A: $\theta_A = \arctan \frac{(y_2 - y_1)}{(x_2 - x_1)}$
 2. The slope of point B: $\theta_B = \arctan \frac{(y_4 - y_3)}{(x_4 - x_3)}$
 3. The curvature of segment from A to B: $\kappa_i = \frac{\theta_A - \theta_B}{l}$
-
-

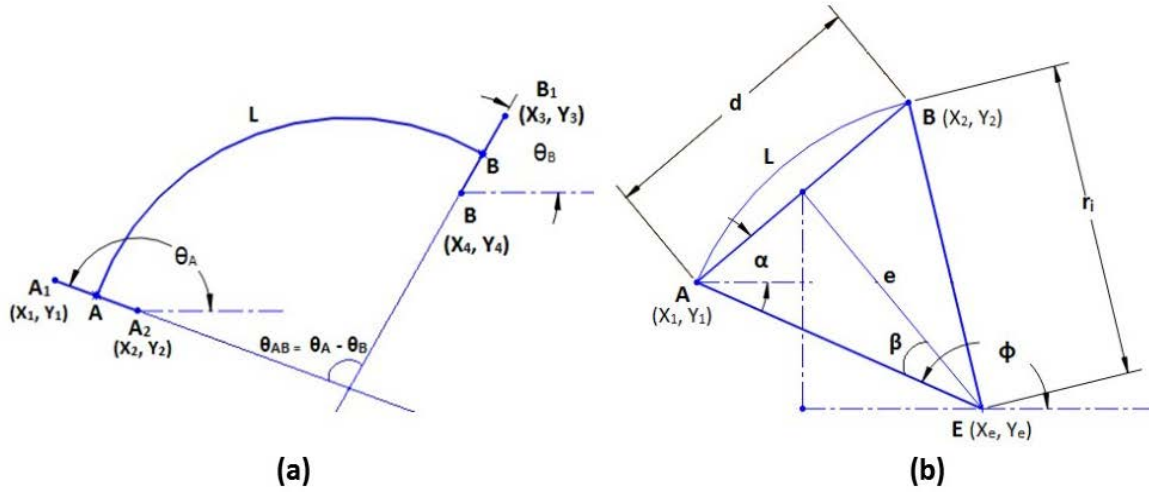


Figure 22 Experimental information is processed for comparison with simulated results. (a) Curvature information is extracted from the positions and orientations of both ends of each segment. (b) The recovered segment shape when $r_i > 0$

Algorithm 2 Recovery of the shape information of a soft segment

Require: Position of two points at each end of the segment:

$$A_1(x_1, y_1), A_2(x_2, y_2) \text{ and } B_1(x_3, y_3), B_2(x_4, y_4)$$

Require: Curvature of the segment: κ_i .

1. Position of point A: $A(x_A, y_A) = \left(\frac{x_1+x_2}{2}, \frac{y_1+y_2}{2}\right)$
 2. Position of point B: $B(x_B, y_B) = \left(\frac{x_3+x_4}{2}, \frac{y_3+y_4}{2}\right)$
 3. The radius of curvature of the segment: $r_i = \frac{1}{\kappa_i}$
 4. The angle of the line AB: $\alpha = \arctan\left(\frac{y_B - y_A}{x_B - x_A}\right)$
 5. The mid-point position between A and B: $x_c = \frac{x_A + x_B}{2}, y_c = \frac{y_A + y_B}{2}$
 6. The distance between A and B: $d = \sqrt{(x_B - x_A)^2 + (y_B - y_A)^2}$
 7. The half arc-angle β : $\beta = \arcsin \frac{d/2}{r_i}$
 8. The distance between the mid-point and the center of curvature point is $e = \sqrt{r_i^2 - \frac{d^2}{4}}$
 9. **If** $r_i = 0$ **then**
 10. Draw a straight line between point **A** and **B**
 11. **else if** $r_i > 0$ **then**
 12. The center of curvature point **E** position $x_e = x_c + e \sin(\alpha), y_e = y_c - e \cos(\alpha)$
 13. The angles of lines **EA**, **EB** are $\phi_A = \frac{\pi}{2} + \alpha + \beta, \phi_B = \frac{\pi}{2} + \alpha - \beta$
 14. Draw the arc based on the equations $x = x_e + r_i \cos(\phi_{AB}), y = y_e - r_i \sin(\phi_{AB}), \phi_{AB} = \phi_A : \phi_B$
 15. **else if** $r_i < 0$ **then**
 16. The center of curvature point **E** position $x_e = x_c - e \sin(\alpha), y_e = y_c + e \cos(\alpha)$
 17. The angles of lines **EA**, **EB** are $\phi_A = \frac{\pi}{2} + \alpha - \beta, \phi_B = \frac{\pi}{2} + \alpha + \beta$
 18. Draw the arc based on the equations $x = x_e + r_i \cos(\phi_{AB}), y = y_e - r_i \sin(\phi_{AB}), \phi_{AB} = \phi_A : \phi_B$
 19. **end if**
-

Therefore, using only marker positions obtained through visual feedback, these algorithms calculate the required information of the position, orientation, and shape of the soft robotic snake prototype. Figure 23 displays the recovered information overlaid with the original frame, following the snake motion in the experiment.

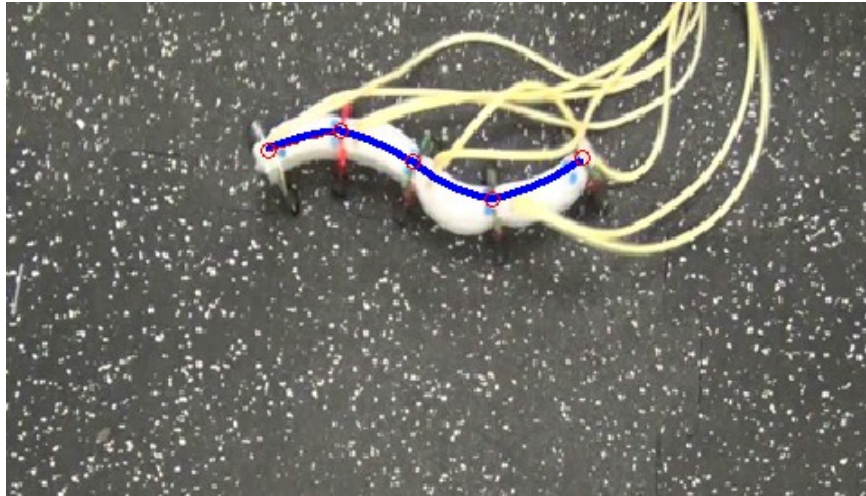


Figure 23 The overlaid curve on the soft snake robot indicates the recovered shape and position of the snake from visual feedback

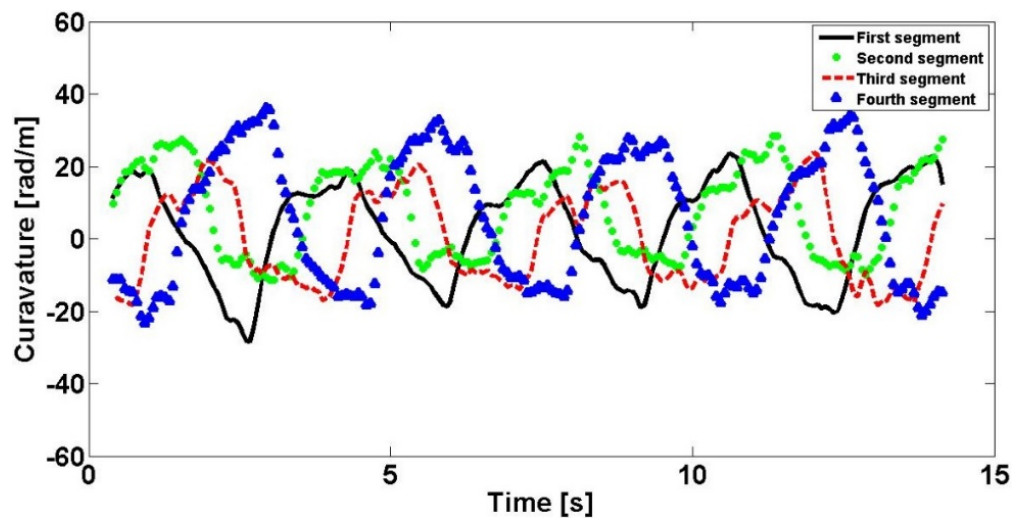


Figure 24 The curvature plot of each soft segment in the experiment. The solid line, circle, dashed line, and triangle represent the 1st, 2nd, 3rd, and 4th soft segments, respectively.

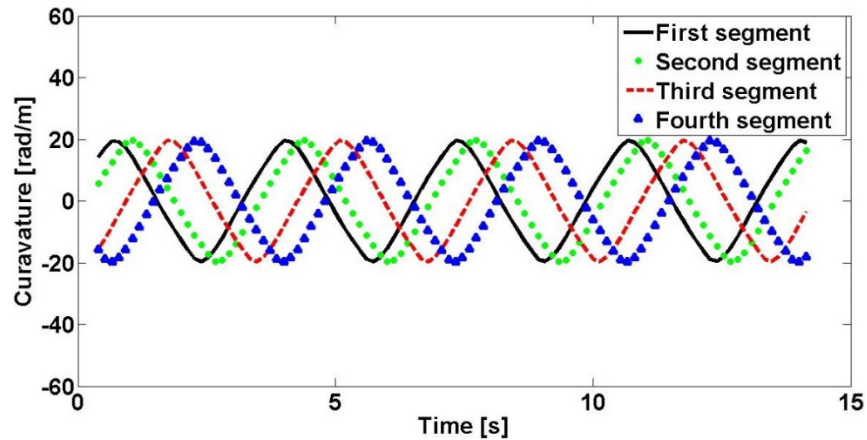


Figure 25 The curvature plot of each soft segment in the simulation. The solid line, circle, dashed line, and triangle represent the 1st, 2nd, 3rd, and 4th soft segments, respectively.

Based on image processing results, Figure 24 shows the curvature plot of each soft segment during an undulation experiment. There are four soft segments, which are shown with different curves in the figure. From this figure, the amplitudes and offsets of curvature waveforms of each soft segment are close but display variation, and the phase offsets between neighboring segments are also not constant. These variations are primarily due to small non-uniformities in fabrication, as well as variations in fluidic impedance between segments, surface flatness, and the effect of tubing. As a result, the snake robot has a tendency to move in a large circle instead of a straight line, which will be addressed via feedback control elsewhere.

In comparison, the simulated curvature plots of each soft segment are shown in Figure 25 using the same parameters as for the experiments. These curves display approximate sinusoidal waveforms as square wave pressure inputs are smoothed by the segment dynamics.

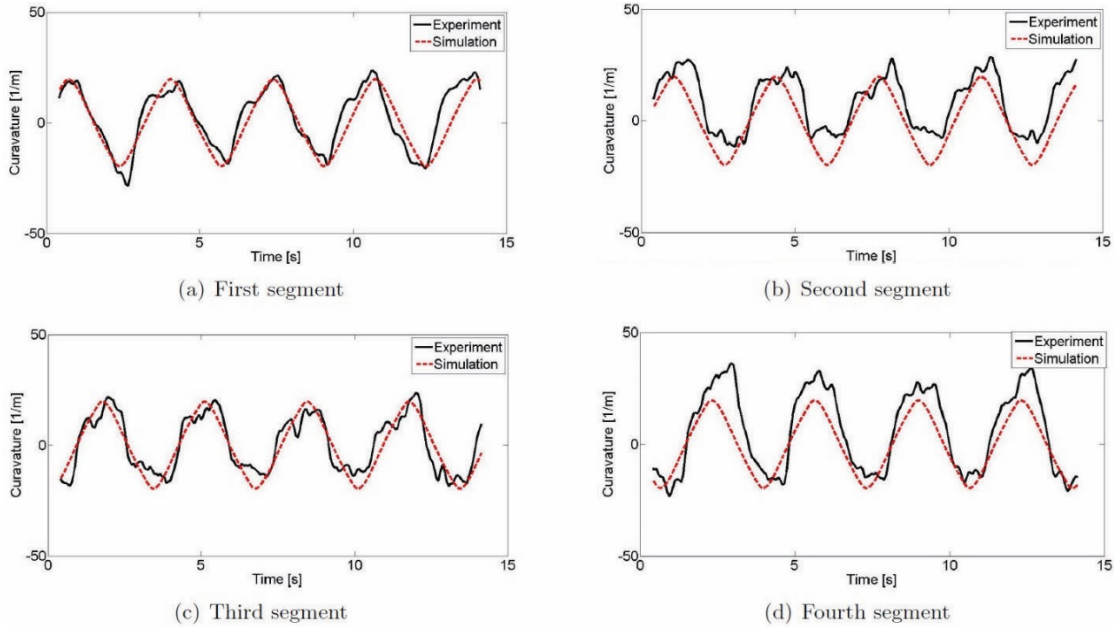


Figure 26 Curvature waveforms of each segment in the experiment (solid line) and the simulation (dashed line).

Experimental curvature measurements are directly compared to simulation results in Figure 26 for all segments. Dashed lines represent simulations and solid lines represent experimental results. All $N - 1$ curvatures can be directly controlled by independent pressure inputs in a similar manner by switching solenoid valves and relying on the segment dynamics. These curves indicate a good match between model predictions and experimental results.

To compare the simulated and experimental shape of the snake robot over time we adopted a local frame method. Placing a coordinate system at the center of mass of the snake robot with zero heading angle (defined as the average orientation of the body), we achieved a standard way to focus only on the shape information. Figure 27 shows the shape of the soft snake robot body for both the experiment (solid) and the simulation (dashed) on the same plane at four sample points in time.

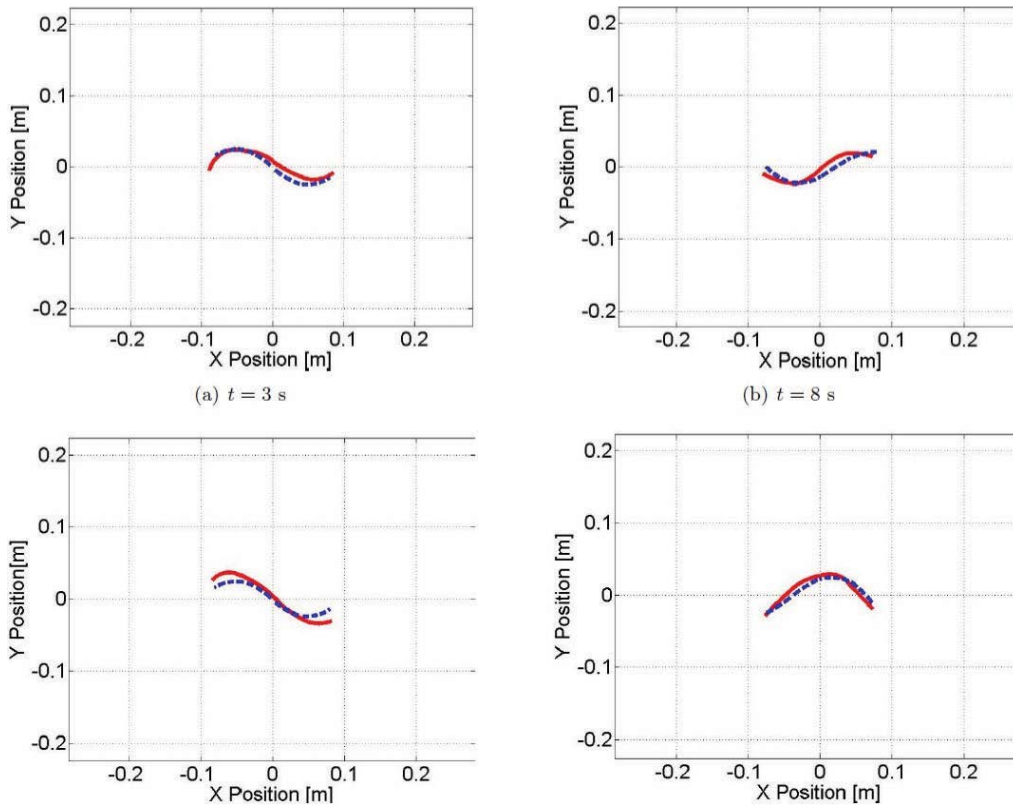


Figure 27 Comparison of the snake robot shapes between the simulation and the experiment at 3, 8, 13, and 16 s. The dashed line shows the simulation and the solid line shows the experimental results.

The root-mean-square (RMS) error due to the shape differences between the theoretical model prediction and experimental measurements during the whole motion is displayed in Figure 28. The total length of our snake robot is 0.24 m and the mean RMS error is 0.0138 m, approximately 5.75% of the body length indicating good accuracy. There are a number of experimental sources of error in the body shape. The snake robot is expected to follow a straight line, but turns slightly during locomotion; curvature amplitudes are not constant among segments; tubings cause external force; and the constraint layer is not located precisely in the middle of the body.

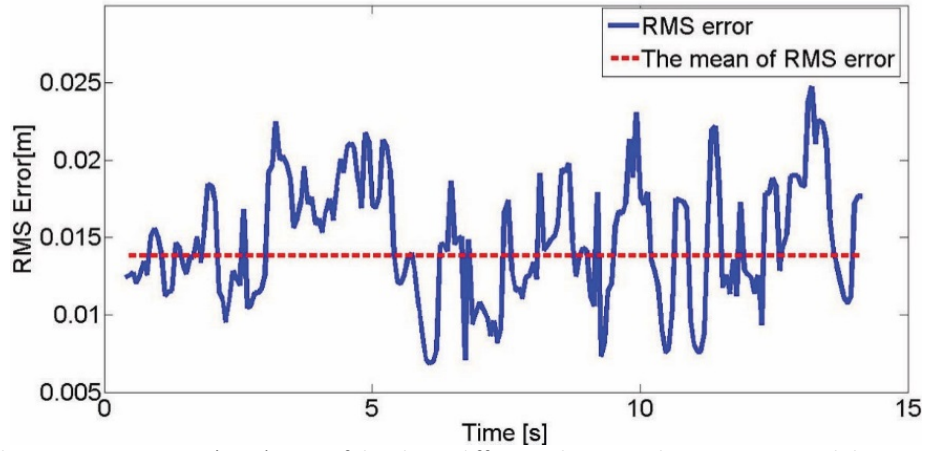


Figure 28 The root-mean-square (RMS) error of the shape difference between the experiment and the simulation.

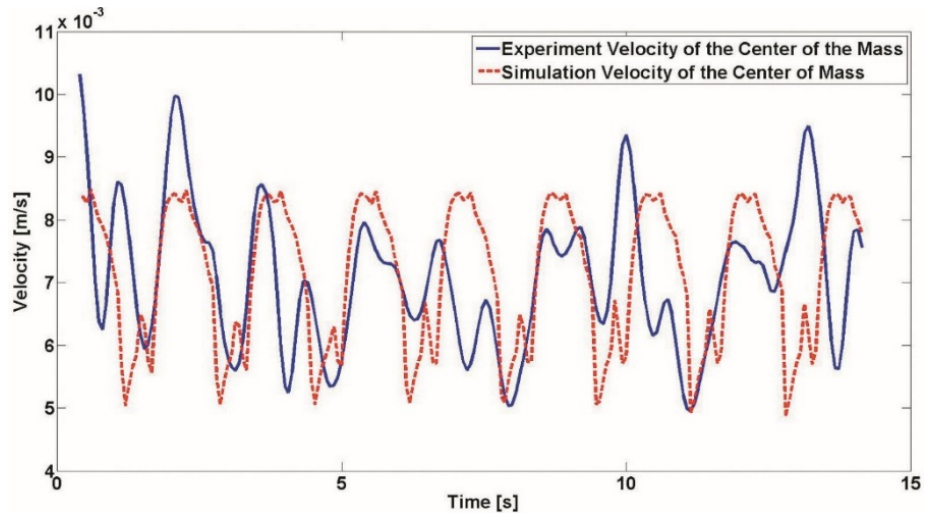


Figure 29 The root-mean-square (RMS) error of the shape difference between the experiment and the simulation.

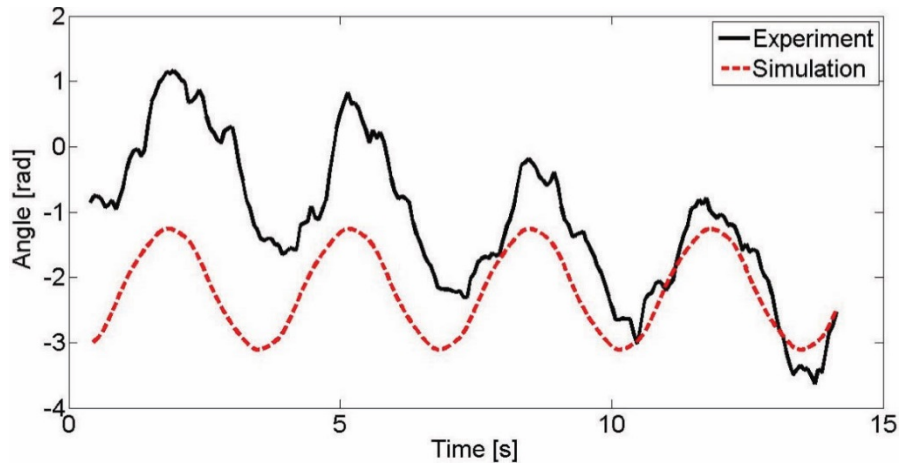


Figure 30 The root-mean-square (RMS) error of the shape difference between the experiment and the simulation.

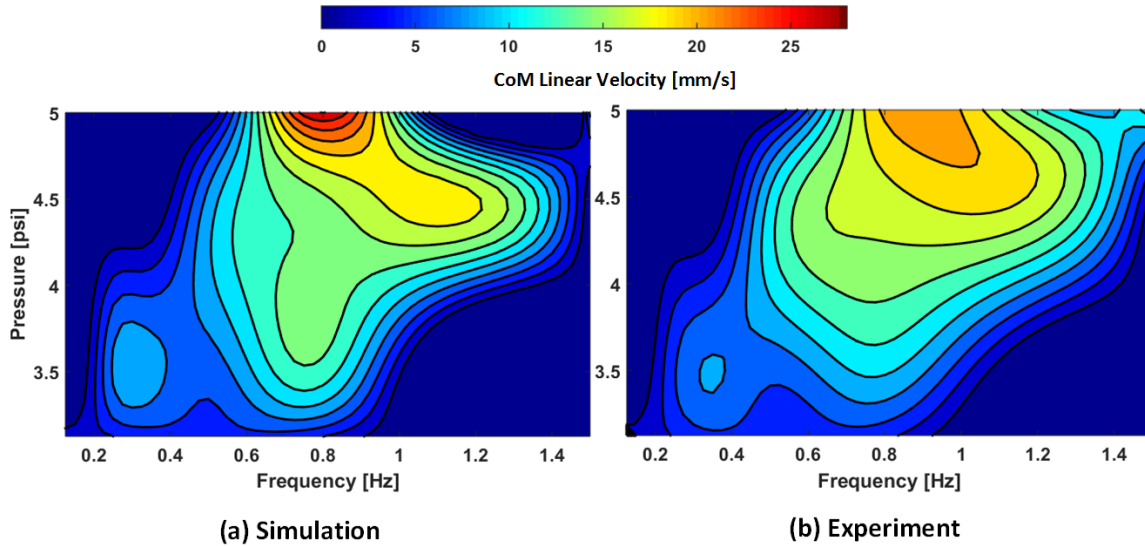


Figure 31 Comparison of model predictions and experimental results for different operational parameters of the soft robotic snake in terms of resulting CoM velocities. Contour plots of the linear velocity of the robot CoM with varying frequencies from 0.16 to 1.5 Hz (x-axis) and pressure inputs ranging from 3.125 to 5 psi (y-axis) are displayed for simulation (a) and experimental (b) results. The CoM velocity levels are stepped at 2 mm/s, annotated on the curves, and indicated as color coding from blue to red.

Linear velocity of the snake robot is determined by the center of mass position over time. Noise in experimental results was reduced using a moving line fit around the current point in time. With a 15 fps camera feed, we used the position information from five frames before and after the current frame and used the slope of the best fit line as the extracted velocity. This method reduced oscillations due to tracking pixel variations between segments while not inducing lag. Figure 29 displays the velocities of the center of mass for the snake robot from both experimental (solid) and simulation (dashed) results. From this figure, a periodicity of velocity is observed around a similar average linear velocity, in line with our model predictions.

Figure 30 shows the rotational angle of the tail for simulated (dashed) and experimental (solid) results. Please note that this angle cannot be directly controlled. If the snake robot follows a straight line in a global coordinate, then the sum of all rigid link

angles should be equal to 0. Hence, this uncontrolled value provides a good indicator of the overall orientation of the robot body over time. For no rotation, the tail angle should oscillate around a constant offset value with no linear change with time, which is the case for the simulation results. However, in the experiment, the snake turns over time, indicated by a drift in the tail angle offset.

To evaluate the strength of the model to describe the behavior of our soft robotic snake, we performed a comparison of simulation and experimental results within the feasible operational parameters of the driving frequency of the curvature waveform and pressure input values, which are directly related to the curvature amplitudes in serpentine locomotion. The resulting CoM velocities for each of these parameter combinations are shown in Figure 31 as contour plots for the simulated model predictions and experimental results. Pressure is varied from 3.125 psi to 5 psi and the frequency is varied from 0.33 Hz to 3 Hz. The results confirm that the model predictions are in line with experimental observations, subject to associated uncertainties.

Two cases of parameter combinations are not investigated. Low frequency and high pressure case would build up too much pressure in the actuators for a long period causing potential rupture. High frequency and low pressure case immobilizes the snake robot since the incoming fluid is released quickly before deformation can be observed. Simulations generated combinations of 56 frequency and 31 pressure values within the given ranges. We performed each experiment three times and removed any outliers before calculating the average values. The information between the measurement points is extracted through interpolation.

3.4.2 The Second Generation SRS

Table 5 Experimental Parameters of the Second Generation SRS

N	l	m	μ_t	u_n	β_i
5	0.037m	0.03kg	0.043	0.57	$\frac{2\pi l}{N-1}$

Table 5 shows the experimental measured parameters. To evaluate the strength of the refined model in describing the dynamic behavior of our soft robotic snake, we compared the model performance to that of the physical SRS. Figure 32 displays contour plots of CoM velocities for the simulated model predictions and experimental results when offset $f = 0$. Input pressures ranged from 41 to 55 kPa and the frequency ranged from 1 to 2 Hz. SRS travels in a straight line when $f = 0$. The maximum linear velocity is around 220 mm/s which is ten times faster than the previous snake robot. The results shows that both model predictions are similar to the experimental results with the complex model being slightly closer.

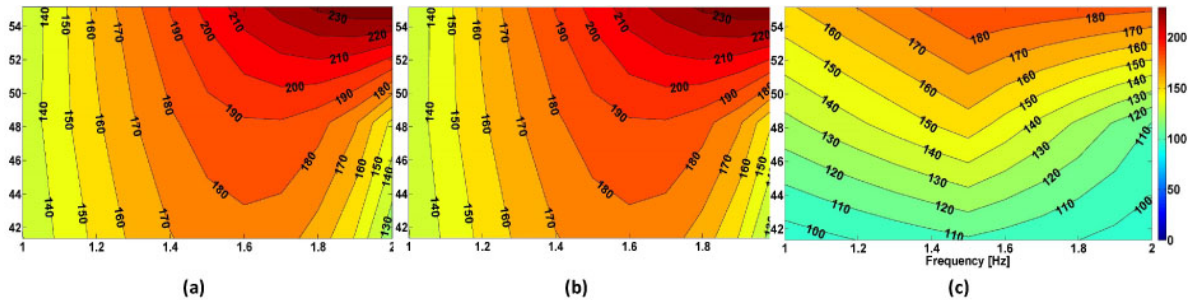


Figure 32 Comparison of model predictions and experimental results for different operational parameters of the soft robotic snake in terms of the soft robotic snake in term of resulting CoM velocities and trajectory radii with the offset term $\phi = 0$. The frequencies from 1 to 2 Hz(x-axis) and pressure inputs ranging from 41 to 55kpa (y-axis). (a),(b),(c) are the CoM velocities for complex model simulation, simplified model simulation, and experimental turning radius of the CoM when $\phi = 0.4$.

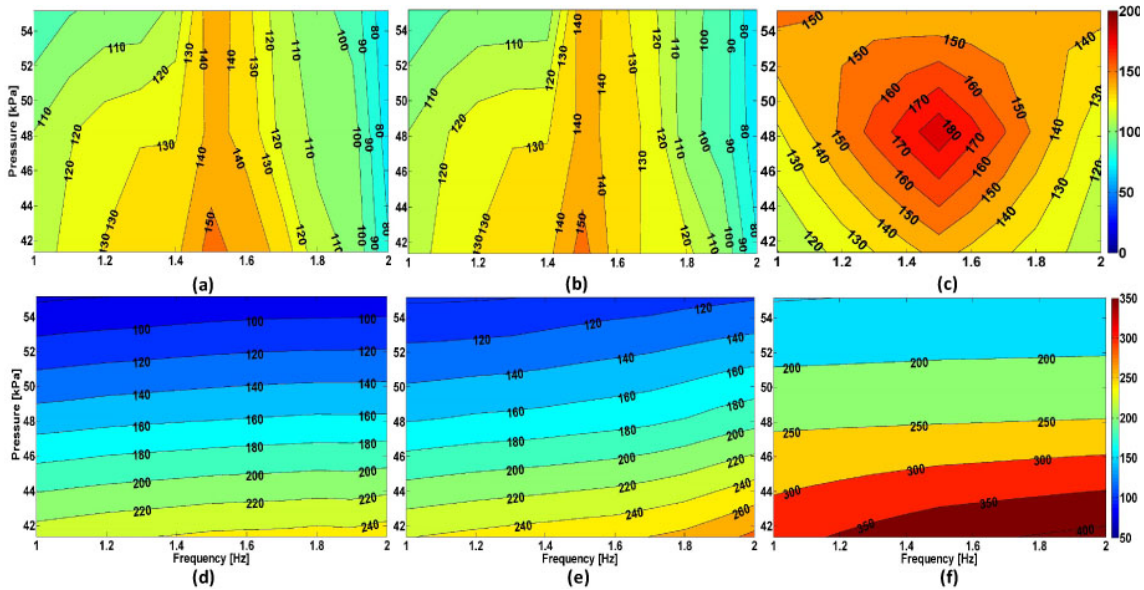


Figure 33 Comparison of model predictions and experimental results for different operational parameters of the soft robotic snake in terms of the soft robotic snake in term of resulting CoM velocities and trajectory radii with the offset term $\phi = 0.4$. The frequencies from 1 to 2 Hz(x-axis) and pressure inputs ranging from 41 to 55kpa (y-axis). (a),(b),(c) are the CoM velocities for complex model simulation, simplified model simulation, and experimental turning radius of the CoM when $\phi = 0.4$. (d),(e),(f) shows the complex model simulation, simplified model simulation, and experimental turning radius of the CoM when $\phi = 0.4$.

Figure 33 (a-c) shows the contour plots of CoM velocities for the simulated model predictions and experimental results when offset $\phi = 0.4$. While the general behavior is captured by both models, the simplified model seems to predict the CoM velocity better for the offset value. The differences that exist between the two predictions and experimental results are likely caused by several factors, including measurement error, fabrication inconsistencies, and the forces due to external tubing, especially for rotation motion. The snake was driven by an external air pressure source and the weight and friction of the required tubing was likely a factor in skewing the results of this experiment. In addition, the fabrication inconsistencies caused the constraint layer between the two halves of the body to have a non-trivial and varying width, changing the behavior of the snake.

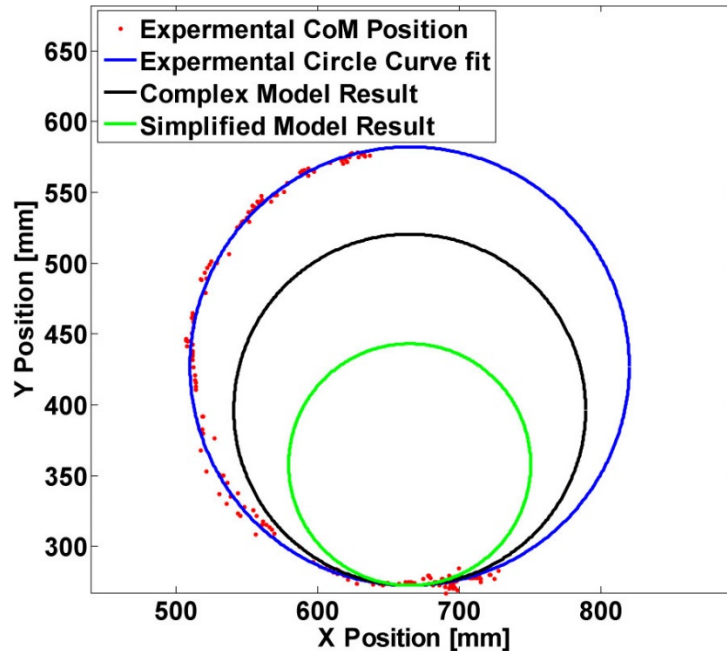


Figure 34 A plot of the experimental trajectory (red dots) and fit line (blue line) compared to the complex and simple model trajectories (black and green lines) with frequency 2 Hz and input pressure 54 kPa.

Figure 33 (d-f) shows the contour plots of the turning radius for the same simulated model predictions and experimental results when offset $\phi = 0.4$. Similarly, a strong dependence of turning radii values on input pressure is revealed for all cases, but predictions are off by wide margin. Figure 34 shows the center of mass trajectory from the motion capture system and its corresponding circle fit alongside the predicted trajectories with frequency 2 Hz and input pressure 54 kPa. In the simulation, the length l of each segment was also assumed to be the length of the pressure chamber assuming the gap between the channels are negligible. However, these unactuated portions do not provide torque and impede the actuator bending, which reduces the SRS' ability to turn (see Figure). Therefore, we choose a correction factor $((l + L_o)/l)$ that represents the ratio of the total segment length including the gap, divided by the length of the channel. We multiplied this factor with the measured radius values (or rotational velocities) in the

simulation results. The experimental turning radius values are still larger than the predictions of the two models, with the complex model results being closer. One of the reasons for this mismatch, in addition to experimental errors mentioned above, is that the models do not include the passive bending forces occurring at these portions, which act to reduce actuator bending curvatures and increase turning radii. Nevertheless, these investigations indicate that, through an initial calibration routine, the proposed models are strong enough to predict the CoM motions of the SRS following non-linear trajectories as a level of abstraction to a non-holonomic differential drive mobile robot, which in turn, makes planning and higher-level control tasks easier.

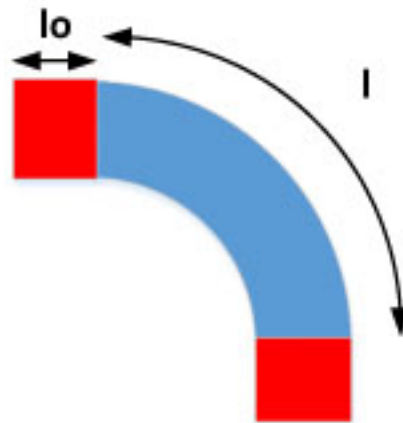


Figure 35 A diagram of each segment. The actuator with an interior pressure chamber is blue area, while the red areas are the gaps. Only blue area is pressurized and capable of active motion.

3.4.3 The Third Generation SRS

Simulations treat the last link and the tail as a single point mass. Therefore, the tail mass is different from the other four links. Table 6 displays the experimental parameter values, where m_T is the mass of the tail.

Table 6 Experimental Parameters of the Third Generation SRS

N	l	m	m_t	μ_t	u_n	β_i
5	0.037m	0.0525kg	0.2676kg	0.043	0.57	$\frac{2\pi I}{N-1}$

During experimental studies, the soft snake was operated at frequencies from 0.75–1Hz with the offset ranging from -0.2–0.2. Figure 36 shows the position of the soft snake at increments of 6 s when the frequency is 1Hz and the offset the is 0.2.

The input pressure was fixed throughout all of the experiments at a value that was too high for the actuators to withstand at steady state. To minimize the time each actuator was pressurized, we constrained the frequencies to remain above 0.75 Hz and the absolute value of the offset to be below 0.2. Figure 37 shows a series of SRS states over a 10 s time interval, comparing simulated results against the experimental results. At each state, the circle represents the snake’s head, and the curve is the rest of the snake trailing behind. In the experimental plot, some snake states have much larger curvatures than the others. This is a result of errors in the motion-capture data, as the curvature sensors do not provide global position information. In the simulation, the zero-offset path of the snake was directly along the vertical axis, with offset paths curving symmetrically to the right and to the left. The experimental snake exhibits a bias to the left, which can be corrected by giving a negative offset. This is likely the result of inconsistencies in the fabrication process, which create different bending properties on either side. In addition, due to curvature sensor requirements (circuit components are placed on one side of the plastic substrate), the constraint layer (the neutral axis) is slightly off center, biasing a

single direction of steering. It should be noted that, given the minimum allowable offset of -0.2 in these experiments, the current snake can only turn right over exceedingly large radii. Using larger negative offset values may enable steering in both directions for smaller pressure input values. The fabrication process may be revised to position the constraint layer at a different location that yields the same amount of bending in both directions.

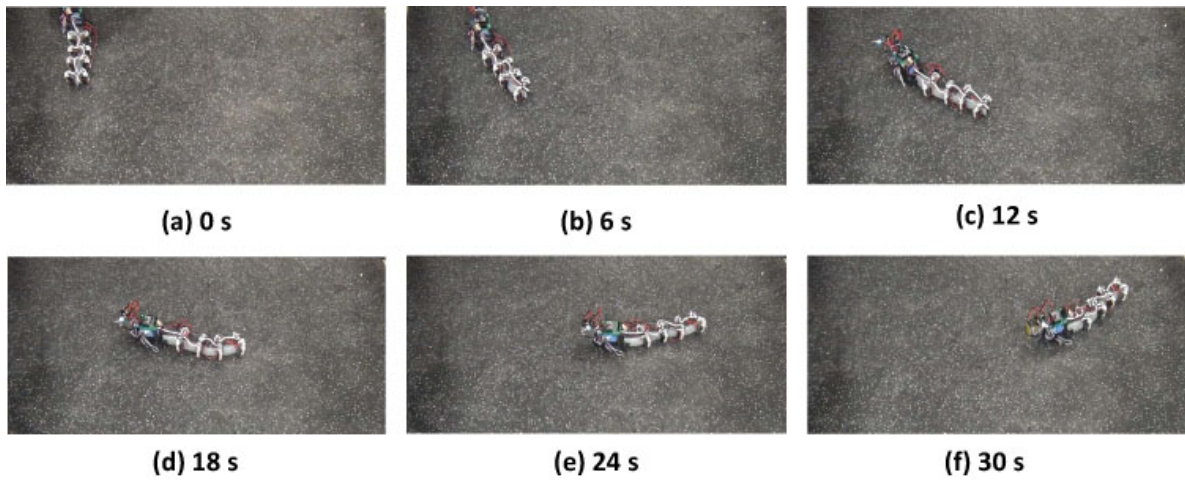


Figure 36 A series of still images, each 6 s apart, taken to show the snake in operation. The frequency is 1 Hz, and the offset is 0.2.

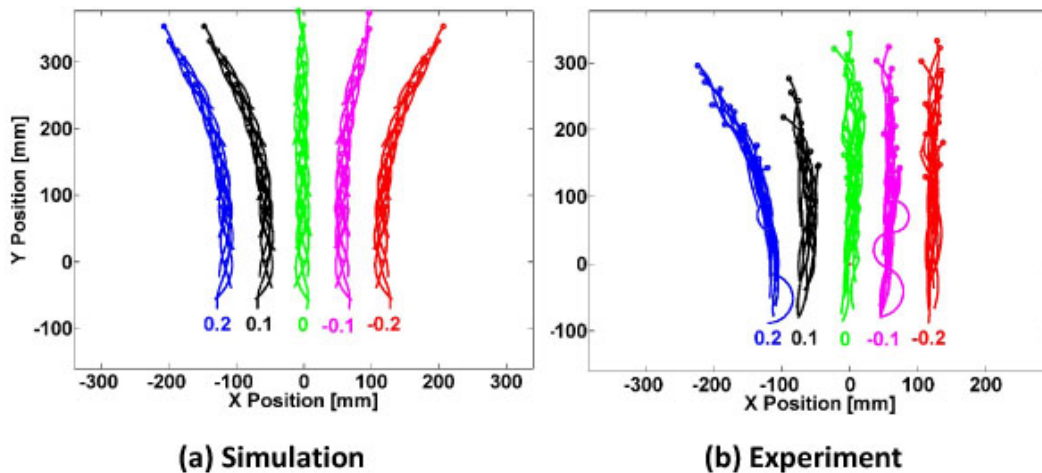


Figure 37 SRS shape and trajectory when the frequency is 0.9Hz and the offset is 0.2 (blue), 0.1 (black), 0 (green), -0.1 (pink), and -0.2 (red) in the simulation (a) and experiment (b) in 10s.

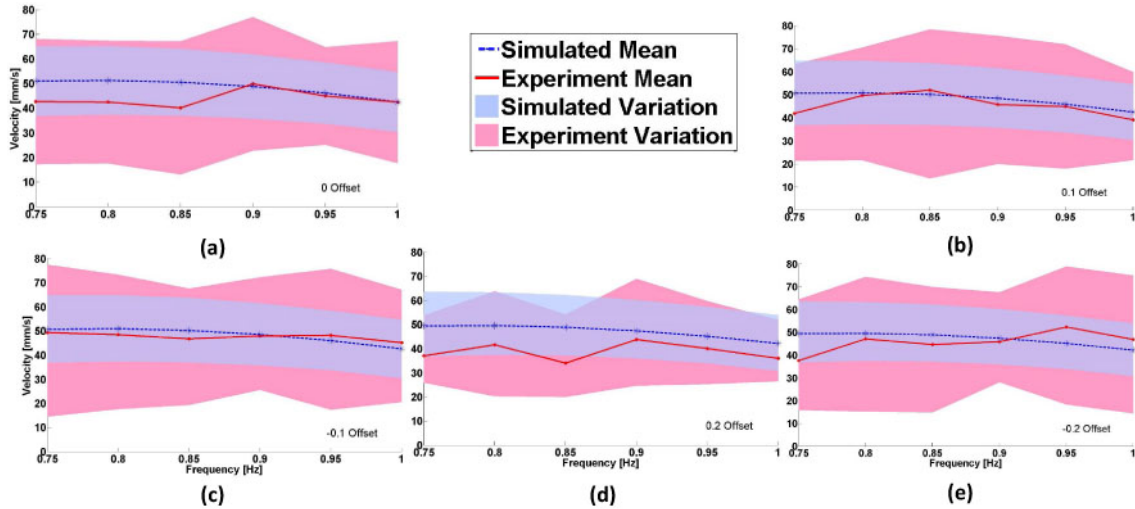


Figure 38 The center of mass (CoM) linear velocity and its standard deviation with respect to undulation frequency from 0.75–1Hz for offset values of 0 (a), 0.1 (b)–0, 1 (c), 0.2 (d), and –0.2 (e). The red solid line and area represent experimental results, and the blue dashed line and area represent simulation results.

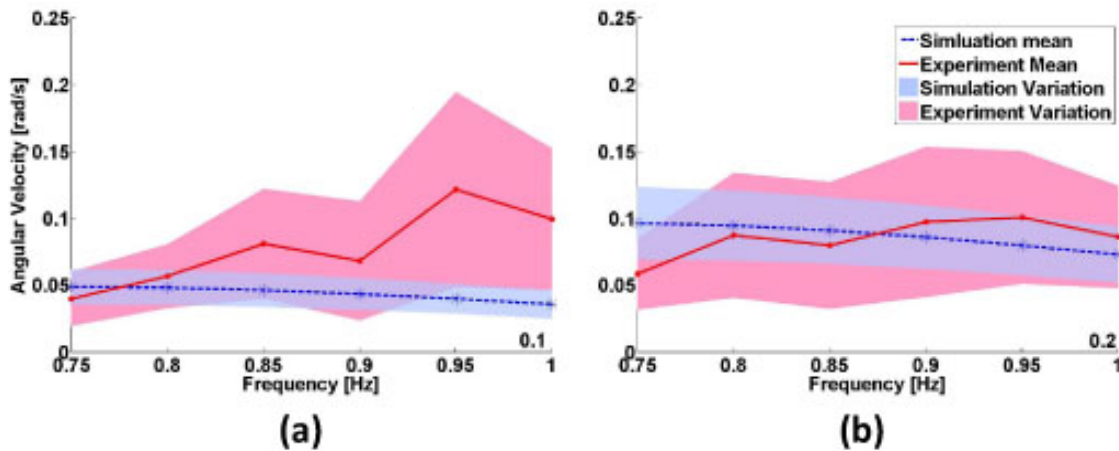


Figure 39 The CoM angular velocity and its standard deviation with respect to undulation frequency from 0.75–1Hz for offset values of 0.1 (a) and 0.2 (b). The red solid line and area represent experimental results, and the blue dashed line and area represent simulation results.

Figure 38 shows a comparison of the linear velocities of the center of mass (CoM) of the SRS between simulation and experimental results. From the plots, it can be seen that the general behavior of the experimental snake is captured by the model. The differences between the model predictions and experimental results are likely the result of measurement errors, fabrication inconsistencies, and varying friction coefficients on different areas of surface. Figure 39 shows the CoM angular velocities for the simulated

model predictions and experimental results under offset values of 0.1 and 0.2. The CoM angular velocities were too small for offsets of 0, -0.1, -0.2 to give meaningful data. As with the linear velocity, the model also predicts physical snake behavior with relative accuracy, especially considering the inconsistencies in the SRS prototype. However, the simulation results display a slight trend of reducing angular velocities with increasing frequency. This makes sense, as an increase in frequency reduces the amplitude of the curvature waveform, which translates as slightly reduced linear velocity. A corresponding effect on the angular velocity is visible, which is calculated as the linear velocity of the CoM around a radius of curvature. Angular velocity measurements are subject to a lot of experimental variation, since linear velocities and radius-of-curvature values both include uncertainty, leading to larger variations in angular velocity measurements. However, the numerical predictions stay within these experimental variations, where trends are difficult to capture.

In order to verify the performance of the integrated curvature sensors, we first performed a line fit to the bending angle with respect to the sensor voltage data on preliminary characterization experiments. We then used this relation to compare curvatures recorded by the curvature sensors and external motion-capture system, which can be seen in Figure 40. The curvature sensors measure the changing actuator angles with high sensitivity and low noise. No difference in quality is observed between the embedded and external measurement systems. Even though valves operate in binary open and close modes, this figure also displays the dynamic response of the actuators smoothing the square waveform to approximate a sinusoidal signal, which we consider

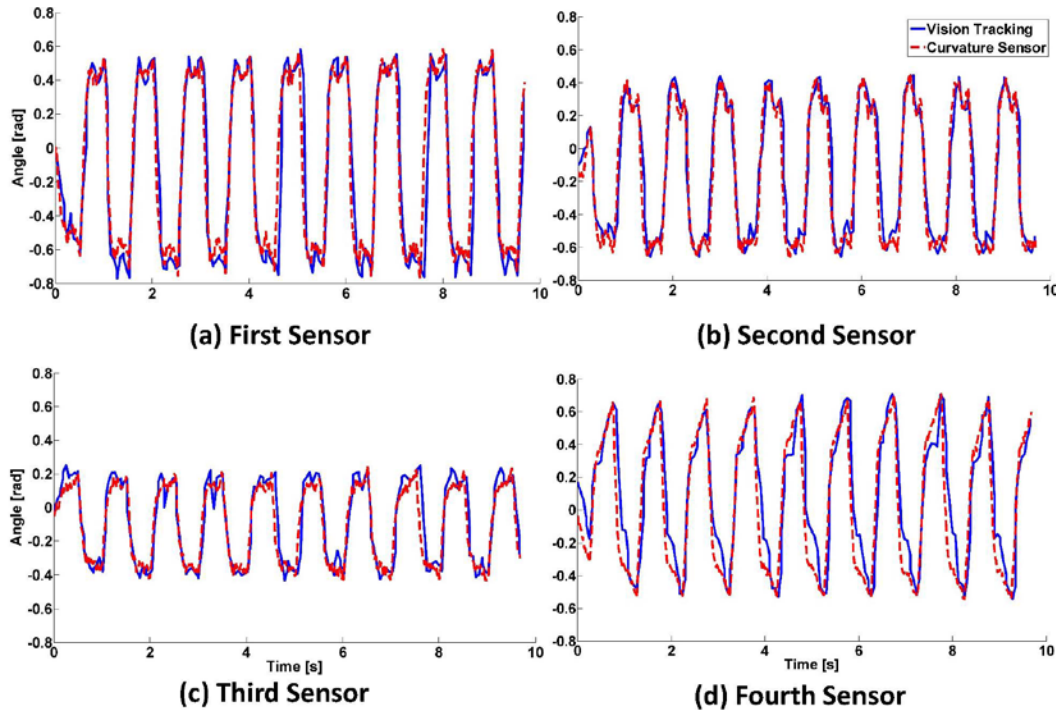


Figure 40 Performance verification of the four embedded curvature sensors using external motion-capture data as ground truth, for $\omega = 2$ Hz and $\phi = 0$. (a)–(d) represent each segment from head to tail.

as a form of physical intelligence, reducing low-level control requirements. It can be seen that the first actuator (head) has the largest amplitude, and the third segment has the smallest amplitude. This is partially the result of differing inertias of the snake on either side of each actuator. For example, the first actuator has nothing in front of it to move, so it is free to curve with less constraint. This does not explain why the fourth actuator has a larger amplitude than the third, as the tail of the snake is where most of the mass is located and should be the most difficult to move. This behavior may be the result of fabrication and assembly errors, both of the soft core itself, and of the valve mounts. There may have been differences in the distances between the valve mounts, with the two mounts surrounding the third actuator being closer together, resulting in reduced curvature from that actuator and more from the surrounding ones. Finally, we observed

that the front wheels of the tail assembly lift off the ground during locomotion, greatly reducing the lateral forces on the end of the fourth segment, allowing for greater bending deformation.

3.5 Discussion and Conclusion

In this section, we developed a complete dynamic model of the SRS to take into account the full balance of forces and torques, allowing it to predict angular velocities. We demonstrated the accuracy of this model by comparing its results to the actual behavior of the first three generation SRS, with the discrepancies being a result of fabrication inconsistencies.

Using the proposed refinement of the soft snake dynamic model, we will be able to use this proposed soft snake robot for more precise control and motion planning. This could include having the snake traverse a maze, where it would need to adjust its undulation parameters in order to move through challenging passages.

Chapter 4

4. Control of Soft Bidirectional Bending Modules

Control in the context of soft robotics has very little precedence, emphasizing the complexity in devising motion control algorithms for these inherently slow-response systems. Work was controlling a unidirectional soft pneumatic bending segment using fiber Bragg grating for sensing and valve pulse width modulation (PWM) for actuation, but with a slow response time. In our previous work, we focused on an iterative sliding mode controller (Iterative SMC) augmented by a feedforward term on a simple 1-DoF revolute joint operated antagonistically by two linear soft pneumatic actuators we call reverse pneumatic artificial muscles (rPAMs). The Iterative SMC utilized PWM of miniature solenoid valves as an approximation of analog pressure control. We recently adapted this control approach to our soft bidirectional bending actuator to compare our

custom magnetic curvature sensor with an off-the-shelf flex sensor, whose resistive sensing modality suffers from significant dynamic artefacts. Our results indicate that, despite its utility in feedback motion control of soft robots, this controller requires solenoid valves to be continuously switched on and off reducing their operational lifetime, and forces the feedback control loop to run at a relatively low frequency due to PWM discretization.

This section, we also seek to increase the bandwidth of the feedback control loop by using a more complicated valving scheme alongside a sliding mode controller directly regulating valve states (Direct SMC). This method allows the system to hold pressure in the actuator, reducing the chattering in the valves, and increasing their lifespan.

The outcome of this chapter was published at [96].

4.1 Iterative and Direct SMC (Sliding Mode Control) Algorithm

In our previous work, we employed an iterative sliding mode controller (Iterative SMC) to control the pressure in each actuator. This was done using pulse width modulation; opening and closing the valves of each actuator to alternately inflate and deflate each actuator at a certain duty cycle as control input. The valves each have a response time of 3 ms, are about 7 mm x 12 mm x 30 mm, and each cost around \$30. As Chapter 2 mention, the dynamic behavior of the soft bending actuator can be approximated as a lumped second order dynamic equation as:

$$\ddot{\theta} = C_1 e^{-t/\tau_1} + C_2 e^{-t/\tau_2} + C_0 \quad (18)$$

Where C_1, C_2 are constant coefficients. τ_1, τ_2 are time constants, and C_0 is the steady-state static angle, with a one-to-one relation to the PWM duty cycle, indicating the angle the actuator will converge after the dynamic terms dissipate.

The dynamic response of the actuator can then be described as the second order system:

$$\hat{a}\ddot{\theta} + \hat{b}\dot{\theta} + \theta = \hat{c}u(t) \quad (19)$$

where θ is the bending angle with respect to time, $u(t)$ is the input Duty Cycle of the PWM signal and $\hat{a} \in (a_o - \Delta a, a_o + \Delta a)$, $\hat{b} \in (b_o - \Delta b, b_o + \Delta b)$ and $\hat{c} \in (c_o -$

$\Delta c, c_o + \Delta c$) are bounded uncertainty parameters. a_o, b_o and c_o and $\Delta a, \Delta b$ and Δc are the mean and 95% confidence interval values of a, b, c .

Eq (19) can be rewritten in state-space form as:

$$\dot{\mathbf{x}} = \mathbf{A}\mathbf{x} + \mathbf{B}\mu(t) \quad (20)$$

Where $\mathbf{x} = [\theta \quad \dot{\theta}]^T, \mathbf{A} = \begin{bmatrix} 0 & 1 \\ -\frac{\hat{b}}{\hat{a}} & \frac{1}{\hat{a}} \end{bmatrix}, \mathbf{B} = \begin{bmatrix} 0 \\ \frac{\hat{c}}{\hat{a}} \end{bmatrix}^T$. Thus, an iterative sliding mode controller can be designed for motion control based on the given dynamic model and bounded uncertainty parameters. For a given reference x^{ref} , the position error is given as:

$$\mathbf{e}_x = \mathbf{G}_x(x^{ref} - \mathbf{x}) \quad (21)$$

where $\mathbf{G}_x = [C \quad 0]$. We define a non-negative Lyapunov function candidate and its derivative as follows:

$$V_x = \frac{e_x^2}{2} \geq 0 \quad (22)$$

$$\dot{V}_x = e_x \dot{e}_x \quad (23)$$

and select a desired dynamic error manifold as:

$$\dot{e}_x + D_x e_x = 0 \quad (24)$$

Where D_x is a positive constant. Plugging (24) into (23), we obtain a non-positive Lyapunov function derivative as:

$$\dot{V}_x = -D_x e_x^2 \leq 0 \quad (25)$$

Which will ensure stability. Combining (20) and (21)

$$\begin{aligned} \dot{e}_x &= G_x(x^{ref} - \dot{x}) \\ &= G_x(x^{ref} - Ax - B\mu(t)) \\ &= G_x B(\mu_{eq}(t) - \mu(t)) \end{aligned} \quad (26)$$

$$G_x B(\mu_{eq}(t) - \mu(t)) D_x e_x = 0 \quad (27)$$

Where $\mu_{eq}(t)$ is the continuous equivalent control input, which is difficult to calculate. Rearranging (26) reveals:

$$\mu_{eq}(t) = \mu(t) + (G_x B)^{-1} \dot{e}_x \quad (28)$$

Approximating $\mu_{eq}(t)$ with $\mu_{eq}(t - \Delta t)$, where Δt is the time step yields the iterative sliding model control law:

$$\mu(t) = \mu(t - \Delta t) + (G_x B)^{-1}(\dot{e}_x + D_x e_x) \quad (29)$$

For simplicity, we define $K = (G_x B)^{-1}$ as a scalar positive tuning factor as:

$$\mu(t) = \mu(t - \Delta t) + (K \dot{e}_x + D_x e_x) \quad (30)$$

One problem of this control method is that it involves constantly inflating and deflating each pneumatic chamber, even when the desired angle is constant. This causes the bending actuator to continuously oscillate around its target and potentially reduces the lifetime of the miniature solenoid valves.

In order to improve upon this, we have adapted our pneumatic circuit to have separate valves on the inlet and outlet of each actuator. This makes it possible for a constant pressure to be held within the chambers, keeping them steady. We derive a direct sliding mode control (Direct SMC) algorithm with this valve setup, defining:

$$\sigma(t) = \dot{e}_x + D e_x \quad (31)$$

Where $\sigma(t)$ is the sliding-mode variable ($\sigma = 0$ describes the sliding manifold). We define three control states (modes). If $\sigma > \varepsilon$ (ε represents a dead-zone around the

target), the module is driven in one direction by venting one actuator and filling the other.

If $\sigma < -\varepsilon$, the module is driven in the opposite direction. However, if $-\varepsilon < \sigma < \varepsilon$, the controller holds the pressure in both actuators, keeping the module at a steady curvature.

4.2 Experimental Result

We first observed the static behavior of our bending module, snapshots of which can be seen in Figure 41. At 30 degree bending in both directions, we can see that the actuator bends smoothly and with constant curvature. The actuator is capable of bending up to 75 degrees in both directions, though this large bending angle seems to result in a less smooth curved shape. This is smaller than the 90 degree bounds we used to model the sensors, as the pressures required to reach 90 degrees can be dangerous to the actuator at prolonged periods. The unactuated side of the actuator is forced to compress so much at that angle that a crease forms, while the central constraint layer is observed to remain smooth. The actuator can reliably withstand pressures of 7 psi (48.3 kPa), which was the pressure used for all subsequent experiments.

We tested both controllers on the integrated soft bending actuator for step and sinusoidal bending angle references. For Iterative SMC controller, we used $K = 1.5 \text{ s/o}$ and $D = 0.0067 \text{ 1/s}$. For the direct SMC controller, we used $D = 0.5 \text{ 1/s}$ and $\varepsilon = 2 \text{ o/s}$. These coefficients were tuned by hand to maximize performance, focusing on minimizing rise time and then limiting subsequent oscillations. Figure 42 shows the response of the controller to a constant desired angle (step response). Unsurprisingly, the direct SMC method, a reduction of around 30%, as the valve configuration used in the direct SMC method allows the pressure required to maintain the desired angle to be held within the actuator. Thus, barring leakage, the direct SMC controller is capable of holding constant angles indefinitely without error. The fluctuation that can be seen in the direct SMC data

is the result of sensor noise. In addition, the direct SMC controller reaches the desired angle with

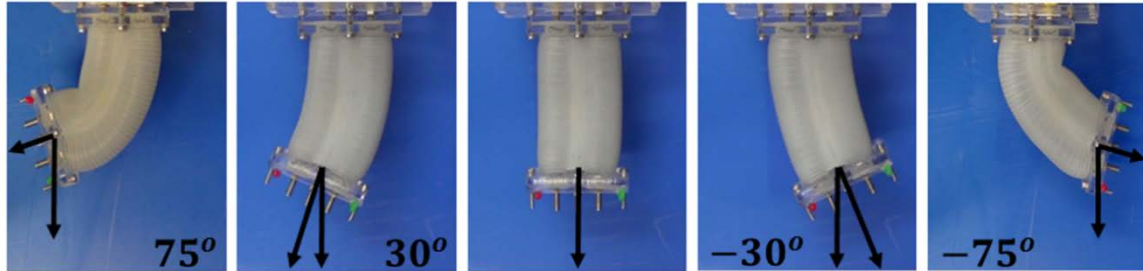


Figure 41 Static response of the fourth generation version bending soft robotic module in a range of 150o at ± 11 psi

significantly less overshoot than the iterative SMC controller. The direct SMC had almost none (less than its steady-state fluctuation), while the iterative SMC demonstrated a 40% overshoot and only settled down after 0.4 seconds (as opposed to 0.2 seconds for the direct SMC).

Figure 43 shows the two controllers following four periods of sine waves at an amplitude of 0.6 rad (34.3°) and frequencies ranging from 0.25 to 6 Hz. There is little difference between the performances of the two controllers at less than 1 Hz, because both controllers are faster than the reference signals. However, the direct SMC controller demonstrates superior performance at higher frequencies, with a 15% higher amplitude and a phase delay of 0.5 less at 6 Hz. It can be seen that the direct SMC controller trajectory is closer to the desired trajectory at higher amplitudes, with larger amplitudes and less phase delay than the iterative SMC. In addition, the direct SMC controller exhibits less vibration than the iterative SMC controller.

However, at the lowest frequency the direct SMC trajectory has larger fluctuations. This is because the direct SMC controller can only either hold position or apply full

pressure in either direction. Thus, when the desired position is outside the dead-zone but nearby, the SMC will cause the actuator to move rapidly, with limitations in the valve

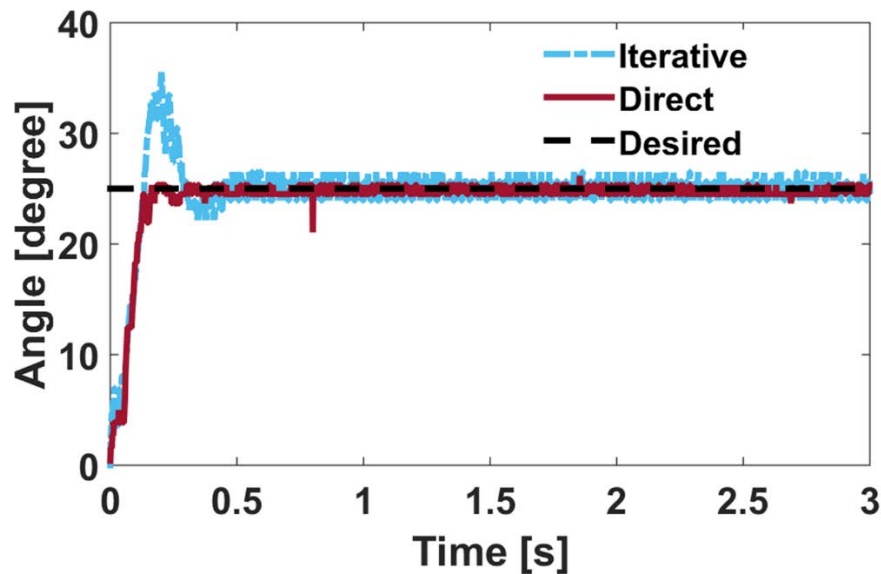


Figure 42 Step response of the two controllers. Red dashed line is the desired bending angle (25o) and the blue and black curves represent the iterative sliding mode controller and the direct sliding mode controller, respectively. The Direct SMC trajectory exhibit.

response time causing it to overshoot the desired position slightly, before undergoing damped oscillation around the desired position. During low frequency signal following, the desired trajectory keeps moving just outside the dead-zone, causing this behavior to occur over the entire trajectory. Under these circumstances, the iterative SMC will change the duty cycle slightly, causing the new average actuator position to increase slightly, resulting in a smoother transition for smaller disturbances.

In order to demonstrate the performance variation between the two controllers, Figure 44(a-b) shows the aggregated normalized amplitude and phase delay for each controller at each frequency. This data shows that the direct SMC controller has a much higher bandwidth than the iterative SMC method, exhibiting little increase in phase delay as frequency increased, to a maximum of 0.5 rad. The direct SMC method also has a higher

amplitude at higher frequencies, consistently around 10 percentage points higher, as the amplitude of the iterative SMC drops off steeply. In addition, the differences in standard deviation between the two controllers show that the direct SMC controller results in less vibration, as expected.

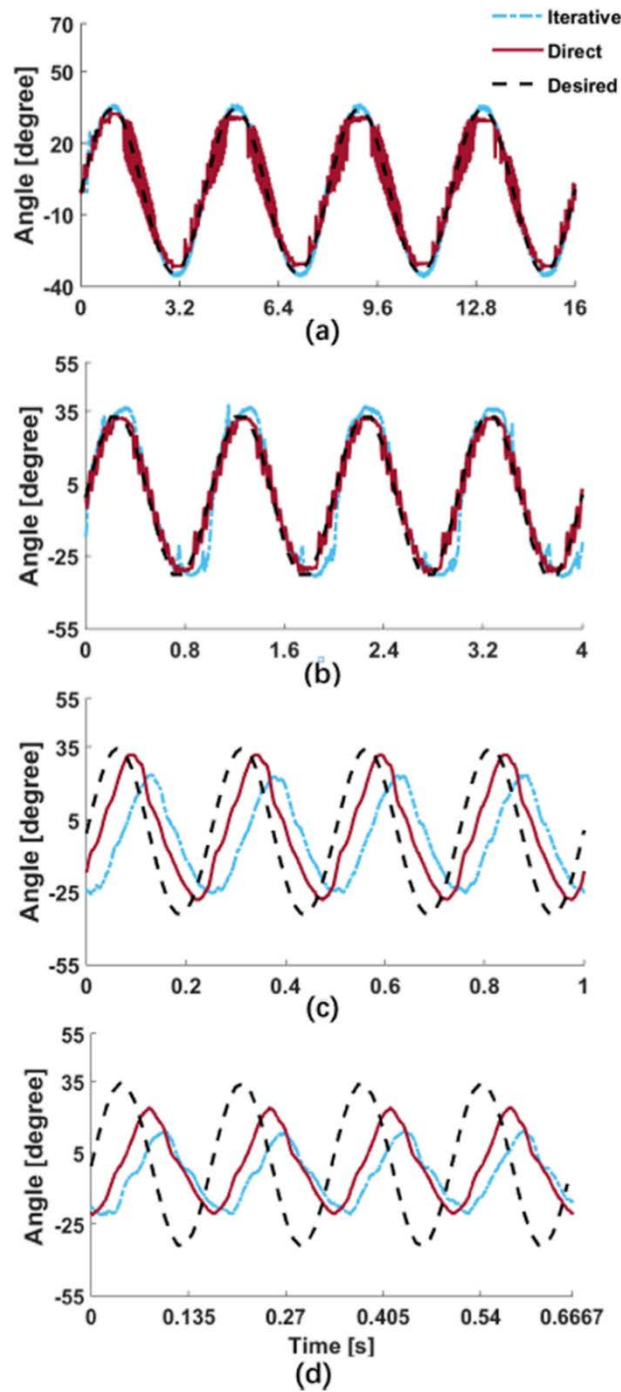


Figure 43 Dynamic response of both controllers following sinusoidal trajectories with frequencies of 0.25 Hz (a), 1 Hz (b), 4 Hz (c), and 6 Hz (d), with the same bending angle amplitude of 34.3°. The red dashed line is the desired trajectory and the blue and black.

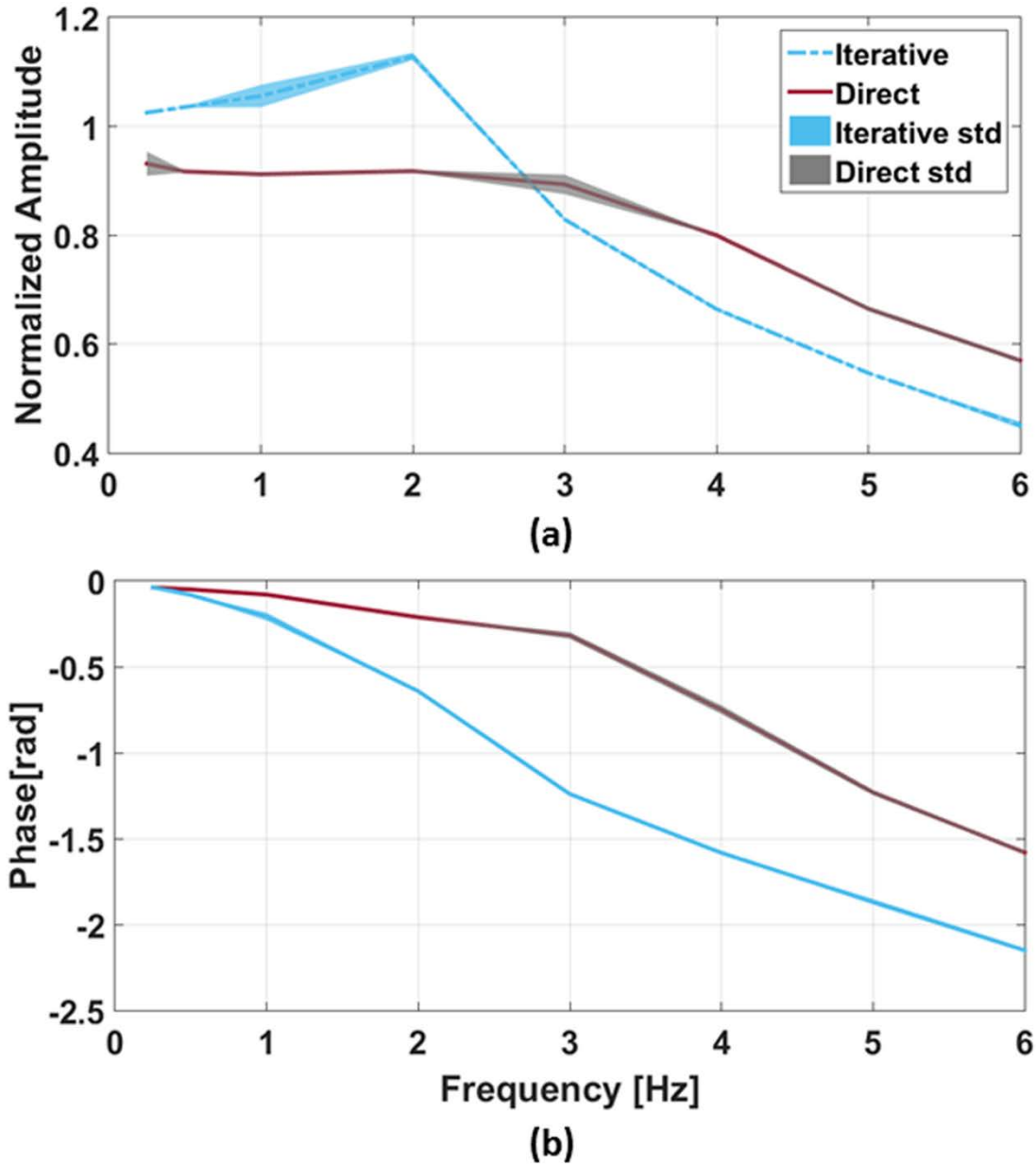


Figure 44 Closed loop frequency response of both controllers tracking sinusoidal signals over a range of frequencies. The normalized amplitude (a) and phase delay (b) data indicate that the direct sliding mode controller offers superior tracking performance with improved phase delay and more uniform amplitude values.

We have had concerns about the lifetime of valves under this type of rapid actuation. In particular, we have observed that the continuous actuation of the iterative SMC controller has had a deleterious effect on the valves being used. To investigate this, we recorded the valve states of the controllers as they operated, allowing us to keep

track of how many times each valve was cycled. First we did this test for sine wave following at 6 Hz (with amplitude = 0.6 rad, as before), the results of which can be seen in Figure 45(a-c). At 6 Hz the system cannot respond quickly enough to follow the sine waves accurately, and thus alternate between full actuation in either direction. We can see from plots (b-c) that the iterative SMC actuates each valve more often for an inferior performance. Over 10 seconds of constant 6 Hz sine wave following, the direct SMC actuator drives each of its valves a total of 67 times compared to the iterative SMC controller's 349 times. Thus, under this operation, valves of a system using the direct SMC controller are likely to last 5 times as long as those using the iterative SMC controller. We also performed the same test when following a 2 Hz square wave with an amplitude of 0.6 Rad (34.3o), which can be seen in Figure 46(a-c). This is a slower frequency than the previous test, which allows the system to reach the desired angle and hold. We can see from Figure 10(b-c) that once the desired angle has been reached, the direct SMC controller stops actuating each valve, while the iterative SMC controller must continue to repeatedly switch between the two states to hold position. Over 10 seconds of tracking a 2 Hz square wave, the direct SMC controller actuates each valve 26 times, while the iterative SMC controller actuates each valve 213 times, an increase of over 8 times the number of switching commands per valve. This improvement will increase for trajectories that involve maintaining a constant angle for extended periods of time, which the proposed direct SMC controller can do without any continuous valve actions.

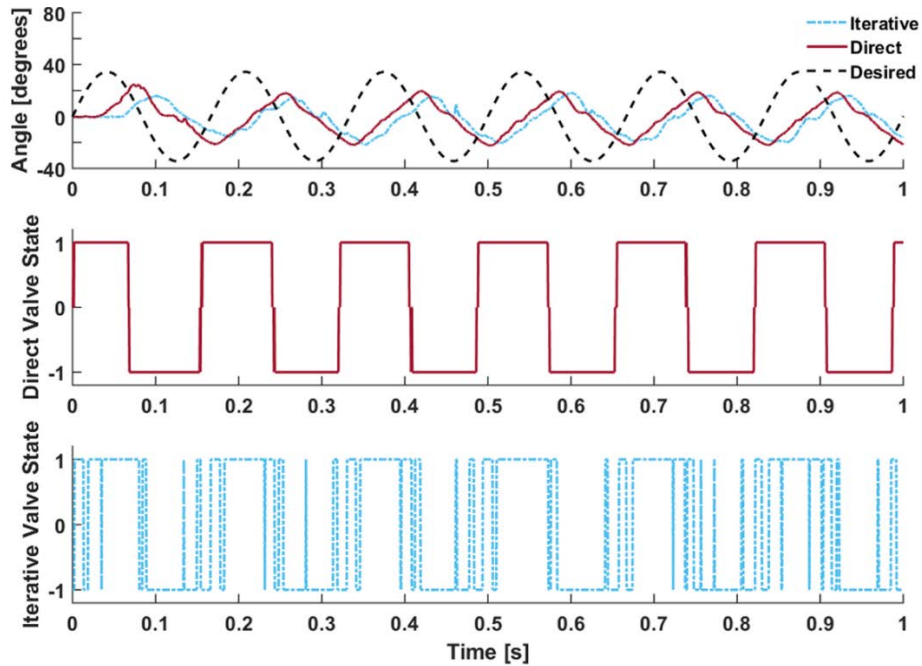


Figure 45 (a) Iterative and direct SMC system trajectories for 6 Hz sine wave following. The corresponding valve states for the direct (b) and the iterative SMC controller (c), where 1 represents bending actuation in the positive direction, 0 represents holding (applies only to the direct SMC controller) and -1 represents bending actuation in the negative direction.

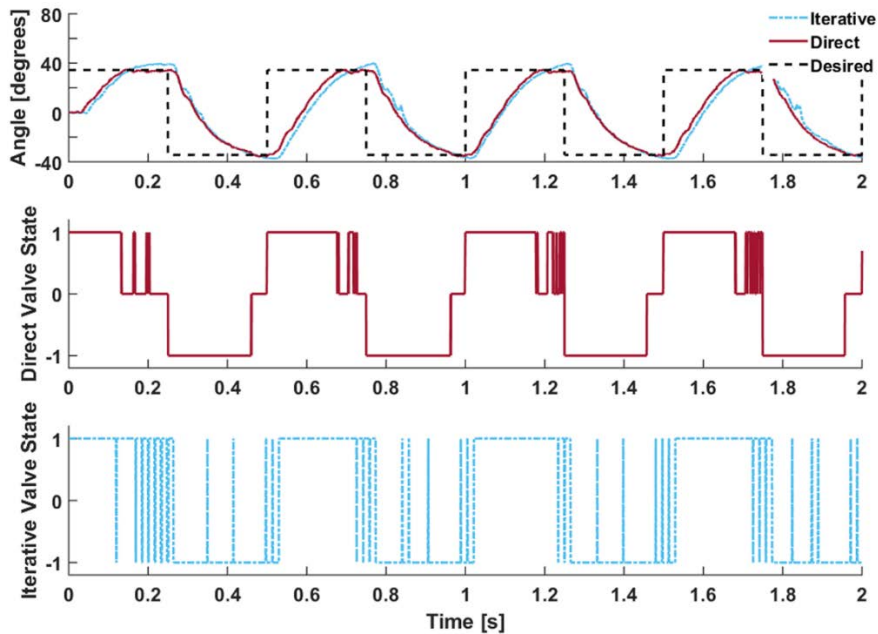


Figure 46 (a) Iterative and direct SMC system trajectories for 2 Hz square wave following. The corresponding valve states for the direct (b) and the iterative SMC controller (c), where 1 represents bending actuation in the positive direction, 0 represents holding (applies only to the direct SMC controller) and -1 represents bending actuation in the negative direction.

4.3 Discussion and Conclusion

In this section, we demonstrated the superiority of this controller over our previously developed iterative sliding mode controller in following static and dynamic trajectories of frequencies ranging from 0.25 to 6 Hz. In addition, we demonstrated a reduction in valve actuations of the direct SMC controller compared to the iterative SMC controller, indicating the former is conducive to longer lifetimes for solenoid valves.

One potential problem with the valving used for the direct SMC approach is it requires two on/off valves for each pressure chamber, and thus, requires double the amount of control signals. This was not a problem for a single bidirectional bending segment with two chambers, but would be more of a difficulty for larger systems with more degrees of freedom. In addition, while the valves are relatively small, on a self-contained system the doubling of the required valves could take up a prohibitive amount of space, perhaps outweighing the improvements it provides.

The ability of the direct SMC controller to follow static trajectories relies on a well-sealed pneumatic system. Any leaks will cause it to drift away from a desired static angle. Once it leaves the dead-zone ε , the control system will respond and experience some oscillation before becoming steady again. This behavior results in much larger oscillations than the iterative SMC around a steady state. As our soft robotic snake locomotion requires dynamic trajectories from each module, this will likely not be a problem for that application. On the other hand, for these modules to be used in a soft manipulator, the ability to remain steady will likely be useful, requiring the chambers to remain well-sealed.

The next step is to adapt this soft actuation module for use in our soft robotic snake. These will be easy to assemble in series to form the body of the snake. The modular nature will allow the snake to be easily repaired and expanded, letting us investigate grasping and redundant locomotion towards a soft mobile manipulator in future work.

Chapter 5

5. Iterative Learning Control and Object avoidance Motion Planning

The higher level behavior of soft robots is a current challenge for researchers. The ideal robotic control behavior is “sense, plan, act,” with the robot observing its environment, deciding what to do, and then doing it. However, compared with traditional rigid robot, the uncertainty soft robotics impedes its realistic application, because the infinite degrees of freedom, the nonlinear materials, and the typical time delay of the soft robotic system actuation increase the computation time for running these algorithms. On the other hand, soft robotics has the advantage of a smooth and continuous biological shape and safe human interaction which also come from these features. In order to reach a general solution for the soft robotics’ task, we proposed a guideline for how to pick the minimum observations which can encapsulate a soft robot’s kinematic and dynamic

features as well as the minimum control inputs which is not compensated the dynamic benefit of the soft robotics but guarantee the accuracy.

In this section, we will investigate two system-level tasks based on the fourth generation WPI SRS platform. First, WPI SRS is able to go in a straight line and turn with a consistent curve by correcting own motion. Because the dynamic and static behavior of each module is different, the WPI SRS does not naturally travel in a straight line or in a consistent curve without feedback control. We utilize the local curvature sensor information and an iterative learning control algorithm to address this problem. In this method, we only control a single parameter to guarantee the snake's motion as desired. Second, we develop a high-level motion planning method to allow the WPI SRS to avoid obstacles and reach the target on 2D space. First, we generate a path based on the traditional A* algorithm and the bounding box for the SRS determined by the kinematic and dynamic information. Then WPI SRS can follow this path using the iterative learning control algorithm.

The outcome of this chapter is under review at [98].

5.1 Iterative Learning Control

Iterative Learning Control (ILC) is a method for control of systems that repeat the same actions over and over again [99]. The serpentine locomotion of the WPI SRS is an example of this, with motion stemming from the repetition of a single gait cycle. In Figure 47, we show the data from the embedded curvature sensor and external motion tracking for each module of the WPI SRS during open-loop operation. Under ideal circumstances, the WPI SRS should go straight line under these conditions. However, from the plot we can see that each actuator behaves differently, with different output amplitudes. These different trajectories, resulting from differences in fabrication, flow rate, and wheel pressure, result in non-straight trajectories for the WPI SRS as a whole.

In this situation, ILC is an ideal tool help WPI SRS follow a straight line. The formulation of the ILC is as follows:

$$u_n = u_{n-1} + ke_{n-1} \quad (32)$$

where u_n is a constant control input at period n , e_{n-1} is the error term for the previous $(n - 1)$ period, and k is the control gain. For the locomotion method of the WPI SRS is a traveling sine wave, where the control input u_n represents the PWM duty cycle of the solenoid valves connecting each actuator chamber to the common pressure source. Our WPI SRS has four modules, therefore, there are eight control inputs. e_{n-1} is the error between the bending angle of each module and the desired bending angle.

First, we use the basic ILC method of self-learning on the WPI SRS. Figure 48 shows bending angle of the four modules during the control process. We run the WPI SRS

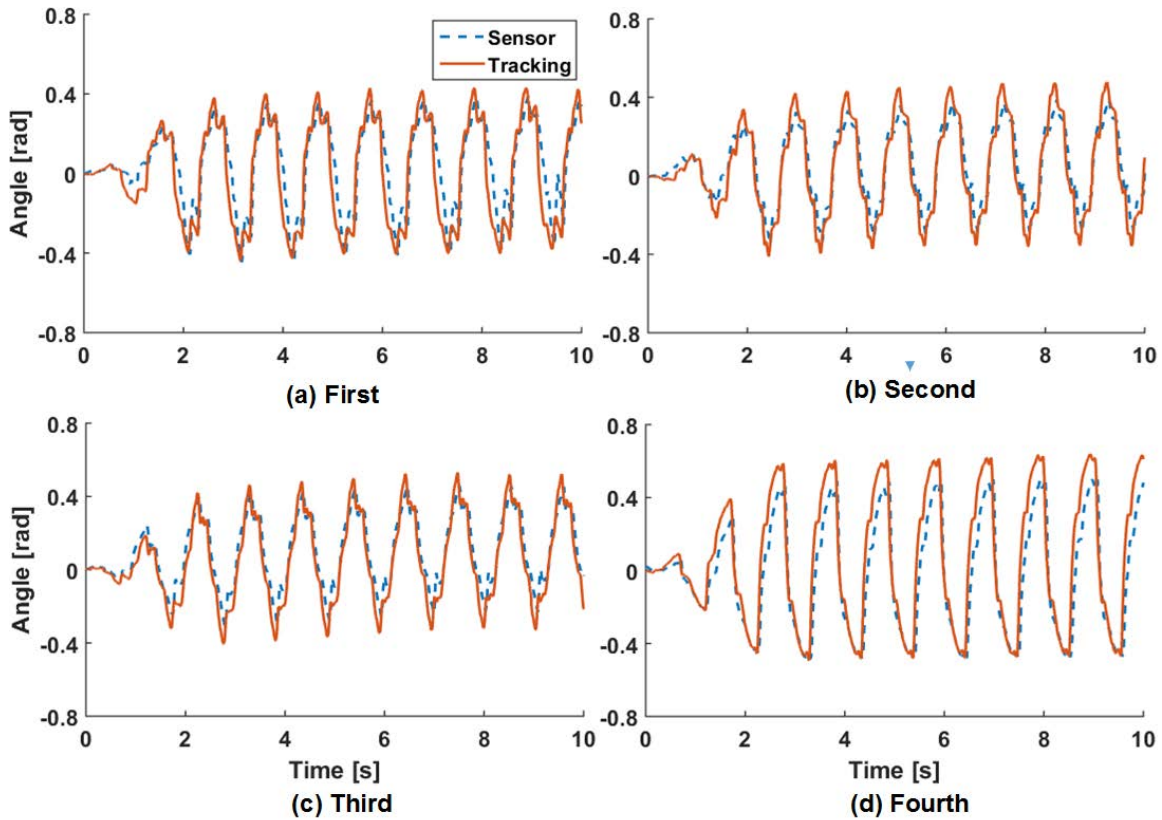


Figure 47 The sensor verification of four generation WPI SRS.

frequency is 1 Hz, phase offset is 0 and full Duty Cycle PWM signal under 19 psi pressure. We use open loop control for the first two periods (to the left of the first vertical pink line). The amplitude is increasing during these two cycles as the WPI SRS gets up to the steady-state flow rate. The controller start by recording the bending angles at the beginning of the third period and calculating the positive and negative amplitude of the four modules in these period. Then we choose the smallest amplitude measured to be the desired, ensuring that the common amplitude can be reached by all actuators.

In following period, the controller recollects the bending angle of all modules at the beginning of the period, then finds the error with respect to the desired amplitude. It passes these errors into the ILC controller to correct the duty cycle of each solenoid valve. At the software level, we can achieve this process on our microcontrollers using time

interrupts, which, as only one interruption is required per cycle, results in minimal code disruption. From Figure 48, we can see that all bending angles are close to the desired angle after ILC takes over (to the right of the last vertical pink line). In this controller, the control gain $k=0.3$.

In first 6 periods after the ILC starts (Between 9 and 15 second), many of the actuators still overstep the desired angle. This is because the control duty cycle to the valves is still saturated, resulting in not change of behavior. After the 5th period, the control input is enough that the valves are no longer saturated, and the actuators behave as desired.

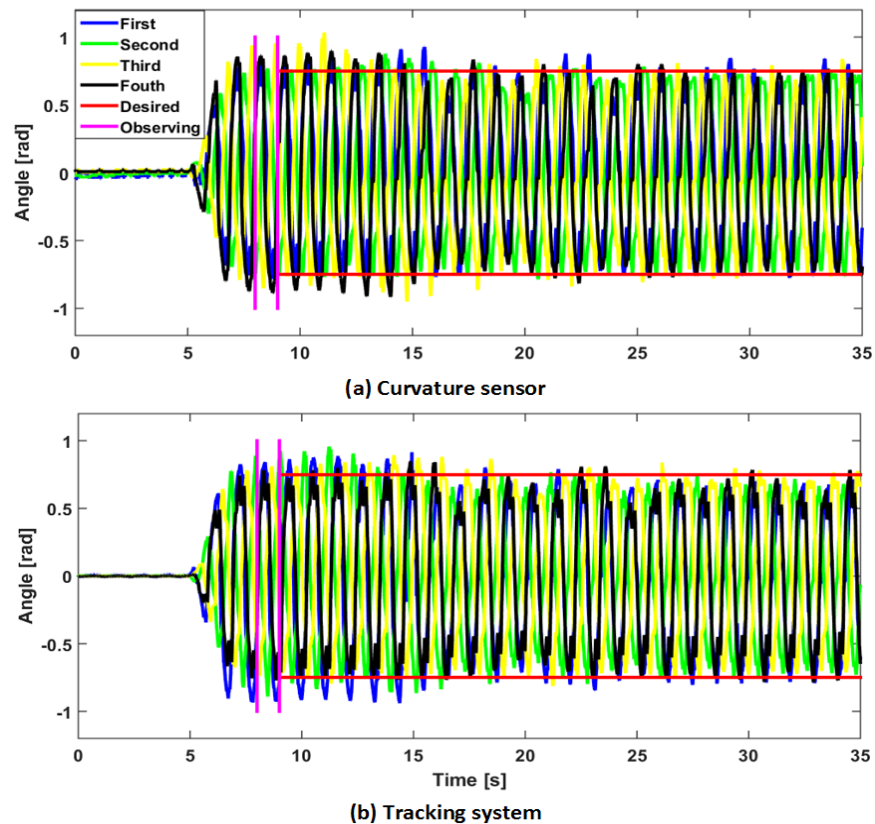


Figure 48 Each module bending angle of the WPI SRS go straight line test control by ILC. (a) is the embedded curvature sensor data (b) is the tracking data. The blue, green, yellow and black curvature respect each actuator bending angle. The pink region is WPI is starting self-learning procures, the controller record all angles data during this period and pick up the smallest aptitude be the desired angle. The red curvature shows the desired boundary.

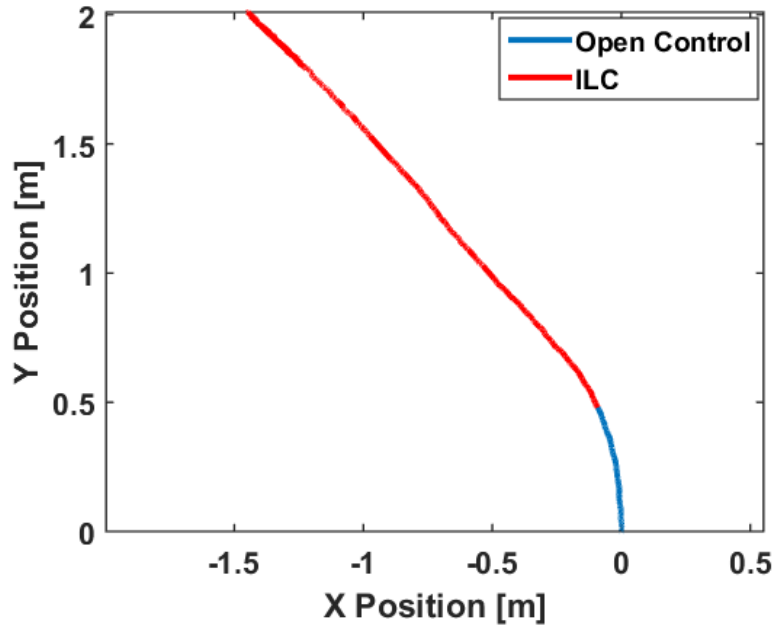


Figure 49 Center of Mass (CoM) of the WPI SRS during the ILC at straight line task

Figure 49 shows the trajectory of the center of mass (CoM) of the WPI SRS. From the plot, we can see that the use of the ILC allows the WPI SRS to travel in a straight line. Similarly, the WPI SRS can also use ILC to maintain a constant curvature trajectory. The only difference between this and the straight-line case is that here we choose the positive desired angle and negative desired angle independently. Figure 50 shows the data of each module from sensor and tracking system. The red line shows the positive desired angle and the cyan line shows the negative desired angle. All amplitudes of the bending modules are close to the desired boundary after the ILC comes into the effect. Figure 51 shows the CoM trajectory of the snake. From the plot, the WPI SRS is going a constant curvature curve after the control.

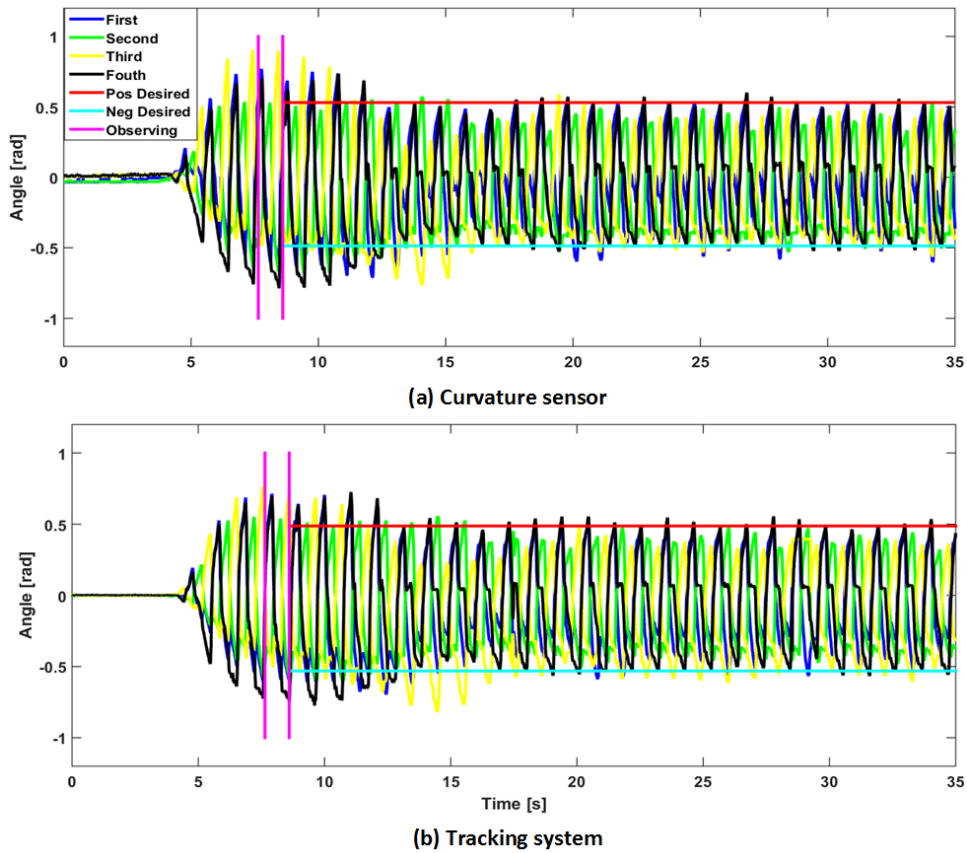


Figure 50 Each module bending angle of the WPI SRS go curve test control by ILC. (a) is the embedded curvature sensor data (b) is the tracking data. The blue, green, yellow and black curvature respect each actuator bending angle. The pink region is WPI is starting self-learning procures, the controller record all angles data during this period and pick up the smallest aptitude be the desired angle. The red curvature shows the desired boundary.

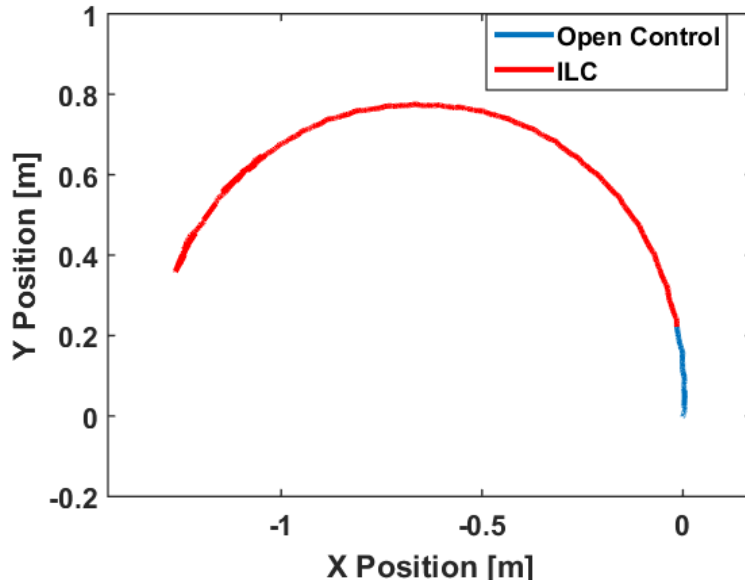


Figure 51 Center of Mass (CoM) of the WPI SRS during the ILC at curve task.

5.2 Motion planning and Trajectory following

5.2.1 Motion Planning

Mobile robot motion planning algorithms have been well established over the last couple decades [99-103]. The discrete space A* algorithm is one of the most common tools for mobile robot motion planning in 2D environments because such robots can be treated as a point in the environment. However, discrete space is not realistic for the WPI SRS, because of its minimum turning radius, especially for the limited space application. For snake robot motion planning, the Peterson group linearized the snake module rotation motion into two linear motion and ran an existing motion planning algorithm. However, a similar linearization method will not work for the WPI SRS because of the dynamic nature of the SRS and its continuously deforming structure. In this paper we use a bounding box, which is a simple, virtual structure that represents space that the WPI SRS takes up, taking into account both its kinematic and dynamic state. An example of a bounding box is shown on Figure 52. The brown point is the CoM of the WPI SRS in its current configuration.

To calculate the bounding box, we first assume that the WPI SRS CoM trajectory (the dashed line) is a constant curvature curve. To form the sides of the bounding box, we shift the CoM trajectory in two opposite directions, increasing or decreasing the curvature but keeping the center of curvature the same. These edges are moved outwards until they no longer overlap the edges of the snake. The other two ends of the bounding box are set

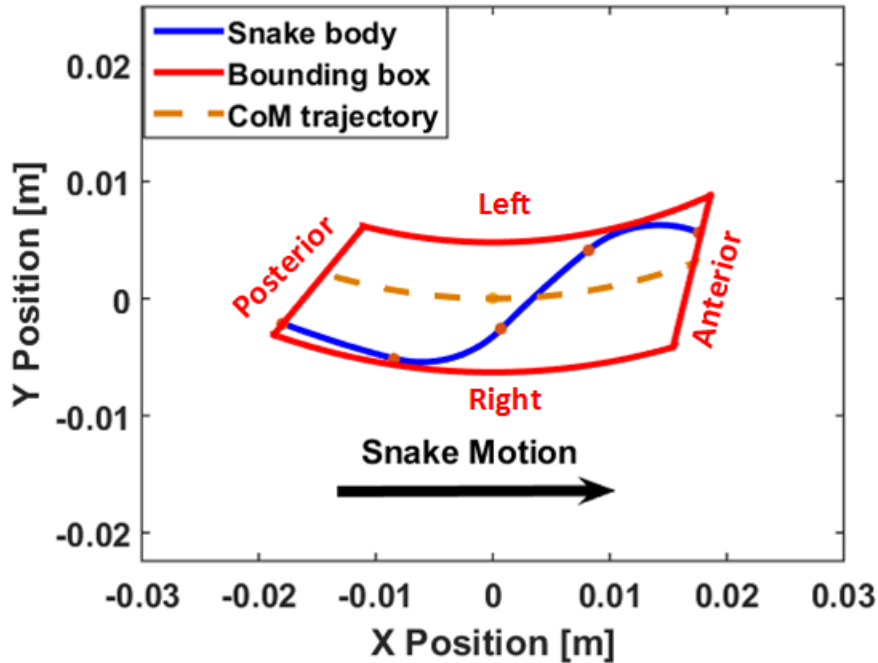


Figure 52 Bounding box definition

to be perpendicular to the WPI SRS' head and tail angles, intersecting with the first two edges. The red line in Figure 52 shows the bounding box. When the snake body's shape changes, the bounding box also changes. The general rule is that the width of the bounding box is fixed for a given input pressure and gait frequency, while the distance between the left and right boundaries changes as the turning offset changes. In order to put the bounding box concept into the motion planning algorithm, here are some assumptions for simplify the problem:

- The workspace of the snake is 2D flat surface.
- The workspace is a continuous space.
- The WPI SRS is a nonholonomic system with its turning angle bounded by $(-\alpha_{max}, \alpha_{max})$.
- The linear velocity of WPI SRS is constant.

- All the environmental obstacles can be represented as circles.
- The algorithm uses a constant sample time.
- The CoM trajectory of WPI SRS is constant curvature curve during the sample time.

This motion planning algorithm operates in continuous space because the shape of the WPI SRS cannot be ignored with respect to the environment. Since WPI SRS is a nonholonomic system, it has a minimum turning radius. As the experimental results showed in [65], the CoM trajectory of the WPI SRS is bounded and the linear velocity can be treated the constant at the different turning offsets.

Table 7 shows the parameters we used in the motion planning algorithm. The snake motion planning algorithm based on the Bidirectional A* algorithm. We assume that the max turning angle of WPI SRS is α_{max} . We divide this range $(\alpha_{max}, -\alpha_{max})$ into N different curvatures. These N curvatures will be each held for a fixed timestep, resulting in N discrete trajectories, or motion primitives, available for the planner at each step. Thus, each parent node will have N child nodes. Because we know the turning angle $\alpha \in (\alpha_{max}, -\alpha_{max})$, the initial CoM angle θ , the linear velocity v and the sample time Δt are constant of the node n , we could determine the bounding box position between the node n and $n + 1$. $P_x(n), P_y(n), \theta(n)$ are the CoM position and orientation of the node n , so the CoM position and orientation of the node $n + 1$ be calculated by:

Table 7 Parameters of the motion planning algorithm

Turning angle	Radius	CoM position	CoM angle	Linear velocity	Sample time
α	r	P_x, P_y	θ	v	Δt

$$P_x(n+1) = r \left(\sin(\theta(n)) - \sin(\theta(n+1)) \right) + P_x(n) \quad (33)$$

$$P_y(n+1) = r \left(\cos(\theta(n+1)) - \cos(\theta(n)) \right) + P_y(n)$$

$$\theta(n+1) = \theta(n) + \alpha$$

$$r = v\Delta t/\alpha$$

Figure 53 shows one simple example of the motion planning algorithm. $N = 5$, $v = \frac{1m}{s}$, $\Delta t = 0.5s$. Start position and rotation: $(0,0, -\frac{\pi}{4})$ and the target position and rotation: $(2,1, -\frac{\pi}{4})$. As in the normal A* algorithm, there two scores defined as:

- g score: If the snake go more straight curvature, the g score will be lower. Assume N is odd number and all paths are symmetric respect with respect to the $i = \frac{N+1}{2}$ path which is the straight line. The g score is calculated as:

$$g = \begin{cases} i & \text{if } i < (N+1)/2 \\ |i - N + 1| & \text{if } i > (N+1)/2 \\ 0 & \text{if } i = (N+1)/2 \end{cases}$$

h score: If the arc distance between the current node and target is smaller, the h score is lower. If there is collision with the bounding box or boarder, the h score would be very high. Assume P_n is the current node.

$$h = \begin{cases} ArcDis(P_n, Target) & \text{if no collision} \\ 10000 & \text{if collision} \end{cases}$$

The algorithm in this example operates as follows:

We start by calculating the five child nodes of the start point, the trajectory of each represented by a blue dashed line. We calculate the score respect with the target position and also check for overlap between obstacles and the corresponding bounding box. We then calculate that $x.1(Forward)$ is the closest node to the target point without

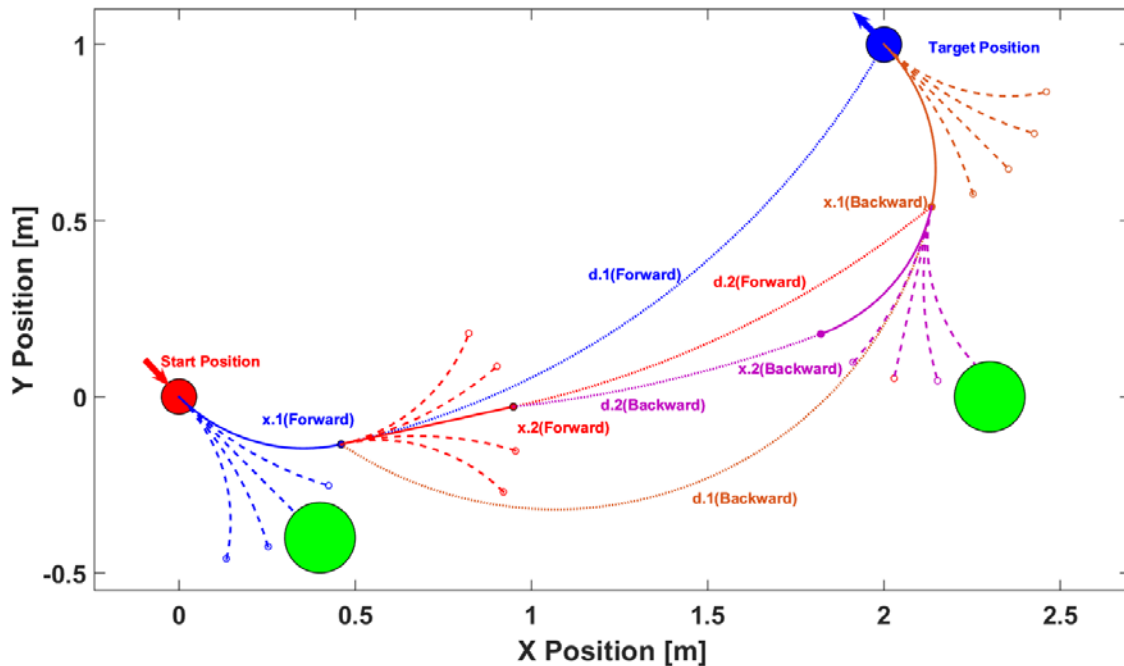


Figure 53 Motion planning algorithm example

collision. The blue solid line shows the CoM trajectory from the start point to the node $x.1(Forward)$. The blue dotted line shows the arc distance between the target point to the node $x.1(Forward)$.

As this is bidirectional, we next calculate the five child nodes of the target position. Then we calculate the arc distance between the children nodes and the node $x.1(Forward)$. The node $x.1(Backward)$ has the smallest arc distance respect to $x.1(Forward)$ without the collision based on the score. The brown solid line shows the CoM trajectory from the target point to the node $x.1(Backward)$. The brown dot line shows the arc distance between $x.1(Forward)$ and $x.1(Backward)$.

We calculate the five child nodes of $x.1(Forward)$ and observe that $x.2(Forward)$ is the best after calculating the arc distance respect with $x.1(Backward)$ without the collision. We repeat this, calculating the child nodes of $x.1(Backward)$ and

find that $x.2(Backward)$ is the best node after calculating the arc distance to $x.2(Forward)$ without collision.

We keep growing the tree from both directions until one of the following happens: the arc distance between the two newest nodes from the two direction is lower than the threshold and the difference between the rotation angles is π or until the arc distance is lower than the threshold. Then we can recover the whole path based on the forward and backward nodes.

In order to test the performance of this motion planning algorithm, we created a custom simulation environment, as shown in Figure 54(a). In this example, the start position and rotation was $(0,0,\pi/4)$ while the the target position and rotation was $(2,1,-3\pi/4)$. The linear velocity $v = 200$ mm/s. The max turning angle is $\pi/3$ with a resolution $N_{resolution} = 21$. The size of the bounding box is 50 mm and the right and left sides shift 10mm at the maximum turning angle and others are linear relationship with bending angle. There are up to 18 obstacles, each with diameter is 200 mm. We random choose the obstacles from only one obstacle to all 18, as seen in Figure 54(a). The algorithm ran 50 times for each configuration. Figure 54(b-e) shows different examples with 3, 5 and 8 obstacles and Figure 55 shows the general result of this algorithm. As the density of the obstacle is increased, the success rate is decreasing as expected. This algorithm is not optimal case because of the efficiency. Most of the path will be close to the obstacles.

5.2.2 Trajectory Following

After we generate the desired path using the previously discussed motion planning algorithm, then we need control the WPI SRS to actually follow the path. The node of the path is the desired position of the WPI SRS at each fixed time. As in a traditional mobile robot ^[74], we adjust the locomotion phase offset using the error between the current rotation and the rotation between the CoM position and the desired position. We also set the threshold which indicated the WPI is close enough to the desired point because it is in the continuous space. Therefore, the WPI SRS travels towards the first desired position, then the second, and so on until it is close enough to the final desired location. Figure 56 shows the simulation example of the WPI SRS following a pre-defined trajectory. First, we define the path at a constant linear velocity (200 mm/s) and the bending angle boundary ($-60^\circ, 60^\circ$) at every one second step, which represent the capabilities of the 2nd generation WPI SRS, then we implement and control our snake dynamic model. From the plot, WPI SRS is able to follow the trajectory very well.

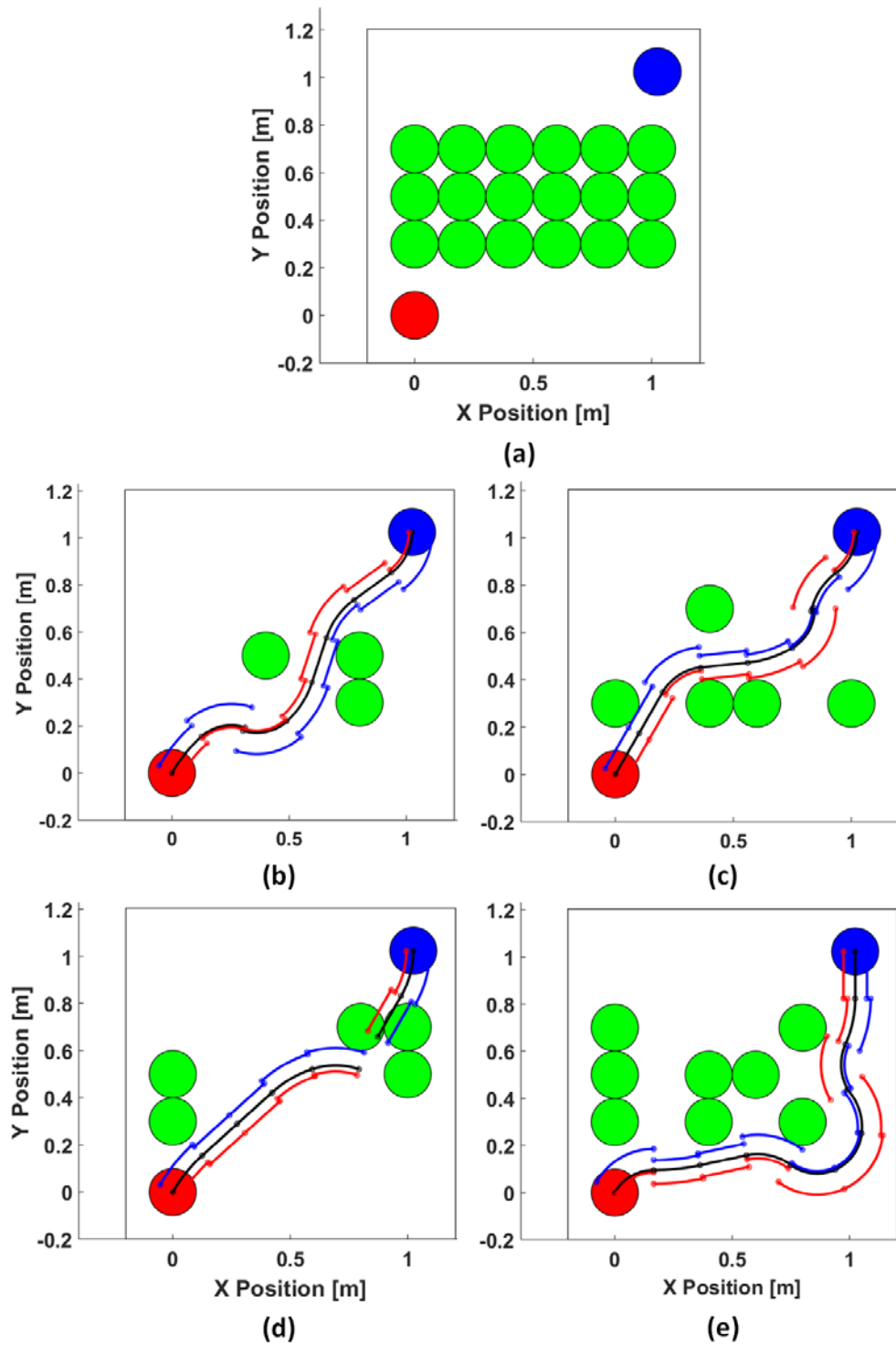


Figure 54 Motion planning algorithm simulation (a) Full obstacles (b) 3 obstacles (Succeeded) (c) 5 obstacles (Succeeded) (d) 5 obstacles (failed) (e) 8 obstacles (Succeeded).

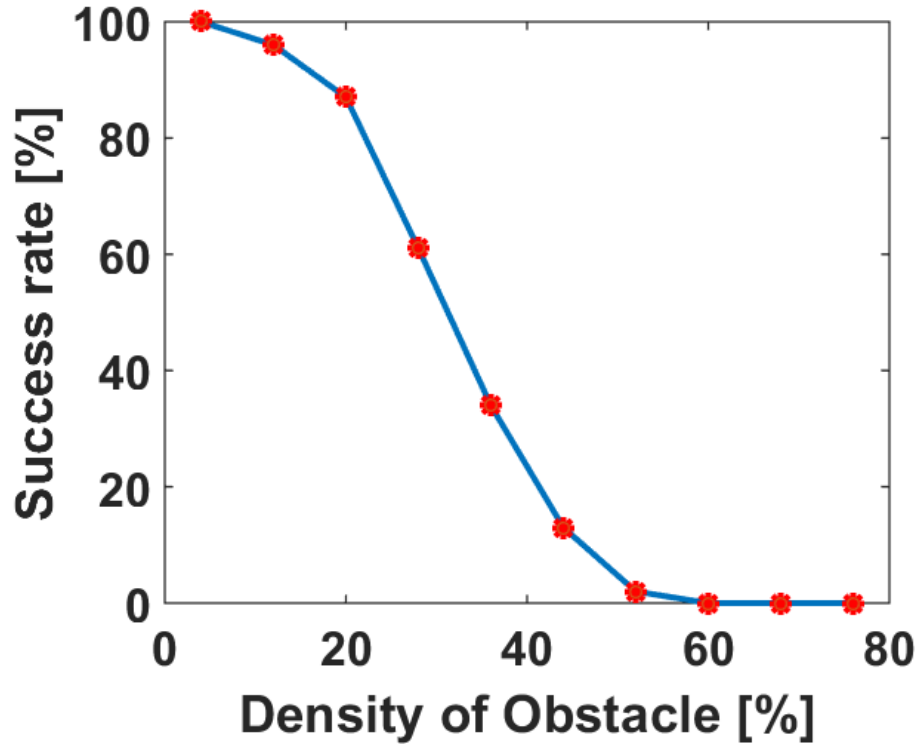


Figure 55 The performance of the motion planning algorithm

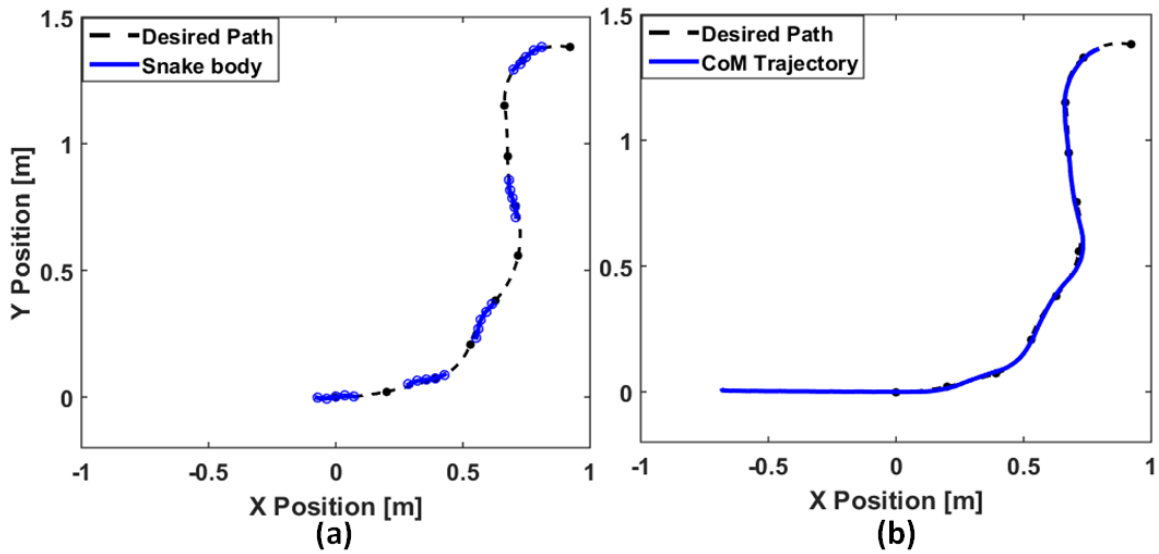


Figure 56 Trajectory following of the WPI SRS in simulation (a) shows the snake body and the desired path at some frame. (b) The desired path and the WPI SRS CoM trajectory.

5.2.3 Motion Planning and Trajectory Following Control Simulation

We simulated the WPI SRS in an obstacle-filled test environment in order to test to motion planning algorithm. First, we will plan a path based on the environment and the WPI SRS kinematic and dynamic information. Then we will control the WPI SRS following this path. We set the desired speed of the WPI SRS to be 200 mm/s and the width of the bounding box to be 50 mm, which is a little larger than the WPI SRS to allow for additional safety. We used a sample time $\Delta t = 1s$, with four obstacles in the environment. Figure 57(a) shows the WPI SRSs body is inside the bounding box as it follows the entire trajectory. Figure 57(b) shows that the CoM of the WPI SRS follows the desired trajectory very well.

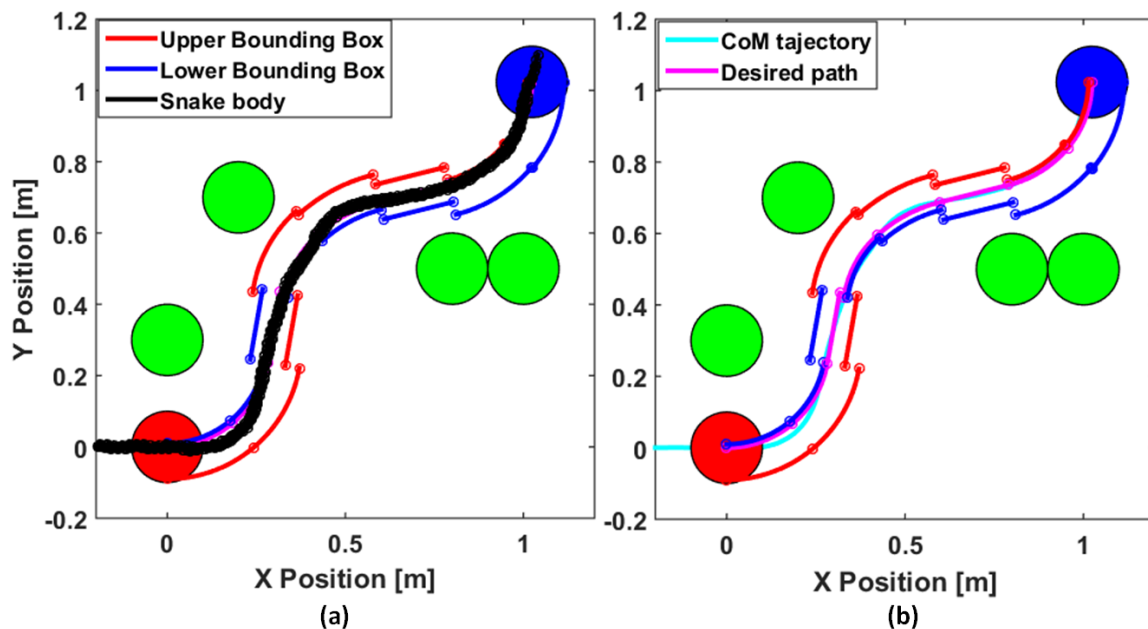


Figure 57 Motion planning and trajectory following simulation of WPI SRS. (a) The WPI SRS body in the simulation environment (b) The WPI SRS CoM trajectory in the simulation environment.

5.3 Experimental Verification

The procedure of the experimental verification was as follows: First, we experimentally determined the control properties of the 4th generation WPI SRS: Linear velocity, bounding box size and curvature boundary. Next, we plan a path for the WPI SRS using the previously-discussed motion planning algorithm and finally, we control the WPI SRS along this pre-defined path.

We ran the system using different phase offsets, from -0.3 to 0.3, using the ILC. With a phase offset of 0, which the WPI SRS would go straight line and the desired bending angle the ILC uses for each direction of the actuator is 0.7 rad. When the phase offset is between 0 and 0.3, the WPI SRS will turn in one direction. When using the ILC for this behavior, we set the desired bending angle for the large bending direction to be 0.7 rad and the desired angle for the smaller bending direction to be between 0.4 to 0.7 rad which is the linear relationship between 0.3 to 0. When the phase offset is between -0.3 to 0, the WPI SRS will turn the opposite direction and the desired angle for two directions of bending will be flipped, We record the position and orientation data of the SRS using the tracking system. Figure 58 shows the bounding box from the experimental result with a of frequency 1.5 Hz and a phase offset of 0.3.

We recorded the position of the entire body of the WPI SRS during its movement, and calculated the radius of curvature of its trajectory. To calculate the size of the corresponding bounding box, we calculated the radii that bound the positions of the SRS on the inside and the outside of its trajectory. Table 8 shows the experimental results of this experimentation, while Table 9 shows the values of the parameters we used in the

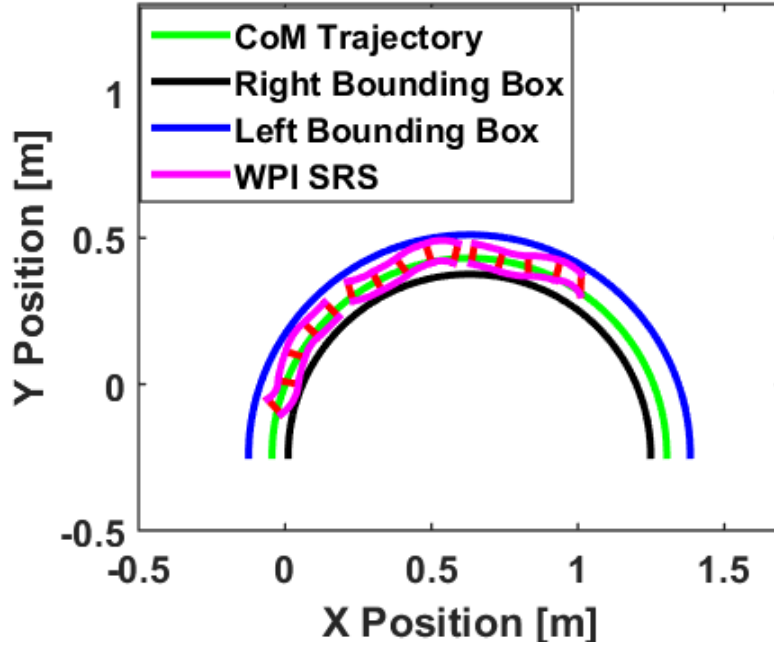


Figure 58 Bounding box from the experiment.

Table 8 Parameters Value of the experimental calibration

Offset	Linear Velocity m/s	Left Bounding Box m	Right Bounding Box m	Radius m
0	0.1345	-0.1	0.1	4.467
0.1	0.1524	-0.08	0.1	1.8157
0.2	0.1082	-0.07	0.1	1.2532
0.3	0.1216	-0.06	0.09	0.7856
-0.1	0.1696	-0.11	0.08	1.7707
-0.2	0.1489	-0.09	0.06	0.8445
-0.3	0.1471	-0.09	0.055	0.6727

Table 9 Parameters Value of the motion planning algorithm

Max turning angle	9°
Linear velocity	0.12m/s
Bounding box size	0.25m
Max shift	0.05m

motion planning algorithm. In order to make sure the WPI SRS did not collide with any obstacles, we used a larger bounding box for the motion planning than that calculated experimentally. The linear velocity of the WPI SRS is around 0.12 m/s. The turning radius is not symmetric respect with the different symbol offset because there has the bias of different actuators. We choose the smaller turning angle limit of the two direction be the curvature boundary, calculating a max turning rate of around 9 degrees per second. We experimentally verified the performance of the motion planning and trajectory following algorithm in three different obstacle-filled scenarios, as shown in Figures 59, 60, and 61. In these figures, we also show the planned path, the center of mass (CoM) trajectory of the actual snake behavior, and footprint of the soft body of the WPI SRS. Figure 59 shows the first scenario, where the target angle is 60° . From the plot, the desired path shows the WPI SRS could reach the target by crossing the gap between these obstacles. We can see that the snake robot has trouble following some of the tight curves dictated by the planner, despite the fact that these curves were calibrated to be achievable by the robot.

However, there are two factors that cause this inconsistency between calibration behavior and actual behavior: first, the speed of wireless communication between the snake and the control computer is slow, resulting in delay in the onset of commands. The frequency trajectory following is around 1000 Hz because it runs on the control computer and the frequency of the local ILC control is around 60 hz because of the limited bandwidth of the binary solenoid valves. The other factor is the translational state between the two far away states. For example, the previous phase offset is -0.3 and the current phase offset is 0.3, so the current turning radius would be larger the ideal radius

from phase 0.3 because the dynamic offset from previous offset -0.3 against the new dynamic input. The bounding box system considers the dynamic effect on the WPI SRS body within a control state but not between the two states translation. When this case happen, the WPI SRS will approach the desired point with a different orientation angle then planned for, as the trajectory following between nodes does not take into account orientation. However, the WPI SRS will converge the same orientation as the desired path after several nodes. From the Figure, we can see that the WPI SRS is able to reacquire the planned trajectory.

The second scenario (Figure 60) shows the desired path is outside from the obstacles because of the gap among these obstacles are too narrow. The target angle is 0° . This experimental performance are the same as the first scenario, WPI SRS could reach the target by following the path even there are some offsets when turning large angles. The third scenario (Figure 61) is the most difficult case, the planning path shows the WPI SRS should cross the gaps among these obstacles by traveling S paths. As the previous two cases, WPI SRS could achieve the task.

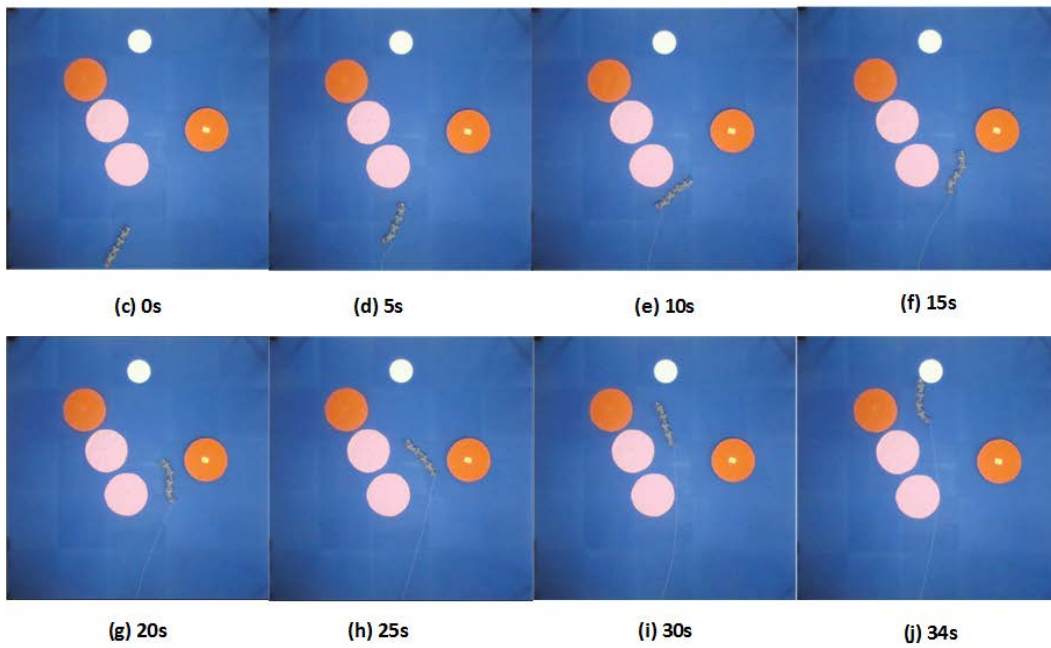
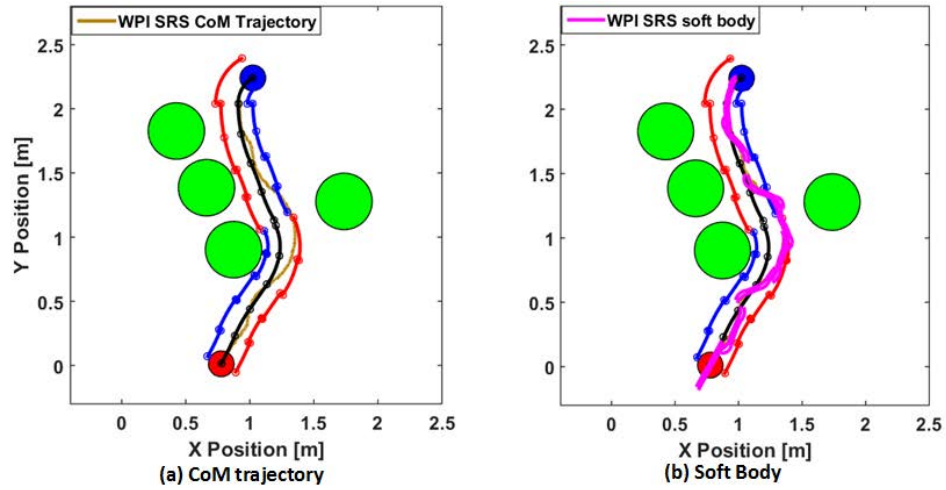


Figure 59 The first scenario experimental results (Target angle is 60°). (a) shows WPI SRS Center of Mass (CoM) and motion planning path and bounding box (b) shows WPI SRS soft body shape and motion planning path and bounding box. (c) (j) shows the snapshot of the experiment.

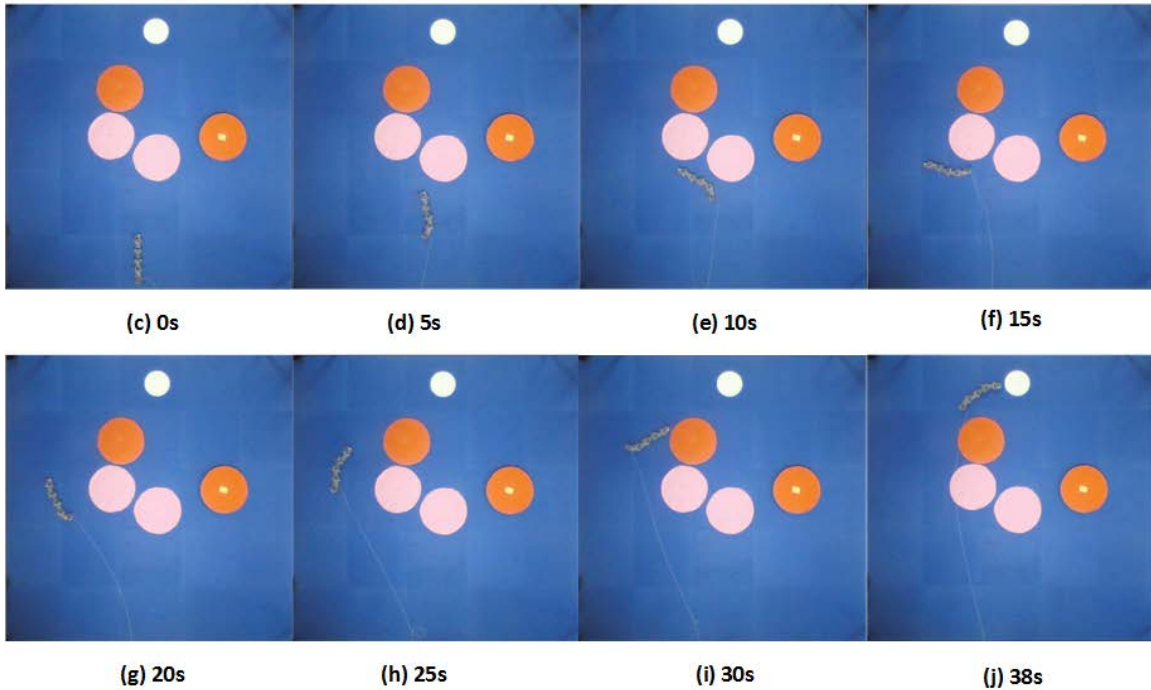
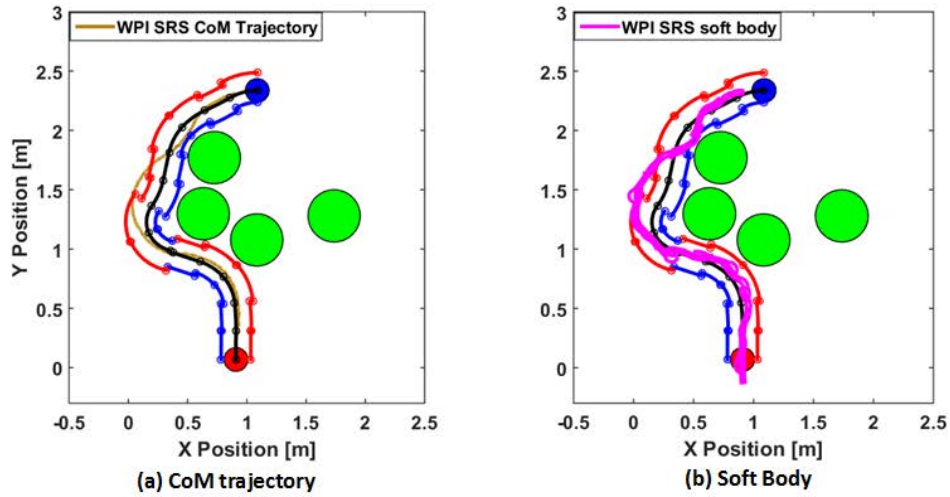


Figure 60 The second scenario experimental results (Target angle is 0°). (a) shows WPI SRS Center of Mass (CoM) and motion planning path and bounding box (b) shows WPI SRS soft body shape and motion planning path and bounding box. (c) (j) shows the snapshot of the experiment.

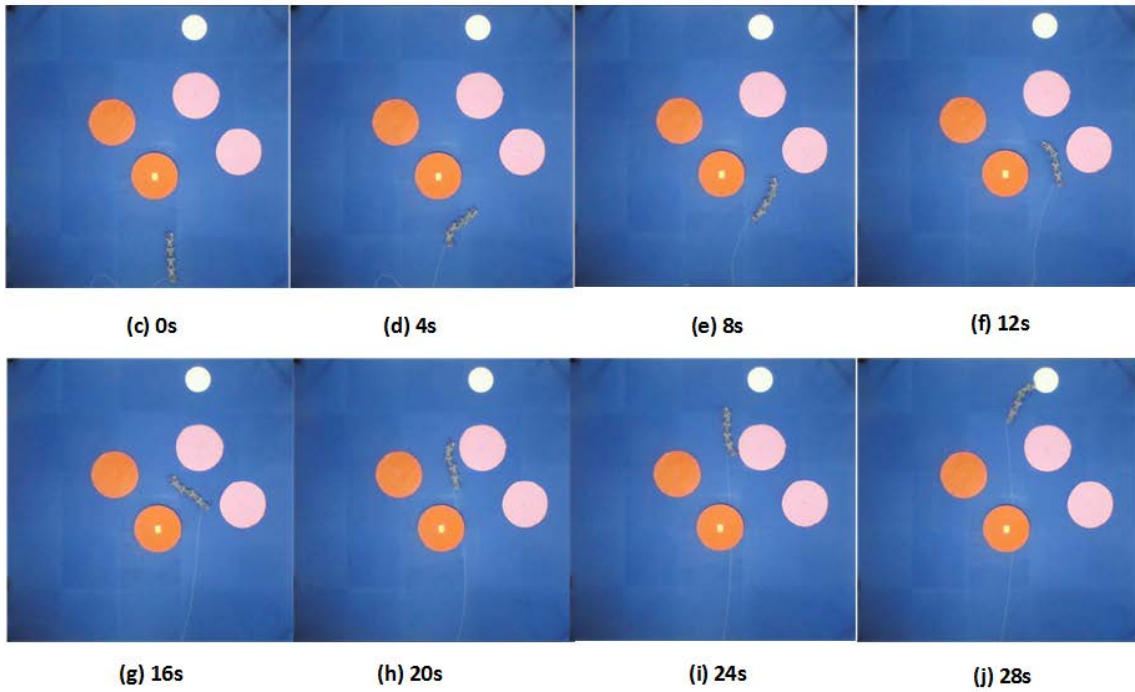
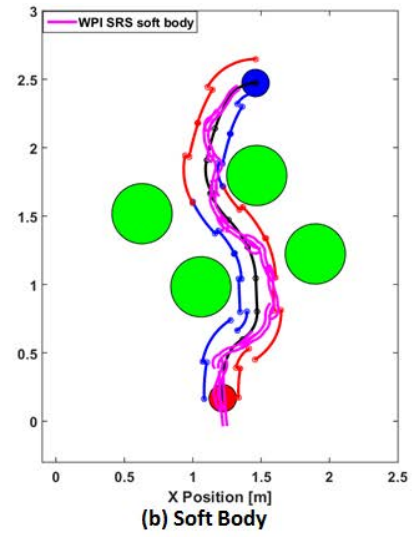
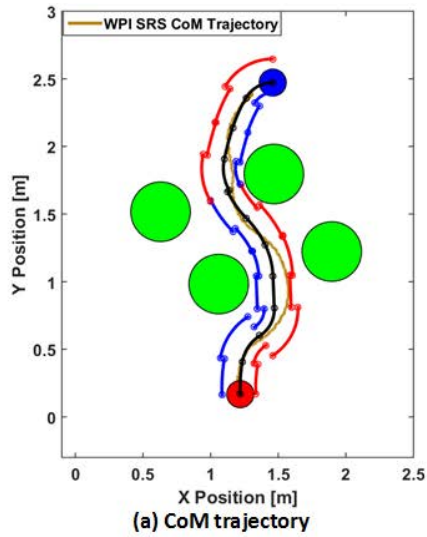


Figure 61 The third scenario experimental results (Target angle is 0°). (a) shows WPI SRS Center of Mass (CoM) and motion planning path and bounding box (b) shows WPI SRS soft body shape and motion planning path and bounding box. (c) (j) shows the snapshot of the experiment.

5.4 Conclusion

In this section, we proposed the fourth generation Worcester Polytechnic Institute soft robotic snake (WPI SRS) which is a modularized soft robotic system. Each soft bending module has own integrated controller, valves, and curvature sensor. Together, these modules can be controlled using a master controller, creating an autonomous mobile soft robot. To improve the reliability of path following, we implemented Iterative Learning Control (ILC) using the onboard curvature sensors. In addition, we designed a bounding box motion planning algorithm which is able to help WPI SRS find the path in the obstacle filled environment. This algorithm combines motion primitives with a simplified kinematic footprint of the WPI SRS, allowing it to simply plan achievable paths for this complex snake robot. We created a method for the SRS to follow these predetermined paths, and experimentally verified their accuracy.

Chapter 6

6. Conclusion

This dissertation explored research topics related to the development, modeling, and control of soft pneumatic robotic systems. Soft robots have many potential advantages over rigid robots in the areas of inspection, search and rescue, and other tasks in unknown environments. However, the lack of the modeling, control, and motion planning techniques for soft robots impedes their use. This dissertation address these problems in the context of the WPI SRS platform. A conclusion of this work is presented below with an extension of future work.

6.1 Summary of Work and contributions

During my PhD studying, I developed the four generation WPI SRS, The first version was similar with the one D. Rus's group developed in 2014, and like many current soft robotic systems, this early prototype was slow, with a maximum velocity of its center of mass (CoM) only around 20 mm/s, which is only one tenth its whole body length. In addition, it suffered from a lack of proprioceptive measurements and required external power source and electrical hardware, impeded advancements toward full autonomy. In 2015, we developed a new soft actuator which has a faster response and a higher pressure tolerance than the first soft actuator. Using this new actuator, the second generation WPI SRS was able to run a 220 mm/s, around one body length per second. This WPI SRS is the faster controllable soft robot in the world. In addition, we developed a dynamic model for soft robotic snakes combining established rigid snake modeling concepts and the soft actuator dynamic model. We verified this model experimentally. This work overcomes the complexities of the soft robotics modeling and make a foundation for the rest control and motion planning work. At the end of 2015, we debuted the third generation WPI SRS, which represented a self-contained and internal-state-sensing system. The power source, fluid source and the electrical circuits were mounted on the robot body and custom flexible magnetic curvature sensor is embedded in the constraint layer of each soft. We optimized the curvature sensor parameters using FEA based on the functional requirement of the WPI SRS. However, for autonomous mobile robot tasks, the third generation WPI SRS still needed to be improved upon. The soft actuators were unreliable and the system had low scalability, being highly depend on the

size of the 3D printer mold and the capability of the master controller. The third generation WPI SRS also had very low maneuverability, severely limiting its ability to achieve manipulation, inspection and other more challenging tasks. In order to make the WPI SRS robot more practical, in 2016 we designed a soft actuator module with integrated curvature sensor and own independent control board. This actuator used an advanced fabrication technique that made it more reliable than our previous actuators. We implemented an iterative sliding mode controller and direct sliding model on a single soft module to achieve the best performance with limited bandwidth in preparation for manipulation and inspection some future tasks. We connected these independent modules in series to create the fourth generation WPI SRS. This version of the WPI SRS can self-correct its own motion using its on-board curvature sensor and an iterative learning algorithm without needing external sensing technology. In addition, I proposed a motion planning and trajectory following algorithm for WPI SRS. In this algorithm, we first defined a bounding box, which is a simple geometric structure contain the infinite degree of freedom kinematic and nonlinear dynamic information of the WPI SRS. Then I plan a path for WPI SRS though an obstacle-filled environment using an A*-based algorithm. Last, WPI SRS will follow the pre-defined trajectory using the iterative learning controller. Table shows the comparison of four generation WPI SRS.

Table 10 Performance comparison of the four WPI SRS generations

Generation	Advantages	Disadvantages
First (2013)	First soft robotic snake	Slow (Max 22 mm/s), No feedback, tethered
Second (2014)	Fast locomotion (Max 214 mm/s)	No feedback, tethered, not scalable
Third (2015)	Tetherless, Curvature feedback	Slow (Max 50 mm/s), Unreliable, Not scalable
Forth (2017)	Modularized, Reliable, Scalable	External air source

6.2 Future Work

The optimization of the WPI SRS

Chapter 3 introduced the precise dynamic model of the WPI SRS. It shows that the usability of the WPI SRS's serpentine gate depends on the surface friction coefficients, the dynamics of the soft actuator, the locomotion gait parameters and the dimensions of the WPI SRS. The characteristics of the fourth generation WPI SRS were chosen arbitrarily, and with convenience in mind. Therefore, we could use the models to optimize the mechanical design of the WPI SRS mechanical design. In addition, we also could optimize the WPI SRS movability on the different surface and different tasks.

The optimal control of the redundant WPI SRS

The latest WPI SRS is a modularized system that can have modules easily added or removed depending on the task. A higher number of links allows for more possible motions but also increase the computation time and the energy loss. The required number of links would depend on the desired task. For example, a manipulation task might need more numbers actuators in control while a pure locomotion task may need fewer actuators. In addition, for a given physical configuration, not all actuators need to be actuated in order to complete the current task. Thus, there is work that can be done optimizing the energy efficiency both by changing the snake structure and changing the control strategies.

The manipulation of the WPI SRS

WPI SRS has the complaint soft structure which is advantageous for manipulation tasks. Unlike the rigid robots, the force feedback sensor and the algorithm make the

system complaint. Therefore, performing manipulation tasks using the WPI SRS is an interesting topic, especially when combined with movement. Chapter 4 shows the control performance of a single module, which can be used as the low level controller for a manipulation task. For high level motion planning, developing a grasping algorithm which combines the whole-snake dynamics with the soft manipulator is a challenge because most manipulators assume a stationary base.

The obstacle contact locomotion of the WPI SRS

In very rocky environments, snakes will make use of obstacle contact in order to increase the efficiency of their locomotion. We would like to investigate ways of employing this technique as well. Currently, a few rigid robots have this capacity, making use of series-elastic joints. The WPI SRS is more similar to a biological snake because of its soft body. However, force measurement with a rigid snake is easier because of the linear spring and all of the deformation concentrated at the joint, whereas the WPI SRS would lose its constant segment curvature. Therefore, attempting to measure the contact forces and predicting the soft actuator's shape is an interesting topic.

The 3 Dimensional WPI SRS

The current WPI SRS is only able to traverse 2D flat surfaces. Chapter 1 shows that biological snakes can travel through complex environment with four different locomotion types. All capabilities of the snake require the soft actuators have 2 degrees of freedom. We would like to create a version of the WPI SRS with these same capabilities, and then implement the different locomotion types, particularly sidewinding. In order to do this, each single soft actuator would require a 2-DoF curvature sensor, necessitating a

significant redesign. The bounding box motion planning concept would become more complex because the bending shape soft now must take into account the effects of gravity.

Reference

- [1] C. Lee, M. Kim, Y. J. Kim, N. Hong, S. Ryu, H. J. Kim, and S. Kim. "Soft robot review," *International Journal of Control, Automation and Systems*, 15(1), 3-15 (2007)
- [2] D. Rus and M. T. Tolley. "Design, fabrication and control of soft robots," *Nature*, 521(7553), 467-475 (2015).
- [3] K. J. Dowling. "Limbless locomotion: learning to crawl with a snake robot" (*Doctoral dissertation, NASA*) (1996).
- [4] S. Bino, and H. Choset. "Survey on urban search and rescue robots." *Journal of the Robotics Society of Japan* 22.5(2004): 582-586.
- [5] Snake locomotion. [Online]. Available: <https://www.ucs.louisiana.edu/~brm2286/locomotn.htm>
- [6] C. D. Onal and D. Rus. "Autonomous undulatory serpentine locomotion utilizing body dynamics of a fluidic soft robot". *Bioinspiration & biomimetics*, 8(2), 026003 (2013).
- [7] Hirose, Shigeo, Peter Cave, and Charles Goulden. Biologically inspired robots: serpentine locomotors and manipulators. *Oxford University Press*, 1993.
- [8] S. Hirose, "Biologically Inspired Robots: Snake-like Locomotors and Manipulators", Oxford University Press (1993).
- [9] S. Hirose, H. Yamada. "Snake-like robots [tutorial]". *IEEE Robotics & Automation Magazine*, 16(1), 88-98 (2009).
- [10] R. Bogue, "Snake robots: A review of research, products and applications", *Industrial Robot: An International Journal*, 41(3), 253-258 (2014).
- [11] J. K. Hopkins, B. W. Spranklin and Gupta, S. K. "A survey of snake-inspired robot designs". *Bioinspiration & biomimetics*, 4(2), 021001 (2009).
- [12] M. Mori and S. Hirose, S. "Three-dimensional serpentine motion and lateral rolling by active cord mechanism ACM-R3." *In Intelligent Robots and Systems, 2002. IEEE/RSJ International Conference on (Vol. 1, pp. 829-834). IEEE* (2002).
- [13] H. Yamada and S. Hirose. "Development of practical 3-dimensional active cord mechanism ACM-R4." *Journal of Robotics and Mechatronics*, 18(3), 305 (2006).
- [14] Mori, Makoto, and Shigeo Hirose. "Three-dimensional serpentine motion and lateral rolling by active cord mechanism ACM-R3." *Intelligent Robots and Systems, 2002. IEEE/RSJ International Conference on. Vol. 1. IEEE, 2002.*
- [15] P. Liljebäck, O. Stavdahl, and A. Beitnes. "SnakeFighter-development of a water hydraulic fire fighting snake robot. In Control", *Automation, Robotics and Vision, 2006. ICARCV'06. 9th International Conference on (pp. 1-6). IEEE* (2006).
- [16] A. A. Transteth, R. I. Leine, C. Glocker and K. Y. Pettersen. "3-D snake robot motion: Nonsmooth modeling, simulations, and experiments." *IEEE Transactions on Robotics*, 24(2), 361-376 (2008).
- [17] A. A. Transteth, R. I. Leine, C. Glocker, K. Y. Pettersen, and P. Liljebäck. "Snake robot obstacle-aided locomotion: Modeling, simulations, and experiments." *IEEE Transactions on Robotics*, 24(1), 88-104. (2008).
- [18] S. A. Fjordingen, P. Liljebäck, and A. A. Transteth. "A snake-like robot for internal inspection of complex pipe structures (PIKo)." *In Intelligent Robots and Systems, IROS, IEEE/RSJ International Conference on (pp. 5665-5671). IEEE* (2009).
- [19] C. Wright, A. Johnson, A. Peck, Z. McCord, A. Naaktgeboren, P. Gianfortoni, G.R. Manuel, Hatton.R and H. Choset. "Design of a modular snake robot. In Intelligent Robots and Systems", *IROS 2007, IEEE/RSJ International Conference on (pp. 2609-2614). IEEE.* (2007)
- [20] J. C. McKenna, D. J. Anhalt, F. M. Bronson, H. B. Brown, M. Schwerin, E. Shammass and H. Choset. "Toroidal skin drive for snake robot locomotion." *In Robotics and Automation, 2008. ICRA 2008. IEEE International Conference on (pp. 1150-1155). IEEE* (2008).
- [21] C. Wright, A. Buchan, B. Brown, J. Geist, M. Schwerin, D. Rollinson and H. Choset (2012, May). "Design and architecture of the unified modular snake robot." *In Robotics and Automation (ICRA), 2012 IEEE International Conference on (pp. 4347-4354). IEEE* (2012).
- [22] A. Crespi and A. J. Ijspeert, A. J. "AmphiBot II: An amphibious snake robot that crawls and swims using a central pattern generator." *In Proceedings of the 9th international conference on climbing and walking robots (CLAWAR 2006) (No. BIOROB-CONF-2006-001, pp. 19-27) (2006).*
- [23] A. Crespi, A. Badertscher, A. Guignard and A. J. Ijspeert. "AmphiBot I: an amphibious snake-like robot." *Robotics and Autonomous Systems*, 50(4), 163-175. (2005).

- [24] A. Crespi, A. Badertscher, A. Guignard and A. J. Ijspeert. "Swimming and crawling with an amphibious snake robot." *Robotics and Automation, Proceedings of the 2005 IEEE International Conference on. IEEE*, 2005.
- [25] G. Granosik, M.G.Hansen, and J. Borenstein. "The OmniTread serpentine robot for industrial inspection and surveillance." *Industrial Robot: An International Journal*, 32(2), 139-148. (2005)
- [26] J. Borenstein, M. Hansen and A. Borrell. "The OmniTread OT - 4 serpentine robot—design and performance." *Journal of Field Robotics*, 24(7), 601-621 (2007).
- [27] M. Sato, M. Fukaya, and T. Iwasaki, "Serpentine locomotion with robotic snakes," *IEEE Control Systems*, vol. 22, no. 1, pp. 64-81, (2002).
- [28] S. A. Fjerdingen, J. Mathiassen, H. Schumann-Olsen and E. Kyrkjeb, "Adaptive snake robot locomotion: a benchmarking facility for experiments," in *European Robotics Symposium, Springer*, pp. 13-22 (2008).
- [29] M. Shugen, "Analysis of creeping locomotion of a snake-like robot," *Advanced Robotics*, vol. 15, no. 2, pp. 205-224, (2001).
- [30] K.Y. Pettersen, Ø. Stavdahl and J.T. Gravdahl. "Snake Robots: Modelling, Mechatronics, and Control." *New York: Springer*, (2013)
- [31] F. Matsuno, and S. Kentaro. "Control of redundant 3D snake robot based on kinematic model." *Robotics and Automation, 2003. Proceedings. ICRA '03. IEEE International Conference on. Vol. 2. IEEE*, (2003).
- [32] S. Seok, C. D. Onal, K.J. Cho, R. J. Wood, D. Rus and S. Kim "Meshworm: a peristaltic soft robot with antagonistic nickel titanium coil actuators." *IEEE/ASME Transactions on mechatronics* 18.5 (2013): 1485-1497.
- [33] Y. S. Song, Y. Sun, R. Brand, J. Zitzewitz, S. Micera, G. Courtine and J. Park. "Soft robot for gait rehabilitation of spinalized rodents." *Intelligent Robots and Systems (IROS), 2013 IEEE/RSJ International Conference on. IEEE*, 2013.
- [34] M. Carmel. "Soft robotics: a perspective—current trends and prospects for the future." *Soft Robotics* 1.1 (2014): 5-11.
- [35] B. A. Trimmer, H. Lin, A. Baryshyan, G. G. Leisk and D. L. Kaplan. "Towards a biomorphic soft robot: design constraints and solutions." *Biomedical Robotics and Biomechatronics (BioRob), 2012 4th IEEE RAS & EMBS International Conference on. IEEE*, 2012.
- [36] S. Yuuta, and S. Hirai. "Crawling and jumping of deformable soft robot." *Intelligent Robots and Systems, 2004.(IROS 2004). Proceedings. 2004 IEEE/RSJ International Conference on. Vol. 4. IEEE*, 2004.
- [37] K. Sangbae, C.Laschi, and B.A.Trimmer. "Soft robotics: a bioinspired evolution in robotics." *Trends in biotechnology* 31.5 (2013): 287-294.
- [38] B. Antonio, G.Tonietti, and E. Piaggio. "Design, realization and control of soft robot arms for intrinsically safe interaction with humans." *Proc. IARP/RAS Workshop on Technical Challenges for Dependable Robots in Human Environments*. 2002.
- [39] S. Mao, E. Dong, H. Jin, M. Xu, S. Zhang, J. Yang and K.H.Low. "Gait study and pattern generation of a starfish-like soft robot with flexible rays actuated by SMAs." *Journal of Bionic Engineering* 11.3 (2014): 400-411.
- [40] B. Antonio, and G. Tonietti. "Fast and" soft-arm" tactics [robot arm design]." *IEEE Robotics & Automation Magazine* 11.2 (2004): 22-33.
- [41] H. Jonathan, and H. Lipson. "Automatic design and manufacture of soft robots." *IEEE Transactions on Robotics* 28.2 (2012): 457-466.
- [42] H. F. Schulte. "The characteristics of the McKibben artificial muscle." *The application of external power in prosthetics and orthotics*, 874, 94-115, (1961).
- [43] G. K. Klute, J. M. Czerniecki and B. Hannaford. "McKibben artificial muscles: pneumatic actuators with biomechanical intelligence." In *Advanced Intelligent Mechatronics, 1999. Proceedings. 1999 IEEE/ASME International Conference on* (pp. 221-226). *IEEE* (1999).
- [44] B. Tondu, and L. Pierre. "Modeling and control of McKibben artificial muscle robot actuators." *IEEE control systems* 20.2 (2000): 15-38.
- [45] R. F. Shepherd, F. Fllievski, W. Choi, S.A.Morin, A.A. Stokes, A.D. Mazzeo, C. Xin, W. Michael and G.M. Whitesides. "Multigait soft robot". *Proceedings of the National Academy of Sciences*, 108(51), 20400-20403, (2011).
- [46] S. A. Morin, R. F. Shephend, S. W. Kwok, A. A. Stokes, A. Nemiroski and G. M. Whitesides. "Camouflage and display for soft machines." *Science* 337.6096 (2012): 828-832.
- [47] M. T. Tolley, R. F. Shepherd, B. Mosadegh, K. C. Galloway, M. Wehner, M. Karpelson, R. J. Wood and G.M. Whitesides. "A resilient, untethered soft robot." *Soft Robotics*, 1(3), 213-223. (2014).
- [48] S. A. Morin, R. F. Shepherd, S. W. Kwok, A. A. Stokes, A. Nemiroski and G.M. Whitesides. "Camouflage and display for soft machines." *Science*, 337(6096), 828-832 (2012).

- [49] R. F. Shepherd, A. A. Stokes, J. Freake, J Barber, P.W. Snyder, A. D. Mazzeo, L. Cademartiri, S. A. Morin, and G. M. Whiteside "Using explosions to power a soft robot." *Angewandte Chemie* 125.10 (2013): 2964-2968.
- [50] N. W. Bartlett, M. Tolley, J. T. B. Overvelde, J. C Weaver, B. Mosadegh, K. Bertoldi, G. M. Whitesides and R. J. Wood. "A 3D-printed, functionally graded soft robot powered by combustion." *Science*, 349(6244), 161-165. (2015)
- [51] M. Wehner, R. L. Truby, D. J. Fitzgerald, B. Mosadegh, G.M. Whitesides, J.A. Lewis and R.J. Wood. "An integrated design and fabrication strategy for entirely soft, autonomous robots." *Nature*, 536(7617), 451-455, (2006).
- [52] C. Laschi. "Octobot-A robot octopus points the way to soft robotics." *IEEE Spectrum*, 54(3), 38-43 (2017).
- [53] H. T. Lin, G. G. Leisk, and B. Trimmer. "GoQBot: a caterpillar-inspired soft-bodied rolling robot." *Bioinspiration & biomimetics*, 6(2), 026007. (2011).
- [54] B. A. Trimmer, A.E. Takesian and B.M. Sweet. "Caterpillar locomotion: a new model for soft-bodied climbing and burrowing robots." *7th International Symposium on Technology and the Mine Problem. Vol. 1. Monterey, CA: Mine Warfare Association*, 2006.
- [55] H. Lin, A. L. Dorfmann, and B. A. Trimmer. "Soft-cuticle biomechanics: a constitutive model of anisotropy for caterpillar integument." *Journal of Theoretical Biology* 256.3 (2009): 447-457.
- [56] A. D. Marchese, C. D. Onal and D. Rus. "Towards a self-contained soft robotic fish: on-board pressure generation and embedded electro-permanent magnet valves." *Experimental Robotics. Springer International Publishing*, 2013.
- [57] A. D. Marchese, C. D. Onal and D. Rus. "Autonomous soft robotic fish capable of escape maneuvers using fluidic elastomer actuators." *Soft Robotics*, 1(1), 75-87. (2014).
- [58] R. K. Katzschmann, A. D. Marchese and D. Rus. "Hydraulic autonomous soft robotic fish for 3D swimming." *In Experimental Robotics (pp. 405-420). Springer International Publishing*. (2016).
- [59] A. D. Marchese, R. Tedrake and D. Rus. "Dynamics and trajectory optimization for a soft spatial fluidic elastomer manipulator." *The International Journal of Robotics Research*, 35(8), 1000-1019. (2016)
- [60] A. D. Marchese, K. Komorowski, C. D. Onal and D. Rus. "Design and control of a soft and continuously deformable 2d robotic manipulation system." *Robotics and Automation (ICRA), 2014 IEEE International Conference on. IEEE*, 2014.
- [61] A. D. Marchese, R. K. Katzschmann and Rus. "A recipe for soft fluidic elastomer robots." *Soft Robotics*, 2(1), 7-25 (2015).
- [62] E. T. Roche, M. A. Horvath, I. Wamala, A. Alazmani, S. E. Song, W. Whyte, Z. Machaidze, C. J. Payne, J. C. Weaver, G. Fishbein, J. Kuebler, N.V. Vasilyev, D. J. Mooney, F. A. Pigula and C. J. Walsh. "Soft robotic sleeve supports heart function." *Science Translational Medicine*, 9(373), (2017)
- [63] E. T. Roche, M. A. Horvath, A. Alazmani, K.C. Galloway, N.V. Vasilyev, D. J. Mooney, F. A. Pigula and C. J. Walsh. "Design and fabrication of a soft robotic direct cardiac compression device." *Proceedings of the ASME 2015 International Design Engineering Technical Conferences & Computers and Information in Engineering Conference (IDETC/CIE 2015)*, Boston, MA. 2015.
- [64] P. Polygerinos, Z. Wang, K. C. Galloway, R. J. Wood and C.J. Walsh. "Soft robotic glove for combined assistance and at-home rehabilitation." *Robotics and Autonomous Systems*, 73, 135-143, (2015).
- [65] P. Polygerinos, K. C. Galloway, E. Savage, M. Herman, K. O'Donnell and C.J. Walsh. "Soft robotic glove for hand rehabilitation and task specific training." *In Robotics and Automation (ICRA), IEEE International Conference on (pp. 2913-2919)*, (2015).
- [66] P. Polygerinos, S. Lyne, Z. Wang, L. Fernando, N. B. Mosadegh, G. M. Whitesides, C. J. Walsh. "Towards a soft pneumatic glove for hand rehabilitation." *Intelligent Robots and Systems (IROS), 2013 IEEE/RSJ International Conference on. IEEE*, 2013.
- [67] M. Calisti, M. Giorelli, G. Levy, B. Mazzolai, B. Hochner, C. Laschi and P. Dario. "An octopus-bioinspired solution to movement and manipulation for soft robots." *Bioinspiration & biomimetics*, 6(3), 036002, (2011)
- [68] M. Cianchetti, M. Calisti, L. Margheri, M. Kuba and C. Laschi. "Bioinspired locomotion and grasping in water: the soft eight-arm OCTOPUS robot." *Bioinspiration & biomimetics*, 10(3), 035003 (2015)
- [69] C. Laschi and M. Cianchetti. "Soft robotics: new perspectives for robot bodyware and control." *Frontiers in bioengineering and biotechnology* 2 (2014).
- [70] F. Renda, M. Giorelli, M. Calisti, M. Cianchetti and C. Laschi. "Dynamic model of a multibending soft robot arm driven by cables." *IEEE Transactions on Robotics* 30.5 (2014): 1109-1122.
- [71] N. Xydias, M. Bhagavat and I. Kao. "Study of soft-finger contact mechanics using finite elements analysis and experiments." *In Robotics and Automation. Proceedings. ICRA'00. IEEE International Conference on (Vol. 3, pp. 2179-2184). IEEE* (2000).
- [72] F. Ilievski, A. D. Mazzeo, R.F. Shepherd, X. Chen and G. M. Whitesides. "Soft robotics for chemists." *Angewandte Chemie*, 123(8), 1930-1935. (2011)

- [73] P. Moseley, J. M. Florez, H. A. Sonar, G. Agarwal, W. Curtin, and J. Paik. "Modeling, design, and development of soft pneumatic actuators with finite element method." *Advanced Engineering Materials* (2015).
- [74] P. Polygerinos, Z. Wang, J. T. Overvelde, K. C. Galloway, R. J. Wood, K. Bertoldi and C. J. Walsh. "Modeling of soft fiber-reinforced bending actuators." *IEEE Transactions on Robotics*, 31(3), 778-789 (2015).
- [75] J. Bishop-Moser, G. Krishnan and S. Kota. "Force and hydraulic displacement amplification of fiber reinforced soft actuators." In *ASME 2013 International Design Engineering Technical Conferences and Computers and Information in Engineering Conference* (pp. V06AT07A031-V06AT07A031). American Society of Mechanical Engineers (2013).
- [76] G. Krishnan, J. Bishop-Moser, C. Kim and S. Kota. "Evaluating mobility behavior of fluid filled fiber-reinforced elastomeric enclosures." In *ASME 2012 International Design Engineering Technical Conferences and Computers and Information in Engineering Conference* (pp. 1089-1099). American Society of Mechanical Engineers (2012).
- [77] N. Tsagarakis, D. G. Caldwell. "Improved modelling and assessment of pneumatic muscle actuators." In *Robotics and Automation, Proceedings. ICRA '00. IEEE International Conference on* (Vol. 4, pp. 3641-3646). IEEE (2000).
- [78] M. Luo, E. H. Skorina, W. Tao, F. Chen and C. D. Onal. "Optimized design of a rigid kinematic module for antagonistic soft actuation." In *Technologies for Practical Robot Applications (TePRA), 2015 IEEE International Conference on* (pp. 1-6). IEEE (2015).
- [79] J. C. Case, E. L. White and R. K. Kramer. "Soft material characterization for robotic applications." *Soft Robotics*, 2(2), 80-87 (2015).
- [80] B. Kim, S. B. Lee, J. Lee, S. Cho, H. Park, H. S. Yeom and S. H. Park. "A comparison among Neo-Hookean model, Mooney-Rivlin model, and Ogden model for chloroprene rubber." *International Journal of Precision Engineering and Manufacturing*, 13(5), 759-764 (2012).
- [81] R. W. Ogden. "Large deformation isotropic elasticity-on the correlation of theory and experiment for incompressible rubberlike solids." In *Proceedings of the Royal Society of London A: Mathematical, Physical and Engineering Sciences* (Vol. 326, No. 1567, pp. 565-584). The Royal Society (1972).
- [82] C. S. Kothera, M. Jangid, J. Sirohi and N. M. Wereley. "Experimental characterization and static modeling of McKibben actuators." *Journal of Mechanical Design*, 131(9), 091010 (2009).
- [83] H. E. Holling, H. C. Boland and E. Russ. "Investigation of arterial obstruction using a mercury-in-rubber strain gauge." *American heart journal*, 62(2), 194-205 (1961).
- [84] R. K. Kramer, C. Majidi, R. Sahai and R. J. Wood. "Soft curvature sensors for joint angle proprioception." In *Intelligent Robots and Systems (IROS), 2011 IEEE/RSJ International Conference on* (pp. 1919-1926). IEEE (2011).
- [85] R. K. Kramer, C. Majidi and R. J. Wood, R. J. "Wearable tactile keypad with stretchable artificial skin." In *Robotics and Automation (ICRA)*, 2011 IEEE International Conference on (pp. 1103-1107). IEEE (2011).
- [86] S. Ozel, E. H. Skorina, M. Luo, W. Tao, F. Chen, Y. Pan and C. D. Onal, C. D. "A composite soft bending actuation module with integrated curvature sensing." In *Robotics and Automation (ICRA), 2016 IEEE International Conference on* (pp. 4963-4968). IEEE (2016).
- [87] Y. L. Park, K. Chau, R. J. Black and M. R. Cutkosky. "Force sensing robot fingers using embedded fiber Bragg grating sensors and shape deposition manufacturing." In *Robotics and Automation, 2007 IEEE International Conference on* (pp. 1510-1516). IEEE (2007).
- [88] J. Yi, X. Zhu, L. Shen, B. Sun and L. Jiang. "An orthogonal curvature fiber bragg grating sensor array for shape reconstruction." In *Life System Modeling and Intelligent Computing* (pp. 25-31). Springer Berlin Heidelberg (2010).
- [89] M. Luo, Y. Pan, W. Tao, F. Chen, E.H. Skorina, C.D. Onal, "Refined Theoretical Modeling of a New-generation Pressure-operated Soft Snake", *Proceedings of the ASME International Design Engineering Technical Conferences & Computers and Information in Engineering Conference (IDETC/CIE)*, (2015).
- [90] M. Luo, W. Tao, F. Chen, T.K. Khuu, S. Ozel, C.D. Onal, "Design Improvements and Dynamic Characterization on Fluidic Elastomer Actuators for a Soft Robotic Snake", *IEEE International Conference on Technologies for Practical Robot Applications (TePRA)*, (2014).
- [91] M. Luo, Y. Pan, E.H. Skorina, W. Tao, F. Chen, S. Ozel, C.D. Onal, "Slithering towards autonomy: a self-contained soft robotic snake platform with integrated curvature sensing", *Bioinspiration & Biomimetics* 10:055001, (2015).
- [92] M. Luo, M. Agheli, C.D. Onal, "Theoretical Modeling and Experimental Analysis of a Pressure-Operated Soft Robotic Snake", *Soft Robotics*, 1(2):136-146 (2014).
- [93] M. Luo, M. Agheli, C.D. Onal, "Theoretical Modeling of a Pressure-Operated Soft Snake Robot", *Proceedings of the ASME 2014 International Design Engineering Technical Conferences & Computers and Information in Engineering Conference (IDETC/CIE)*, (2014).

- [94] W. Tao, E.H. Skorina, F. Chen, J. McInnis, M. Luo C.D. Onal, "Bioinspired Design and Fabrication Principles of Reliable Fluidic Soft Actuation Modules", *IEEE International Conference on Robotics and Biomimetics (ROBIO)*, 2169-2174, (2015).
- [95] S. Ozel, E.H. Skorina, M. Luo, W. Tao, F. Chen, Y. Pan, C.D. Onal, "A Composite Soft Bending Actuation Module with Integrated Curvature Sensing", *IEEE International Conference on Robotics and Automation (ICRA)* pp. 4963-4968, (2016).
- [96] M. Luo, E. H. Skorina, W. Tao, F. Chen, S. Ozel, Y. Sun and C. D. Onal. "Toward Modular Soft Robotics: Proprioceptive Curvature Sensing and Sliding-Mode Control of Soft Bidirectional Bending Modules". *Soft Robotics*, (2017)
- [97] E. H. Skorina, M. Luo, W. Tao, F. Chen, J. Fu, C. D. Onal, "Adapting to Flexibility: Model Reference Adaptive Control of Soft Bending Actuators", *IEEE Robotics and Automation Letters*, (2017)
- [98] M. Luo, F. Chen, E.H. Skorina, W.Tao, Y. Sun., and C.D.Onal. " Motion Planning and Iterative Learning Control of a Pressure-operated Modular Soft Robotic Snake." *The International Journal of Robotics Research 2017* (under review).
- [99] K. L. Moore and X. J. Xu. "Iterative learning control." Taylor & Francis (2000).
- [100] R. Siegwart, I. R. Nourbakhsh and D. Scaramuzza. "Introduction to autonomous mobile robots." MIT press (2011).
- [101] H. M. Choset "Principles of robot motion: theory, algorithms, and implementation." MIT press (2005).
- [102] F. Duchoň, A. Babinec, M. Kajan, P. Beňo, M. Florek, T. Fico and L. Jurišica. "Path planning with modified A star algorithm for a mobile robot." *Procedia Engineering*, 96, 59-69 (2014).
- [103] L. Ji and X. Sun. "A Route Planning's Method for Unmanned Aerial Vehicles Based on Improved A-Star Algorithm[J]." *Acta Armamentarii* 7 (2008): 788-792.